# Material-binding peptides empowering MP/NPs enrichment, detection, and quantification

Von der Fakultät für Mathematik und Naturwissenschaften der RWTH Aachen University zur Erlangung des akademischen Grades eines Doktors der Naturwissenschaften genehmigte Dissertation

vorgelegt von

**Maochao Mao**,

Master (M. Sc.) of Biotechnology

aus

Sichuan, China

Berichter: Univ.-Prof. Dr. rer. nat., Ulrich Schwaneberg

Univ.-Prof. Dr. rer. nat., Maria Fyta

Tag der mündlichen Prüfung: 20.04.2026

## Abstract

The widespread production and application of synthetic polymers has resulted in an annual global output of over 400 million metric tons. While their desirable properties support modern infrastructure and products, the transition toward a circular polymer economy is expected to dramatically increase the release of micro- and nanoplastics into the environment. These particles originate from various sources, including textiles, packaging, and tire abrasion, and have become pervasive across ecosystems, such as air, water, food, beverages, and even human tissues. The lack of standardized methods, particularly for particles smaller than 5 mm, remains a key regulatory and scientific barrier, as acknowledged by the European Commission. To address this, the primary objective of this doctoral thesis was to develop enrichment and analytical methods using material-binding peptides for the reliable detection and quantification of MP/NPs in environmental water samples and human tissues.

In the first part of the work, an enrichment platform called MagNanoTrap was developed. It is based on a custom-engineered bifunctional peptide (LCI-DZ-MBP1) that functionalizes $Fe_3O_4$ superparamagnetic nanoparticles. The LCI domain binds iron oxide beads, while MBP1 targets common plastic types such as polypropylene, polyethylene, polystyrene, and polyethylene terephthalate. This platform achieved an adsorption capacity of 3.95 ± 0.14 g/g for 500 nm polystyrene nanoparticles. In combination with pyrolysis–gas chromatography/mass spectrometry, the method enabled detection down to 0.061 μg of PS from only 1 L of water using 16 mg of coated SPIONs. The system proved effective across seven environmental water types, including river, lake, sea, and wastewater, for detecting a broad range of polymer types.

In the second part, a dual-functional biohybrid catalyst system was developed, named Hooked for Decay, for simultaneous micro- and nanoplastics capture and degradation. This system combines a Grubbs-Hoveyda catalyst with a peptide variant (LCI_F16C) immobilized on iron oxide beads. It forms a hydrophobic polynorbornene coating via ring-opening metathesis polymerization, allowing rapid capture of various hydrophobic nanoplastics such as polypropylene, polyethylene, polystyrene, poly(ethylene terephthalate), poly(methyl methacrylate), and styrene-butadiene rubber. The system demonstrated a high adsorption capacity (5.53 ± 0.29 g/g for polystyrene nanoplastics) and a 99% recovery rate for styrene-butadiene rubber nanoplastics. Moreover, the embedded catalyst retained its ethenolysis activity, achieving a 6.5% degradation of styrene-butadiene rubber, validating the potential of combined capture and degradation.

In the final part of this work, micro- and nanoplastics were successfully detected and quantified in 139 human kidney tissue samples using pyrolysis–gas chromatography/mass spectrometry. Eight different types of polymers were identified and quantified. Visualization of MP/NPs in kidney tissue was achieved using a fluorescently labeled peptide (“plastibody”). Importantly, an inverse correlation between MP/NP content and estimated glomerular filtration rate was observed, suggesting a possible link between particle accumulation and declining kidney function.

In summary, this thesis presents significant advances in the enrichment, detection, quantification, and biological assessment of micro- and nanoplastics. Two peptide-based nanotechnologies were developed: MagNanoTrap, which facilitates the efficient capture, identification, and quantification of nanoplastics in environmental water samples; and Hooked for Decay, which not only captures hydrophobic nanoplastics but also enables partial degradation of styrene-butadiene rubber nanoparticles. Furthermore, this work provides evidence of micro- and nanoplastic accumulation in kidneys and its potential association with impaired kidney function. Together, these findings contribute to the development of next-generation tools for environmental monitoring and public health assessment in the context of plastic pollution.

## Publications

### Sections of this thesis have been published in

**Mao, M.**,[+] Ahrens, L.,[+] Luka, J.,[+] Contreras, F., Kurkina, T., Bienstein, M., de Passos, M., Schirinzi, G., Mehn, D., Valsesia, A., Desmet, C., Serra, M., Gilliland, D., & Schwaneberg, U. (2024). Material-specific Binding Peptides Empower Sustainable Innovations in Plant Health, Biocatalysis, Medicine and Microplastic Quantification. *Chem. Soc. Rev.*, 53(12), 6445-6510.

**Mao, M.**, Bienstein, M., Contreras, F., Wang, D., Feng, L., & Schwaneberg, U. (2026). MagNanoTrap Enrichment Empowers Ultra-sensitive Quantification of Mixed Nanoplastic Particles from Environmental Water Samples. *Angew. Chem. Int. Ed.* 2026, e22823.

Wang, D.,[+] **Mao, M.**,[+] Lorberg, M., Luka, J., Bienstein, M., Okuda, J., & Schwaneberg, U. (2025). Hooked for Decay with Hydrophobic-coated Magnetic Beads to Grapple and Disintegrate Nanoplastics. *Angew. Chem. Int. Ed.* 2025, 64, e202510356.

[+] Shared first authorship

### Other projects

## Table of Contents

## List of Abbreviations

| | |
|---|---|
| µFTIR | Micro-FTIR |
| µRaman | Micro-Raman |
| BHIS | Brain heart infusion-supplemented |
| BSA | Bovine serum albumin |
| CBM | Carbohydrate-binding module |
| CD | Circular dichroism |
| cepPCR | Casting error-prone polymerase chain reaction |
| COF | Covalent-organic frameworks |
| DLS | Dynamic light scattering |
| DTG | Derivative thermogravimetric |
| DTT | Dithiothreitol |
| DZ | Domain Z |
| eGFR | Estimated glomerular filtration rate |
| eMBP | Engineered material-binding peptide |
| epPCR | Error-prone polymerase chain reaction |
| ESI-TOF MS | Electrospray ionization time-of-flight mass spectrometry |
| FACS | Fluorescence-activated cell sorting |
| FTIR | Fourier-transform infrared spectroscopy |
| GH | Grubbs–Hoveyda–type |
| ICP-MS | Inductively coupled plasma mass spectrometry |
| ICP-OES | Inductively coupled plasma optical emission spectrometry |
| LB | Lysogeny Broth |
| LCI | Liquid chromatography peak I |
| LOD | Limit of detection |
| LOQ | Limit of quantification |
| MBP | Material-binding peptide |
| MD | Molecular dynamics |
| MOF | Metal-organic frameworks |
| MP/NP | Micro-/nanoplastic |
| NaCl | Sodium chloride |
| nMBP | Naturally occurring material-binding peptide |
| NMR | Nuclear magnetic resonance |
| NTA | Nanoparticle Tracking Analysis |
| PAC | Poly-aluminum chloride |
| PAH | Polycyclic aromatic hydrocarbon |
| PC | Polycarbonate |
| PE | Polyethylene |
| PES | Polyethersulfone |
| PET | Polyethylene terephthalate |
| PMMA | Poly(methyl methacrylate) |
| PP | Polypropylene |
| PS | Polystyrene |

| | |
|---|---|
| PVC | Polyvinyl chloride |
| Py-GC/MS | Pyrolysis-gas chromatography/mass spectrometry |
| QM/MM | Quantum mechanics/molecular mechanics |
| ROMP | Ring-opening metathesis polymerization |
| SBR | Styrene-butadiene rubber |
| SEM | Scanning electron microscopy |
| SERS | Surface-Enhanced Raman Scattering |
| SPIONs | Superparamagnetic iron oxide nanoparticles |
| SQUID | Superconducting quantum interference device |
| SRS | Stimulated Raman Scattering |
| TED-GC/MS | Thermal Extraction Desorption-GC/MS |
| TEM | Transmission electron microscopy |
| TGA | Thermogravimetric analysis |
| VSM | Vibrating sample magnetometry |
| WWTP | Wastewater treatment plant |
| XPS | X-ray photoelectron spectroscopy |

## List of Figures

## List of Tables

# 1 Introduction

## 1.1 Challenge of MP/NPs for environmental and human health

Fully synthetic plastics first came into people's view as Bakelite in 1907.[1] From then on, the potential and possibilities of plastics for industrial applications were continuously explored. Until the 1950s, plastics began to be produced commercially on a large scale.[2] In 2023 alone, global polymer production, including widely used plastics such as polypropylene (PP), polystyrene (PS), polyethylene (PE), polyethylene terephthalate (PET), poly(methyl methacrylate) (PMMA), polycarbonate (PC), polyvinyl chloride (PVC) and nylons 6 and 66, reached 413.8 million metric tons (Plastics – the fast Facts 2024 • Plastics Europe). These materials are favored for their strength, flexibility, and resistance to corrosion, but their persistence in the environment and resistance to degradation present growing ecological and public health concerns.

Efforts to transition toward a circular polymer economy, emphasizing recycling, biodegradation, and reduced reliance on virgin plastic, are being actively promoted through new policies and infrastructure investments.[3-5] However, paradoxically, increased plastic recycling and the development of biodegradable plastics may inadvertently contribute to the rise in environmental micro- and nanoplastics (MP/NPs) load.[6] For example, it has been reported that up to 100 billion NPs can be released from just 1 gram of polyester textile,[7, 8] demonstrating the unintended consequences of current mitigation strategies.

MP/NPs, defined as plastic fragments smaller than 5 mm and 1000 nm, respectively, have become ubiquitous pollutants across global environments.[9] These particles are generated through various degradation processes, including mechanical abrasion, ultraviolet radiation, and microbial activity, which break down larger plastic debris into smaller particles.[10, 11] Additionally, MP/NPs are also directly released as primary particles through industrial manufacturing and consumer products, such as cosmetics, cleaning agents, or paints.[6] Due to their small size, MP/NPs have a high mobility, allowing them to travel easily through interconnected water networks.[12-14] They can also attach to fine airborne particulate matter (PM2.5), which enables their transport over long distances via atmospheric currents.[15] As a result, MP/NPs have been detected in a wide range of environments, including soil,[16] cloud,[17] surface waters,[18, 19] Antarctica,[20] and even deep-sea.[21] Studies have also reported MP/NPs in

food such as honey,[22] bottled water,[23] infant formula,[24] and beverages,[25] indicating a constant and unavoidable exposure to plastic particles in daily human life.

NPs, in particular, differ fundamentally from MPs in terms of behavior, transport, and toxicity. Their extremely high surface-to-volume ratio, combined with significant Brownian motion, gives them unique physicochemical properties.[9] These characteristics not only enhance their mobility but also increase their potential for cellular uptake, bioaccumulation, and adverse interactions with biological tissues.[26] Additionally, their hydrophobic surfaces can readily attract and concentrate more harmful substances such as PAHs, plasticizers, flame retardants, and pharmaceutical residues.[27] As a result, NPs are generally more bioavailable than MPs and pose a greater toxicological risk. Their small size allows them to penetrate biological membranes and,[28] alarmingly, even cross the blood-brain barrier, particularly for those smaller than 20 nm,[29] raising serious concerns about their potential to cause neurological and systemic health effects.

Recent research has confirmed the presence of MP/NPs in a variety of human tissues and organs, including kidneys,[30] lungs,[31] arteries,[32, 33] bones,[34] eyes,[35] brains,[30] and even the placenta.[36] Studies have linked MP/NP accumulation to multiple health risks, ranging from cardiovascular disease[33] to neurodegenerative disorders like Parkinson's disease[37] and amyotrophic lateral sclerosis.[38] Although quantification methods such as pyrolysis-gas chromatography/mass spectrometry (Py-GC/MS) have made it possible to detect these particles even in human blood, with concentrations averaging 1.6 μg/mL,[39] there remains a significant gap in our understanding of their long-term impacts, especially in relation to organ function and disease progression.

The ecological consequences are no less severe. In plants, MP/NPs have been shown to inhibit root elongation, reduce seed germination rates, and disturb nutrient uptake.[40-42] In aquatic organisms, ingestion of plastic particles has been documented in a variety of species,[43, 44] with mussels[45, 46] and zebrafish[47] now being explored as bioindicators of environmental plastic contamination. Moreover, tire-wear particles, predominantly composed of styrene-butadiene rubber (SBR), represent one of the largest sources of environmental MPs.[48] These elastomeric particles degrade into nano- and microscale fragments via road abrasion and weathering[49] and are released into the environment at an estimated 0.2 to 5.5 kg per person annually.[50]

The persistence of MP/NPs in ecosystems, combined with their potential to bioaccumulate, alter microbial communities, and interfere with physiological processes in plants, animals, and

humans, makes them one of the most pressing environmental and health challenges of our time.[6] Therefore, innovative and robust technologies are urgently needed to capture/enrich, detect, and degrade MP/NPs, not only to protect natural ecosystems but also to safeguard public health in an increasingly plastic-saturated world.

### 1.2 Analytics to detect and quantify MP/NPs

MP/NPs are persistent environmental contaminants that are increasingly detected in soil, water, air, and food. Their widespread presence has raised concerns about their potentially harmful, yet still poorly understood, impacts on ecosystems and human health.[51] While scientific attention to this issue began years ago, public interest has recently surged due to heightened media coverage, particularly regarding NPs. However, the understanding of their distribution, fate, and effects remains limited. Regulatory frameworks, such as those being considered by the EU Commission, are difficult to establish due to the lack of harmonized methods for larger MPs (<5 mm) and the analytical challenges in reliably identifying and quantifying submicron-sized NPs (<1 µm).[52, 53]

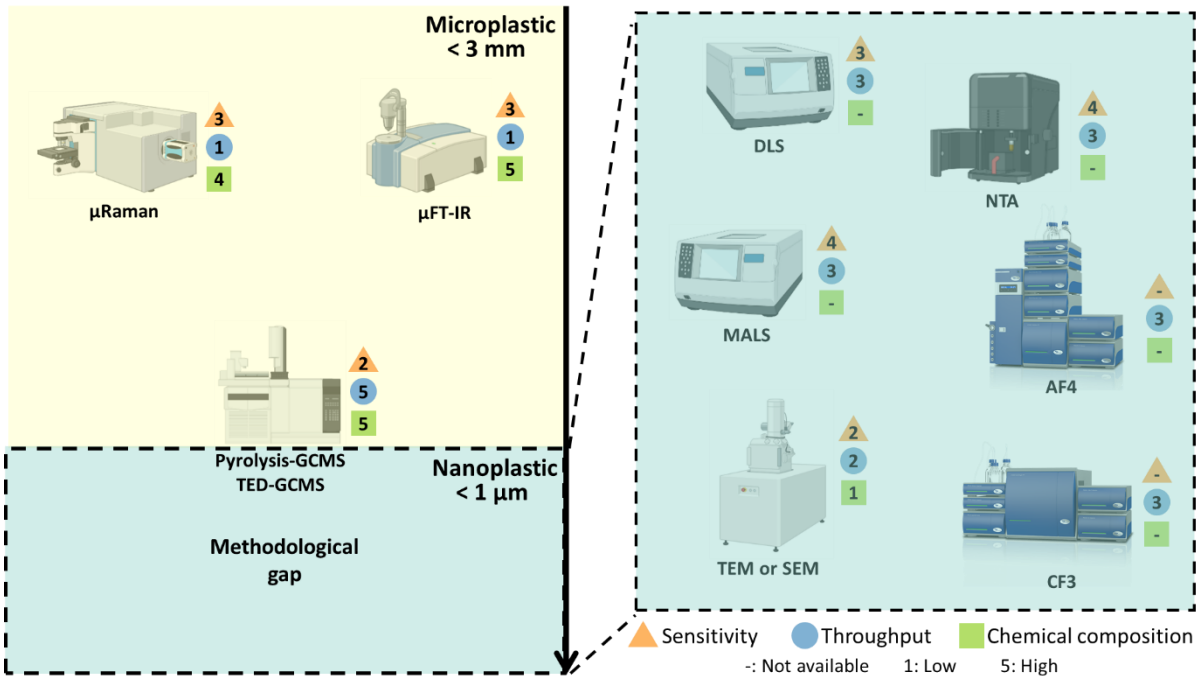


**Figure 1. Established and developing techniques relevant to the detection, quantification, and characterization of MP/NPs.** Taken from the Royal Society of Chemistry.[54]

Currently, only a limited number of analytical techniques are available for the detection and quantification of MP/NPs, each with its specific advantages and limitations. In general, polymer detection methods fall into three main categories: particle counting, optical micro-spectroscopy, and mass spectrometry (Figure 1).

In the first category, microscopy-based approaches, such as optical microscopy, fluorescence microscopy, scanning electron microscopy (SEM), and transmission electron microscopy (TEM), are used after sample enrichment, for example, via membrane filtration.[55] These techniques allow visualization and morphological analysis of particles ranging from the micro- to the nanoscale, but they offer low throughput and typically do not provide chemical identification. Another method used is light scattering-based analysis, particularly Nanoparticle Tracking Analysis (NTA), which enables size distribution and concentration measurement of NPs without prior enrichment.[56] However, NTA cannot distinguish between organic NPs and inorganic particles. Moreover, the presence of larger particles may interfere with the detection of smaller nanoparticles, compromising the accuracy of quantification. Fluorescence-based techniques are more sensitive and enable high-throughput quantification. In these methods, MNPs are stained with hydrophobic dyes such as Nile Red[57] or Plastibody reagents,[58] and counted using fluorescence-activated cell sorting (FACS). While Nile Red broadly labels hydrophobic materials, it lacks selectivity and may stain non-plastic particles. On the other hand, Plastibody, which consists of Alexa Fluor-labeled peptide probes, shows greater specificity. However, broader application of Plastibody technology requires development of a diverse set of polymer-specific binding peptides[59, 60] or a universal binding peptide that can reliably distinguish plastics from non-plastic particles.

The second category, vibrational spectroscopy, involves chemical identification through infrared (IR) and Raman microscopy.[61] These techniques are non-destructive, label-free, and provide spatially resolved information on polymer composition.[62, 63] Micro-FTIR (μFTIR) and micro-Raman (μRaman) are commonly used for this purpose. While IR spectroscopy detects changes in dipole moment, Raman spectroscopy is sensitive to changes in molecular polarization and is more effective for identifying polymers with symmetric structures and repeating units.[64, 65] Despite their advantages, both techniques are limited by the optical diffraction limit and detector sensitivity. μFTIR typically detects particles down to ~5–6 μm, whereas μRaman can reach sizes around 0.5–1 μm. Although Raman-based methods are now widely used for MPs detection, their limitations in throughput and size resolution have led to the development of advanced variants. For example, Stimulated Raman Scattering (SRS) Microscopy offers faster imaging and better resolution.[23] However, NPs enrichment via membrane filtration still poses challenges in recovery and size range. To overcome this, Moon *et al*. introduced a technique using pulsed laser-induced bubble formation to collect NPs, followed by transfer to glass substrates for Surface-Enhanced Raman Scattering (SERS)

analysis, allowing the direct visualization and identification of NPs in seawater.[66] In another approach, Shi *et al*. combined microfluidic manipulation with gold nanoparticle enrichment and SERS to identify and quantify NPs (e.g., PS, PMMA, PET) in environmental water samples as small as 7 mL.[67] While these advanced Raman methods show great potential, their cost and technical complexity may hinder broad implementation.

The third category consists of thermo-analytical techniques, such as Py-GC/MS and Thermal Extraction Desorption-GC/MS (TED-GC/MS).[68] These methods use high temperatures to thermally decompose polymers into volatile components, which are then separated via gas chromatography and identified by mass spectrometry. This approach allows for highly sensitive quantification, with detection limits ranging from 0.001 μg to 1 μg, depending on the polymer types.[33, 69] An advantage of thermo-analytical methods is that they are not constrained by particle size limits, provided the total polymer mass exceeds the detection threshold. However, these methods do not provide information on particle number, size, or morphology, and rely on prior enrichment to address sensitivity limitations. Despite these limitations, Py-GC/MS has been successfully applied to detect and quantify mixed MP/NPs in a variety of environmental and biological matrices. These include soil,[70] air,[71] freshwater,[18, 19] seawater,[72] wastewater,[69, 73] and biotic samples such as kidneys,[30] arteries,[32, 33] eyes,[35] and brains.[30] Moreover, these techniques have been used to detect MP/NPs in food and beverage products, such as seafood,[74] bottled water,[19] and soft drinks[75].

### 1.3 Remediation techniques of MP/NPs in water systems

To date, several physical and chemical remediation technologies have been developed to address the removal of MP/NPs from water systems. Among the physical approaches, sand filtration is a widely used and energy-efficient method commonly employed in wastewater treatment.[76] This technique relies on the mechanical trapping of plastic particles within the layers of sand as water passes through. Another widely studied method is membrane filtration, which removes MP/NPs based on the pore size of the membrane.[18, 19, 69, 73, 77, 78] Depending on the cutoff threshold, membrane filtration can be categorized into microfiltration, ultrafiltration, nanofiltration, and reverse osmosis, each capable of targeting different particle size ranges from micrometers down to nanometers. Sedimentation represents another important physical strategy, where plastic particles or their flocculated aggregates are allowed to settle at the bottom of a tank under the influence of gravity, effectively separating them from the water.[79] Flotation, in contrast, utilizes the introduction of air bubbles into water samples.[80, 81]

Hydrophobic MP/NPs tend to attach to these bubbles and rise to the surface, where they can be removed through skimming or other collection techniques.

In addition to physical methods, chemical approaches such as coagulation have proven effective. This method involves the addition of chemical coagulants, commonly ferric chloride ($Fe^{3+}$),[82] aluminum chloride ($AlCl_3$),[83] or poly-aluminum chloride (PAC),[84] which neutralize the surface charges of plastic particles, promoting their aggregation into larger flocs that can be removed through sedimentation or filtration.

Adsorption-based techniques form a particularly broad and promising category for MP/NP remediation. These methods utilize a range of physically or chemically functionalized materials, including carbons,[85] sponges/aerogels/fibers,[86-88] metal (hydr)oxides,[89] and zeolites/metal-organic frameworks (MOFs)/covalent-organic frameworks (COFs).[90-93] The underlying mechanism of adsorption relies on multiple types of interactions between the adsorbent and plastic particles. These include hydrophobic interactions, electrostatic attraction, π–π stacking, van der Waals forces, and hydrogen bonding.[94] The effectiveness of these interactions depends on the physicochemical properties of both the adsorbent surface and the MP/NPs.

Overall, while each method has its own advantages and limitations, a combination of physical and chemical strategies is often necessary to achieve efficient and reliable removal of MP/NPs from complex environmental water systems.

### 1.3.1 Magnetic materials-based techniques for MP/NPs enrichment

Superparamagnetic iron oxide nanoparticles (SPIONs), typically composed of $Fe_2O_3$ or $Fe_3O_4$, have recently gained significant attention as effective adsorbents for enriching organic compounds from aqueous environments. These nanoparticles offer a unique combination of a high surface-to-volume ratio and the ability to be easily separated from water using magnetic fields, making them both efficient and cost-effective for large-scale applications. Unmodified SPIONs have demonstrated the capability to remove contaminants such as glyphosate from water. More advanced designs, such as core-shell and double-shell SPION structures, have shown high efficacy in extracting crude oil, hydrocarbons, and other hazardous organic pollutants from water sources.[95-103]

Depending on their surface chemistry, iron oxide beads can interact with MP/NPs through various mechanisms. Bare iron oxide nanoparticles, which possess hydroxyl groups on their surfaces, can bind MP/NPs via hydrogen bonding.[104] When functionalized with long

hydrophobic alkyl chains, such as a C18 tail, iron oxide beads are capable of capturing MP/NPs through enhanced hydrophobic interactions.[72, 105, 106] Similarly, iron oxide beads coated with polyoxometalate-based ionic liquids also rely on hydrophobic interactions for plastic particle enrichment.[107]

Beyond traditional functionalized magnetic beads, researchers have also incorporated magnetic functionality into other materials during synthesis, giving rise to hybrid systems such as magnetic carbon,[108] magnetic MOFs,[92, 93] and even magnetically guided micro- and nanorobots.[109-111] These multifunctional materials further expand the toolkit available for the targeted capture and removal of MP/NPs from complex environmental systems.

### 1.3.2 Enrichment techniques applied to MP/NPs detection and quantification in environmental water samples

Due to the typically low concentrations of MP/NPs present in environmental water systems, an enrichment step is often essential prior to their detection and quantification. This enrichment facilitates accurate monitoring of their presence, distribution, and potential environmental and human health impacts. Most current analytical methods have been developed and validated using water samples spiked with known concentrations of MP/NPs. These spiked samples allow for the controlled testing of detection sensitivity and method reliability.

For instance, Jiménez-Lamana *et al.* employed positively charged gold nanoparticles to enrich negatively charged, carboxylated PS NPs, achieving a detection limit of 135 nm using inductively coupled plasma mass spectrometry (ICP-MS).[112] Besides, Zhou *et al.* used the surfactant Triton X-45 to extract PS and PMMA NPs, followed by analysis via Py-GC/MS, reporting recovery rates ranging from 84.6% to 96.6% for PS and 76.5% to 96.6% for PMMA.[113] Lai *et al.* advanced this method by combining Triton X-45 extraction (which avoids enrichment of inorganic particles) with gold nanoparticle enrichment, obtaining PS NP recoveries of 72.9% to 92.8% and enabling quantification by numbers in environmental water samples.[114]

For the detection of MP/NPs in environmental water samples, Yang *et al.* applied a silver nanowire membrane to trap PS NPs down to 50 nm with a recovery of 86.7%.[77] These were identified using SERS in environmental water samples such as water from expanded PS containers and seafood markets. Moon *et al*. developed a technique involving shrinking surface bubble deposition, where heated silver nanoparticles generated microbubbles that concentrated NPs.[66] With SEM and SERS, this method enabled the detection of nylon, PS, and PET NPs in

seawater. Xiao *et al*. took a different approach by combining simple paper filtration with flame ionization mass spectrometry to detect PET MP/NPs in commercial bottled water and juice products.[115]

For MP/NPs detection and also quantification in environmental water samples, Li *et al*. used alkylated iron oxide beads to bind and aggregate NPs.[72] After filtering the aggregates with glass fiber membranes, Py-GC/MS was used for quantification, yielding recovery rates of 71.9% to 119.0% for PS NPs, depending on water type. Detected PS NP concentrations ranged from 0.18 to 0.40 μg/L in seawater and from 0.24 to 0.73 μg/L in river water. Although PMMA was also targeted, it remained undetected in these samples. In a related method, Zhou *et al*. utilized bovine serum albumin (BSA) to coat the surface of NPs with a protein corona, followed by a salt-out and centrifugation process to concentrate the plastics.[116] Subsequent Py-GC/MS analysis yielded recoveries between 78.8% and 98.9% for PS NPs, with concentrations of 1.92 μg/L detected in river water and 2.82 μg/L in the influent of a wastewater treatment plant. PMMA was included in the analysis but was not detected. In another study, Shi *et al*. developed an advanced system using gold nanoparticle stacks combined with polylactic acid-based optical tweezers to capture and manipulate NPs.[67] This system, integrated into a microfluidic platform and coupled with SERS, achieved recoveries of 89.3% to 94.3% for PS NPs and a detection limit as low as 150 ng/L. Importantly, it required just 7.2 mL of sample to detect PS NP concentrations of 6.5–8.5 μg/L in river water, 1.4–1.8 μg/L in mariculture farm water, and 0.7–1.0 μg/L in beach water.

Despite these promising techniques, only membrane-based methods have been demonstrated to be broadly applicable for monitoring MP/NPs in diverse environmental water samples. These include both cross-flow systems, capable of processing up to 50 liters, and dead-end filtration setups working with 1-liter samples.[18, 19, 69, 73] Both approaches employed polyethersulfone (PES) membranes with a 0.01 μm pore size and were coupled with Py-GC/MS for analyzing a broad range of plastic types, such as PP, PE, PS, PET, PMMA, PC, nylon 6, and nylon 66. These membrane-based techniques achieved recoveries greater than 50%, demonstrating their suitability for comprehensive environmental monitoring.

### 1.4 Material-binding peptide

Material-binding peptides (MBPs) are short amino acid sequences with a distinctive ability to adhere to (specific) material surfaces. They are generally classified into two main types based

on their origin: (a) naturally occurring MBPs (nMBPs) and (b) engineered or synthetic MBPs (eMBPs), as illustrated in Figure 2.[54]

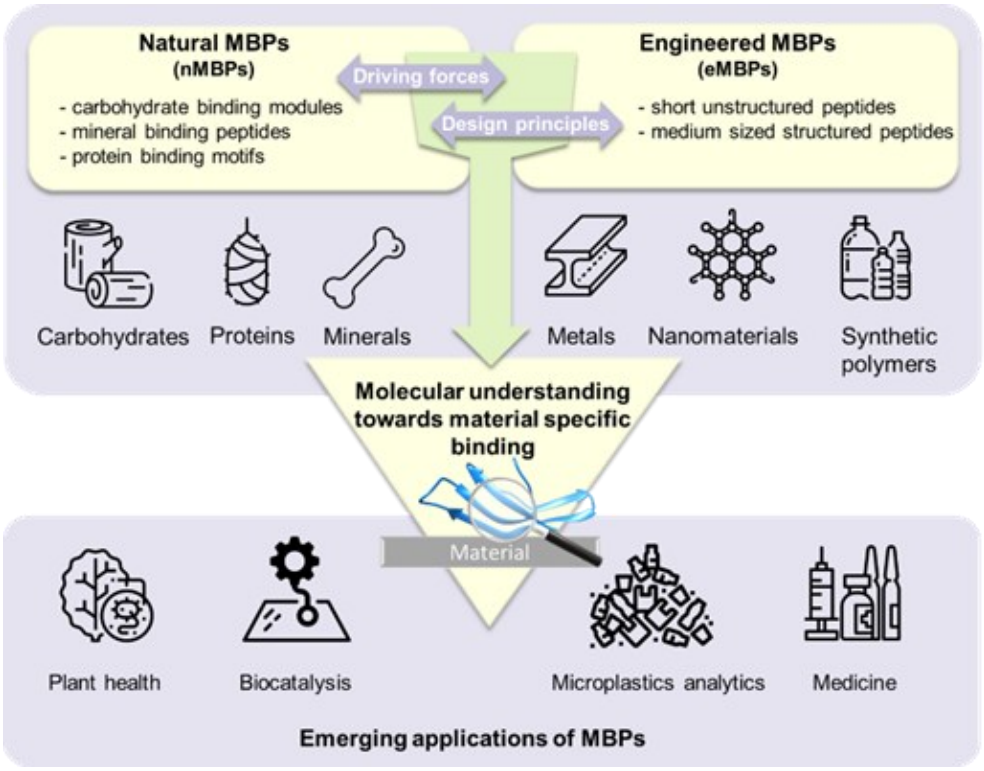


**Figure 2. Overview of material-binding peptides (MBPs) categorized into three main groups: natural MBPs (nMBPs), engineered MBPs (eMBPs), and those developed for emerging applications in fields such as plant health, biocatalysis, medicine, and microplastic analytics.** Taken from the Royal Society of Chemistry.[54]

Over millions of years, nature has evolved nMBPs to recognize and bind to specific classes of compounds, including carbohydrates (e.g., cellulose,[117, 118] chitin,[119, 120] and starch[121]), proteins (e.g., silk,[122] collagen,[123] and keratin[124]), and minerals (e.g., calcium carbonate,[125, 126] hydroxyapatite,[127] and silica[128]). These binding domains, such as carbohydrate-binding modules (CBMs), typically share a common β-sandwich fold structure composed of two overlapping β-sheets with 6–12 antiparallel β-strands and range from 30 to 200 amino acids in length.[129] CBMs bind to carbohydrates through three distinct modes. Type A CBMs interact with flat, crystalline surfaces such as cellulose and chitin using planar binding sites. Type B CBMs engage in groove-like internal binding modes, allowing them to accommodate longer sugar chains. Type C CBMs recognize short sugar residues at the ends of polysaccharides using pocket-like structures.[130] For protein- and mineral-binding peptides, binding motifs are often short (3–12 amino acids) and may exist as unstructured sequences unless embedded within larger proteins.[131] These natural MBPs play essential roles in biological processes such as biomineralization, host-pathogen interactions, cell adhesion, and the degradation of natural polymers.

Engineered MBPs are classified by their length and structural complexity. Class I eMBPs are short (≤20 amino acids), typically lack a defined secondary structure, and are often discovered through phage display or rational design. Class II eMBPs are longer (20–100 amino acids), structurally diverse, and tend to form stable 3D conformations upon material binding, similar to natural MBPs. These engineered peptides are tailored for binding to a variety of materials, including metals, polymers, metal oxides, and nanomaterials.[54]

The specificity and strength of MBP binding are driven by the spatial arrangement of amino acid side chains that engage in non-covalent interactions,[54] such as hydrogen bonding (e.g., Ser, Thr, Asn, and Glu), electrostatic interactions (e.g., Asp, Glu, Lys, Arg, and His), hydrophobic forces (e.g., Ala, Val, Leu, and Ile), and π–π stacking or aromatic interactions (e.g., Phe, Tyr, and Trp). Binding generally occurs through an initial contact interface involving a few amino acids, followed by broader interaction across a larger surface area involving multiple binding forces. Designing MBPs for specific material applications requires a comprehensive understanding of these molecular interactions and the influence of peptide structure and composition. Protein engineering allows the tuning of MBP properties to meet application-specific demands, such as altered binding strength, specificity, or environmental resilience.

MBPs offer a simple and energy-efficient method to functionalize surfaces under mild, aqueous conditions within minutes.[132] They exhibit strong adhesion to both natural (e.g., leaves,[133-135] graphite,[136] and metals[137, 138]) and synthetic materials (e.g., PP,[139] PS,[140] PET,[141] PLA,[59, 60] nylon 66,[142] and stainless steel[143, 144]). These peptides can form dense monolayers with surface coverage above 80%, creating ultrathin coatings (3–15 nm) that are effectively invisible.[142, 144] Their compatibility with scalable processes such as dip-coating and spray-coating, along with low production costs (covering up to 654 m² per gram at under €0.01/m²), makes them highly suitable for large-scale use.[143, 145]

One of the most extensively characterized peptides is the liquid chromatography peak I (LCI) peptide, which is composed of 47 amino acids and adopts a β-sheet structural motif.[146] Another notable material-binding peptide is MBP1, which features two parallel α-helices and contains a high proportion of arginine residues, approximately one-third of its 33 amino acids.[147] The presence of positively charged amino acids, particularly arginine and lysine, has been shown to significantly enhance binding affinity to various polymer surfaces, including PP,[148] PET,[142] and polyamide.[142] Due to this property, MBP-1 serves as a promising candidate for use as a universal binder for a wide range of plastic surfaces in the context of this thesis.

Despite their promising properties and versatility, MBPs are not yet widely adopted in industrial settings outside of diagnostic applications, where chemical immobilization techniques still dominate. However, their potential in sustainable bioeconomy frameworks continues to grow, with emerging solutions targeting diverse challenges across multiple fields, such as plant health, biocatalysis, medicine, and microplastic analysis.

### 1.4.1 Bifunctional protein/peptide

MBPs can be genetically fused to biomolecules, such as enzymes or antimicrobial peptides, or chemically linked to functional molecules via click chemistry, such as metal catalysts or anti-fouling agents (Figure 3). These combinations result in either MBP-protein fusions or biohybrid systems that can be stably and directionally immobilized onto material surfaces. To ensure optimal function, both the binding and active domains are separated by spacer sequences. These spacers may be rigid linkers like Domain Z (DZ, consisting of three parallel α-helices) and 17x α-helices, flexible sequences such as GGGS, or chemical linkers of varying carbon chain lengths. The spatial separation between functional units is critical to prevent interference between domains, thereby preserving their individual binding, catalytic, or functional properties.[54]

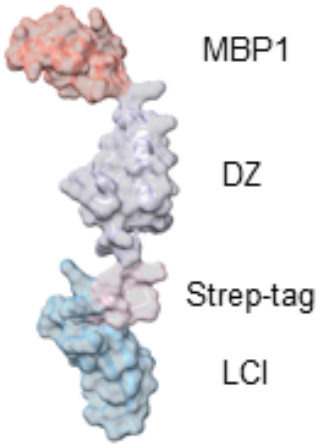


**Figure 3. Exemplary construct of a bifunctional peptide.** Material-binding peptide LCI is fused to another material-binding peptide MBP1, with DZ as a linker.

Most MBP applications rely on bifunctional constructs. In biocatalysis, these bifunctional peptides support the efficient anchoring of enzymes[60, 143, 149, 150] and metal catalysts[151, 152] onto diverse surfaces, including polymers and stainless steel, offering possibilities for polymer recycling and the development of membrane reactor systems. In the medical field, MBPs are used to create biocompatible interfaces for devices like implants and prosthetics, supporting cell growth and recruitment, while also incorporating properties such as antimicrobial

activity[153-155] and anti-fouling.[156, 157] In agriculture, the use of MBPs is rapidly expanding, particularly for reducing pesticide usage and nutrient delivery.[133-135, 145] MBPs also offer improved rain resistance compared to conventional pesticide formulations.[135] Besides, the use of MBPs minimizes environmental accumulation since they are entirely bio-based and biodegradable.

### 1.4.2 Protein engineering of material-binding peptide (eMBPs)

Protein engineering is a powerful tool that enables the functional optimization of proteins, including enhancing binding strength or material specificity in eMBPs. eMBPs are typically categorized into two classes: class I peptides (<20 amino acids) and class II peptides (20–100 amino acids). Notably, class II eMBPs often adopt a defined three-dimensional structure, in contrast to the typically unstructured class I peptides. Depending on the eMBP class, different engineering strategies can be employed to tailor their properties (Figure 4).

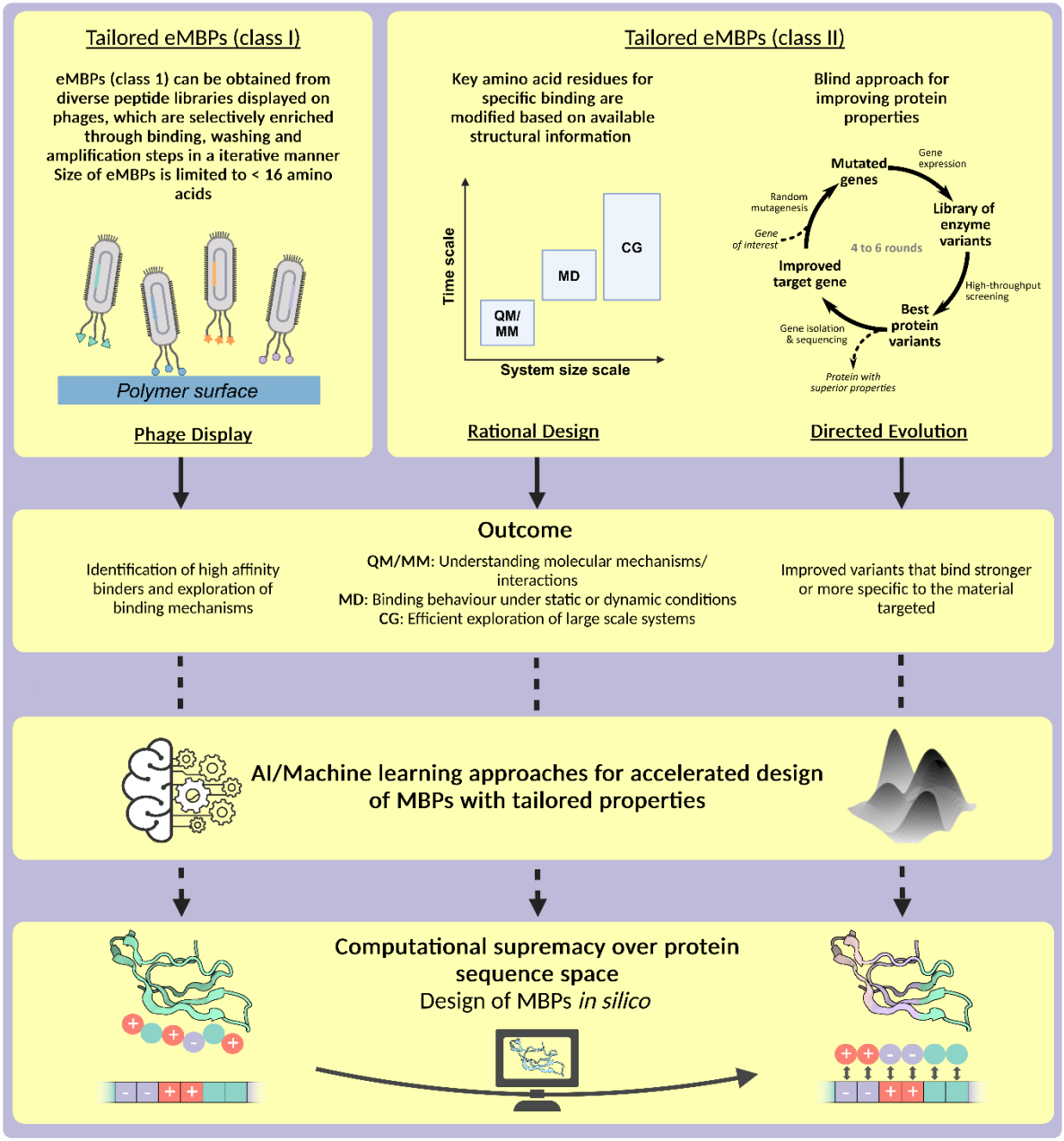


**Figure 4. Overview of protein engineering methodologies towards material-binding peptides.** It comprises phage display (class I), rational design, and directed evolution (class II), all of which have been utilized in engineering eMBPs. These approaches have yielded important outcomes and contributed experimental data and biophysical insights necessary for effectively navigating the vast protein sequence space. Taken from the Royal Society of Chemistry.[54]

Phage display remains the primary technique for identifying short peptides, especially for diagnostic applications, and is the preferred method for engineering class I eMBPs. Phage display of peptides and antibodies, which earned the 2018 Nobel Prize in Chemistry, marked a significant breakthrough by enabling the directed evolution of short binding proteins. This technique relies on the expression and selection of peptides on the surface of phages, creating a physical link between phenotype and genotype.[158] However, a key limitation of phage display

is that the length of the peptides is typically restricted to fewer than 16 amino acids. The phage display workflow involves creating large peptide libraries, cloning them into the phage genome, and selecting high-affinity binders through iterative rounds of biopanning. These libraries can reach a diversity of up to $10^{11}$ unique sequences, which are typically fused to phage coat proteins to enable their surface display.[159, 160] Thanks to this vast diversity, peptide or antibody variants with low nanomolar dissociation constants can be identified.[161] Following library construction, the next phase is the iterative biopanning process. In this step, the phage library is incubated with the target material, after which multiple washing steps are performed to remove non-specific or weakly bound clones. The phages that remain bound are then eluted and amplified in *Escherichia coli*, serving as the template for the next round of selection. After several rounds, high-affinity candidates are isolated, sequenced, and further characterized to understand their binding mechanisms.[162] In addition, protein engineering approaches such as rational design, directed evolution, or hybrid strategies can be employed to fine-tune the properties of class II eMBPs.

Rational design strategies can be broadly categorized into sequence-based analyses and structure-based modeling approaches.[163] The former are computationally less intensive and involve the alignment or analysis of protein sequences to identify structurally or functionally related proteins. One widely used method in this category is consensus design, which involves generating stable protein variants by combining the most frequently occurring amino acids at each position from a group of evolutionarily related proteins. In contrast, structure-based computational design requires greater computational resources and evaluates protein functionality based on three-dimensional structural features. This approach can identify functional structural motifs even among unrelated proteins, offering insights into protein activity and binding behavior. Quantum mechanics/molecular mechanics (QM/MM) methods are often employed to model protein–protein interactions or reaction mechanisms, particularly when high-resolution modeling at the smallest time and spatial scales is required.[164] However, to date, these methods have not been applied to the engineering of material-binding peptides. Other computational tools, such as substrate docking and molecular dynamics (MD) simulations, allow for in-depth analysis of specific residues and their interactions, helping to elucidate how peptides interact with their binding partners or other molecular targets. For large-scale systems and longer timescales, coarse-grained modeling is useful for examining broader behaviors and system dynamics. Overall, rational design of material-binding peptides and

proteins facilitates a deeper understanding of the biophysical properties that govern their binding mechanisms.

Directed evolution has become a standard tool in industrial protein engineering, enabling the adaptation of natural proteins for a wide range of biotechnological applications. These include the sustainable enzymatic production of chemicals and pharmaceuticals, as well as the development of custom enzymes for industries such as food, feed, and laundry—an achievement recognized by the 2018 Nobel Prize in Chemistry.[158, 165] This approach involves iterative cycles of diversity generation, typically through methods like error-prone polymerase chain reaction (epPCR), followed by screening of the resulting protein variants to identify improved candidates under specific selection pressures (e.g., enhanced activity, solvent resistance, or thermal stability). One of the main challenges in directed evolution is the efficient exploration of the vast protein sequence space. For example, a 50-residue peptide has a theoretical diversity of $20^{50}$ possible sequences (approximately $1.63 \times 10^{65}$), making experimental screening highly resource-intensive. To address this, smart strategies such as KnowVolution have been developed.[166] KnowVolution integrates computational predictions with experimental data to optimize mutational efforts and achieve targeted improvements with minimal workload. For eMBPs ranging from 30 to 120 amino acids, traditional mutation rates (3–5 mutations per 1000 bp) are insufficient. Instead, higher mutation frequencies (20–50 mutations per 1000 bp) are required. This technical hurdle has been overcome through the development of specialized mutagenesis protocols, namely casting error-prone polymerase chain reaction (cepPCR)[167] and PepEvo1[168], by Prof. Schwaneberg's group. Ultimately, directed evolution yields improved variants of class II eMBPs, which exhibit stronger and more specific binding to target materials, contributing to a deeper understanding of the underlying molecular interactions.

Moreover, the insights gained from engineering both classes (class I and II) of eMBPs can be leveraged using machine learning and artificial intelligence to accelerate and optimize peptide design.[169] The final goal within the field of engineering material-binding peptides is the computational supremacy over protein sequence space, which would enable the design of MBPs *in silico*.

### 1.5 Objective

MP/NPs are ubiquitous contaminants in the environment, particularly in aquatic ecosystems. One of the main challenges in MP/NPs detection and quantification lies in the current analytical

gap in reliably quantifying particles smaller than 5 mm, which has been acknowledged by the EU Commission as a major limitation to establish effective regulations on MP/NP contamination.[52, 53] Additionally, recent research has raised growing concern about the potential impact of MP/NPs on human health, highlighting the urgent need for investigation of their biological effects.

The main objective of this thesis is to develop effective enrichment strategies using MBPs, validated through case studies with deionized water, wastewater, and environmental water, to address the challenge of quantifying low MP/NP concentrations. In addition, it aims to establish a robust detection and quantification protocol based on Py-GC/MS, enabling reliable analysis in environmental samples and extending its application to biological samples to explore potential human health impacts. Specifically, in Section 3.1, the secondary objective was to develop a custom-engineered bifunctional peptide, LCI-DZ-MBP1, to functionalize iron oxide nanoparticles for capturing NPs. This enrichment platform, termed MagNanoTrap, was validated across seven different 1 L environmental water samples, followed by Py-GC/MS analysis for plastic identification and quantification. Section 3.2 had the secondary objective of introducing a tailored system, Hooked for Decay, featuring a biohybrid catalyst (**GH**@LCI_F16C) immobilized on iron oxide nanoparticles. This system formed a hydrophobic polymer coating via ring-opening metathesis polymerization for efficient MP/NP capture and included an embedded Grubbs-Hoveyda catalyst for subsequent degradation of SBR NPs. In Section 3.3, the secondary objective was to assess the correlation between MNP accumulation and decreased kidney function. Here, we analyzed 139 human kidney tissue samples, stratified by estimated glomerular filtration rate (eGFR), using Py-GC/MS to quantify MP/NP content and assess correlations with kidney function. Additionally, to visualize the spatial distribution of MP/NPs within kidney tissues, we applied a fluorescently labeled material-binding peptide ("plastibody") for imaging under confocal microscopy. In summary, this thesis introduces innovative peptide-enabled nanotechnologies that contribute significantly to the advancement of water remediation strategies. These systems also enhance analytical capabilities for the detection and quantification of MP/NPs in complex environmental samples. Moreover, the work offers critical insights into the biological accumulation of MP/NPs in human tissues, providing a foundation for future studies on their potential health impacts. Altogether, these contributions pave the way for the development of next-generation tools for both environmental and biomedical monitoring.

# 2 Materials and methods

## 2.1 Chemicals

Unless otherwise specified, all chemicals were obtained from commercial suppliers, including Sigma-Aldrich/Merck, TCI, BLDpharm, and others. Aqueous dispersions of $Fe_3O_4$ nanoparticles were purchased from Particular Materials SRL (Italy) and PlasmaChem GmbH (Germany). PMMA and PS nanoparticles with various charges and sizes were acquired from microParticles GmbH (Germany) and Polysciences Europe GmbH (Germany), respectively. The Microplastics Calibration Standard-Low Set was obtained from Frontier Lab (Japan). Al Grubbs–Hoveyda–type (**GH**) cofactors, including **GH-C3**, **GH-C5**, and **GH-C10**, monomer **Nor-C18**, and **Nor-SH** were synthesized following the procedure described in the corresponding manuscript in this thesis.

## 2.2 Protein expression and purification

### 2.2.1 Expression and purification of LCI-DZ, DZ-MBP1, and LCI-DZ-MBP1

DNA sequences encoding protein LCI-strep-DZ, strep-DZ-MBP1, and LCI-strep-DZ-MBP1 (see Appendix) were synthesized by GenScript Biotech (Netherlands) and cloned into the pET-28a(+) expression vector. The synthesized plasmids were transformed into *E. coli* BL21(DE3) competent cells for intracellular protein expression.

Following overnight incubation at 37 °C with shaking, the pre-culture was used to inoculate 50 mL of Lysogeny Broth (LB) medium containing 50 µg/mL kanamycin. Cultures were grown at 37 °C and 200 rpm until the optical density at 600 nm ($OD_{600}$) reached 0.4–0.6. Protein expression was then induced by adding 0.1 mM IPTG, followed by incubation at 18 °C and 200 rpm overnight.

Cells were harvested by centrifugation at 4000 rpm for 20 min and resuspended in buffer A (50 mM Tris-HCl, pH 8.0, and 300 mM NaCl), then lysed via sonication (15s/15s, 5 min). The lysate was centrifuged at 12000 rpm for 10 min, and the resulting supernatant was loaded onto a Strep-Tactin®XT 4Flow® gravity column pre-equilibrated with buffer A after filtration with a 0.45 µm filter. After washing with 10 column volumes of buffer A, target proteins with strep tag were eluted using buffer B (50 mM Tris-HCl, pH 8.0, 300 mM NaCl, and 2.5 mM desthiobiotin). The eluted proteins were subsequently buffer-exchanged into buffer C (50 mM Bicine-NaOH, pH 9.0) using a PD-10 Desalting Column (Cytiva). All purification steps and buffer exchange procedures were performed at 4 °C. Protein concentrations were determined

by UV absorbance at 280 nm. The purified proteins were flash frozen in liquid nitrogen and stored at -80 °C for later use.

### 2.2.2 Expression and purification of LCI_F16C

DNA sequence encoding protein LCI_F16C (see Appendix) was synthesized by GenScript Biotech (Netherlands) and cloned into the pEKEx2 expression vector. The synthesized plasmids were transformed into *Corynebacterium glutamicum* ATCC 13032 competent cells for extracellular protein expression.

Pre-cultures were grown overnight at 30 °C in 5 mL of Brain Heart Infusion-Supplemented (BHIS) medium, consisting of 37 g/L brain heart infusion powder, 91 g/L sorbitol, and 50 µg/mL kanamycin, using 15 mL Falcon tubes. The main cultures containing 200 mL of BHIS medium supplemented with 25 µg/mL kanamycin were inoculated with the pre-cultures and grown at 30 °C until the $OD_{600}$ reached 0.6-1.0. Protein expression was then induced by the addition of 0.1 mM IPTG, followed by incubation at 18 °C and 200 rpm for 48 h.

Cells were removed by centrifugation at 5000 rpm for 30 min, and the supernatant containing the target proteins was loaded onto a Strep-Tactin®XT 4Flow® gravity column pre-equilibrated with buffer A. After washing with 10 column volumes of buffer A, target proteins with strep tag were eluted using buffer B (50 mM Tris-HCl, pH 8.0, 300 mM NaCl, and 2.5 mM desthiobiotin). The eluted proteins were subsequently buffer-exchanged into buffer D (50 mM Tris-HCl, pH 8.0) using a PD-10 Desalting Column (Cytiva). All purification steps and buffer exchange procedures were performed at 4 °C. Protein concentrations were determined by UV absorbance at 280 nm. The purified proteins were flash frozen in liquid nitrogen and stored at -80 °C for later use.

## 2.3 Conjugation of metal cofactor

Grubbs-Hoveyda type cofactors (**GH-C3**, **GH-C5**, and **GH-C10**) were covalently conjugated to LCI_F16C via a maleimide linker targeting the reduced thiol group of the cysteine residue in the peptide. Specifically, to reduce the disulfide bond, LCI_F16C (200 µM) was incubated with 15 mM DTT for 60 minutes at room temperature. After reduction, DTT was removed by buffer exchange via a PD-10 Desalting Column (Cytiva). The conjugation reaction was carried out by incubating the reduced LCI_F16C with 5.0 equiv. of GH-cofactor (final concentrations: 20 µM protein, 100 µM cofactor) in Tris-HCl buffer (20 mM, pH 7.5, 150 mM NaCl) containing 5% DMSO (v/v) for 60 minutes at room temperature. Following conjugation, the reaction buffer was exchanged to the binding buffer (50 mM Tris-HCl, pH 8.0). The resulting

biohybrid catalysts, such as **GH-C3**@LCI_F16C, **GH-C5**@LCI_F16C, and **GH-C10**@LCI_F16C, were flash frozen in liquid nitrogen and stored at -80 °C for later use.

### 2.4 Conjugation of Alexa Fluor 594 fluorescent dye

Conjugation of Alexa dye 594 compounds to LCI_F16C was carried out through covalent bonding between the maleimide group of the dye and the reduced thiol group of the cysteine residue in LCI_F16C peptide. The thiol group was reduced by incubating 50 µM LCI_F16C with 5 mM DTT for 2 hours at room temperature. Following reduction, DTT was removed via buffer exchange with a PD-10 Desalting Column (Cytiva). The reduced protein was subsequently incubated with 5.0 equiv. of Alexa-maleimide 594 dyes in Tris-HCl buffer (50 mM, pH 8) for 60 minutes at room temperature. After the conjugation, the biohybrid Alexa 594@LCI_F16C was stored at 4 °C in binding buffer (50 mM Tris-HCl, pH 8.0).

### 2.5 Protein modeling

Structure of the bifunctional peptide LCI-DZ-MBP1 was predicted by AlphaFold2[170] and visualized by ChimeraX 1.4.[171]

Structure modelling of the biohybrid catalysts with different linker lengths was based on the NMR solution structure of wild-type LCI (PDB: 2B9K).[146] The F16C mutation, which introduces a cysteine residue for anchoring, was introduced *in silico*. The resulting LCI_F16C structure underwent energy minimization using YASARA Structure (version 20.12.24) with the AMBER14 force field.[172] Following established protocols,[173, 174] the modeling was performed using YASARA Structure (version 20.12.24), applying the AMBER14 force field for protein residues and GAFF[175] with AM1/BCC[176] partial charges for the covalently bound catalyst. To preserve correct coordination geometry, distances and angles between the metal center and coordinating atoms were constrained based on a previously reported crystal structure.[177] Additional atoms required for the linker were manually added. The metal center was assigned a +2 charge, and the overall charge of the catalyst was set to neutral. The linker was manually positioned near Cys16, and a covalent bond was defined between the sulfur atom of the cysteine and the C1 atom of the maleimide group. The resulting biohybrid catalyst models were solvated in a TIP3P water box under periodic boundary conditions at pH 7 and a density of 0.997 g/mL. Three initial conformations were evaluated, and favorable models for covalent attachment to the reactive maleimide were identified using steepest descent minimization and simulated annealing. These pre-minimized structures were further refined

through molecular dynamics simulations at 298 K for 5000 ps, with snapshots taken every 25 ps to analyze binding modes.

### 2.6 Preparation of PP, PE, PET, and SBR NPs

PP, PE, and SBR nanoparticles were synthesized based on the method reported by Faeze *et al.*,[178] with modifications. In brief, 10 mg of PP granules, LD-PE powder, or SBR granules were dissolved in 5 mL of xylene at 110 °C on a heating plate for 10 minutes until fully dissolved. While stirring vigorously, 20 mL of ice-cold deionized water was rapidly added to emulsify the solution, followed immediately by water bath sonication for 30 minutes. After emulsification, larger particles were removed using Whatman Grade 1 qualitative filter paper. The filtration step was repeated once more following gentle magnetic stirring for 2 hours at room temperature, yielding a stable dispersion of nanoparticles in water.

PET nanoparticles were prepared following a previously reported protocol.[179] In summary, 10 mg of PET powder was dissolved in 2 mL of 1,1,1,3,3,3-hexafluoro-2-propanol at room temperature for 1 hour. The resulting PET solution was then added dropwise into 20 mL of deionized water under vigorous magnetic stirring. To remove the organic solvent, the suspension was gently stirred at room temperature for an additional 2 hours. The precipitated nanoparticles were subsequently collected by filtration using filter paper.

### 2.7 Preparation of functionalized iron oxide beads

#### 2.7.1 LCI-DZ-MBP1 coated iron oxide beads

The functionalization of the beads was carried out by incubating $Fe_3O_4$ nanoparticles (0.3 g/L) from Particular Materials with an excess of the bifunctional peptide LCI-DZ-MBP1 (5 µM) in Bicine/NaOH buffer (50 mM, pH 9) in a total volume of 200 µL. The mixture was shaken at 1200 rpm for 1 minute in screw-neck glass vials (ND 8, TH. GEYER GmbH & Co. KG, Germany). Following the reaction, magnetic separation was used to wash the beads with water, and the functionalized nanoparticles were subsequently resuspended in water for further applications.

#### 2.7.2 Film-coated iron oxide beads

The immobilization of the biohybrid catalyst was performed by incubating $Fe_3O_4$ nanoparticles (75 µg/mL) from PlasmaChem with an excess of catalyst **GH**@LCI_F16C (5 µM) in Tris-HCl buffer (50 mM, pH 8) in a total volume of 200 µL. The mixture was shaken for 1 minute, followed by two washing steps with water to remove unbound catalyst under a magnetic field.

The peptide-functionalized $Fe_3O_4$ nanoparticles were then resuspended in water, and the modified monomer (20–500 µM, prepared as a 10 mM stock in methanol) was added. The reaction mixture was shaken for 1 to 9 minutes to allow formation of a hydrophobic film. Subsequently, the film-coated $Fe_3O_4$ nanoparticles were washed twice with water to remove excess monomer and resuspended in water for further use.

### 2.7.3 Fluorescence-labeled film-coated iron oxide beads

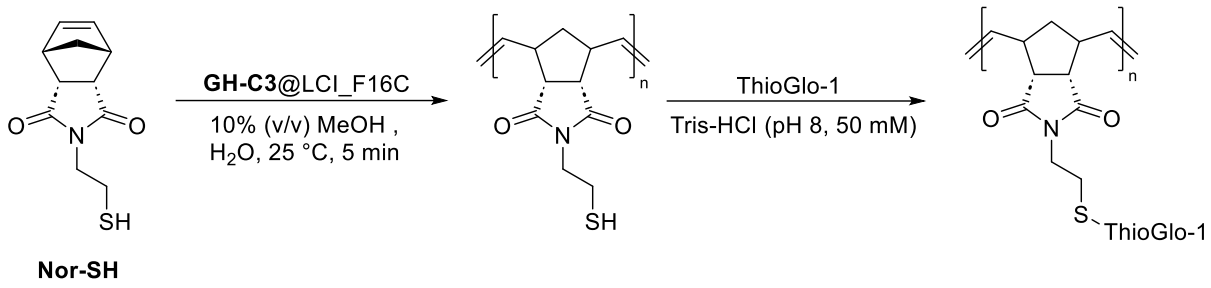


**Figure 5. ROMP of Nor-SH with the following labeling by ThioGlo-1.**

The polymer film was formed using **Nor-SH** as the monomer, following the procedure described above. Upon completion of the polymerization, ThioGlo-1 was added to label the free thiol groups presented on each monomer, enabling subsequent fluorescence characterization (Figure 5).

### 2.8 Characterization

A range of analytical techniques was employed to characterize the materials and assess experimental outcomes. A fluorescence microscope (BX51, Olympus) was used to visualize peptide binding on material surfaces and confirm polymer film formation. FACS (MoFlo Astrios EQ, Beckman Coulter) was applied to evaluate the functionalization efficiency of MagNanoTrap beads. Dynamic light scattering (DLS) and zeta potential measurements were performed using a Zetasizer (Malvern Panalytical) to determine the nanoparticle size distribution and surface charge, respectively. Thermogravimetric analysis (TGA, STA6000, PerkinElmer) was used to monitor sample mass loss during heating from 100 °C to 800 °C. Surface chemical composition was analyzed using X-ray photoelectron spectroscopy (XPS, AXIS Supra+, Kratos Analytical) and Fourier-transform infrared spectroscopy (FTIR, Nicolet iS20, Thermo Scientific). Electrospray ionization time-of-flight mass spectrometry (ESI-TOF MS, Agilent) confirmed successful functionalization of magnetic beads with bifunctional peptides. Magnetic properties before and after functionalization were examined using a superconducting quantum interference device (SQUID) magnetometer (MPMS-XL, Quantum

Design). Sample morphology was investigated via SEM (SU9000, Hitachi), while internal structural features were visualized using TEM (SU9000, Hitachi). Nuclear magnetic resonance (NMR) spectroscopy was conducted on Bruker Avance II or Avance III spectrometers at 400 MHz for $^{1}H$ and 101 MHz for $^{13}C$ nuclei to characterize the formation of the polymer film. Chemical shifts were referenced to residual proton signals of the deuterated solvents and reported relative to tetramethylsilane. Standard multiplicity abbreviations were used: s (singlet), d (doublet), t (triplet), q (quartet), quint (quintet), and m (multiplet). Circular dichroism (CD) spectra were recorded on a JASCO J-1100 spectrometer with a Peltier-controlled cell holder to analyze secondary structure changes of the biohybrid **GH**@LCI_F16C. Unless otherwise specified, measurements were conducted at 19 °C with a 0.2 mm path length cuvette and a protein concentration of 20 µM. Inductively coupled plasma optical emission spectrometry (ICP-OES) was performed using a Spectroblue ICP-OES instrument (Spectro Analytical Instruments) to confirm the conjugation of GH-cofactors to peptide LCI_F16C. Calibration was carried out using a commercially available ruthenium standard (1.0 g/L, Sigma-Aldrich), with calibration samples prepared at concentrations of 0 ppm, 2 ppm, and 5 ppm Ru.

### 2.9 200 µL-scale enrichment

Enrichment experiments were performed on a 200 µL scale using glass vials and evaluated by UV absorbance measurements (CLARIOstar, BMG Labtech). In each experiment, the functionalized iron oxide beads were mixed with 0.2 g/L of PS nanoparticles and 100–200 mM NaCl in aqueous solution, with a final volume of 200 µL. The mixture was shaken at 1200 rpm for 20 minutes, followed by magnetic separation. Subsequently, 100 µL of the supernatant was transferred to a transparent 96-well plate for UV-vis absorbance analysis.

Nanoparticle concentration in the supernatant was determined using a calibration curve generated from standard UV-vis measurements. The nanoparticle recovery rate ($R_1$) was calculated using Equation (1):

$$R_1 = \left(1 - \frac{C_t}{C_0}\right) * 100\% \quad (1)$$

where $C_t$ is the concentration of PS NPs in the supernatant after magnetic separation, and $C_0$ is the initial PS NPs concentration.

The adsorption uptake $q$ (g/g) was calculated using Equation (2):

$$q = \frac{C_0 - C_t}{C_m} \quad (2)$$

where $C_m$ represents the concentration of functionalized iron oxide beads. All experiments were performed in triplicate to ensure reproducibility.

### 2.10 Adsorption kinetics models

The adsorption kinetics in this study were evaluated using two commonly applied models: the Pseudo-first-order model (3) and the Pseudo-second-order model (4).[180]

$$q_t = q_e(1 - e^{-k_1 t}) \quad (3)$$

$$q_t = \frac{k_2 q_e^2 t}{1 + k_2 q_e t} \quad (4)$$

In these equations, $q_t$ represents the amounts of NPs adsorbed per unit mass of functionalized iron oxide beads at a given time t, while $q_e$ denotes the adsorption capacity at equilibrium. The constants $k_1$ and $k_2$ are the adsorption rate constants for the Pseudo-first-order and Pseudo-second-order models, respectively.

### 2.11 Adsorption isotherm models

The adsorption isotherms in this study were evaluated using two widely accepted models: the Freundlich model (5) and the Langmuir model (6).[181]

$$q_e = K_F C_e^{1/n} \quad (5)$$

$$q_e = \frac{q_m K_L C_e}{1 + K_L C_e} \quad (6)$$

In these equations, $C_e$ (g/L) represents the equilibrium concentration of the adsorbate (PS NPs), while $q_e$ and $q_m$ denote the adsorption capacities at equilibrium and at maximum adsorption, respectively. $K_F$ and $K_L$ (L/g) are the isotherm constants for the Freundlich and Langmuir models, respectively.

### 2.12 Environmental water samples collection

Water samples were collected from various natural and anthropogenic sources. Lake water from a natural reservoir was sampled at Eifel National Park (Monschau, Germany), while lake water influenced by human activities was obtained from Hangeweiher (Aachen, Germany). River water samples were taken from the Rhine River (Düsseldorf, Germany). Seawater, collected at a depth of 50 meters off the coast of Portugal, was purchased from Mrutzek Meeres-Aquaristik GmbH (Germany). Wastewater samples were sourced from the effluent of the SIDEN wastewater treatment plant in Heiderscheidergrund (Luxembourg). Additional treated wastewater samples, obtained after sand filtration and crossflow ultrafiltration (Boll &

Kirch system), were provided by APATEQ (Luxembourg). All samples were stored in glass bottles with PP caps at 4 °C, except for the seawater, which was stored in a PE container.

### 2.13 1 L-scale enrichment

Deionized water spiked with NPs was used for method optimization, while environmental water samples required a pretreatment step before extraction. Specifically, each 1 L water sample was vacuum filtered through 1 µm glass fiber filters (47 mm) using a stainless-steel filtration unit to remove microorganisms, algae, suspended solids, organic debris, and MPs. The resulting filtrate was collected in a 5 L glass flask and subjected to oxidative digestion by adding 100 mL of 30% $H_2O_2$ and incubating at 60 °C for 48 hours in an orbital incubator shaker (Minitron, INFORS, Switzerland) to eliminate organic matter on the NPs surface.[19, 69]

One liter of either the digested samples cooled to room temperature or the NPs-spiked deionized water was mixed with 16 mg of MagNanoTrap beads and 1 M NaCl, and shaken at 200 rpm for 2 hours to promote adsorption. Afterward, it was transferred to a 500 mL glass beaker, where magnetic extraction was used to isolate the MagNanoTrap-NPs complex. These complexes were then resuspended in 5 mL of deionized water and transferred to a 1.5 mL glass vial for a second magnetic extraction step to further concentrate the sample.

The isolated MagNanoTrap-NPs complex was treated with 37% HCl at 65 °C for 30 minutes, followed by filtration through a 10 kDa centrifugal filter (PES, VWR, UK) to remove the acid. The aggregation was resuspended in methanol and transferred to a Py-GCMS sampling cup for further analysis. The recovery rate ($R_2$) of the spiked assay was calculated using Equation (7):

$$R_2 = \frac{m_2 - m_1}{m_0} * 100\% \quad (7)$$

where $m_0$ is the amount of NPs spiked, $m_1$ is the amount of NPs detected before spiking, and $m_2$ is the amount of NPs detected after spiking.

### 2.14 Human kidney samples collection and treatments

A total of 139 human kidney samples from three groups were obtained through collaboration with Uniklinik Aachen. The samples were stored at –80 °C without undergoing any embedding procedures. Before analyzing MP/NPs in the kidney tissue via Py-GC/MS, the samples were digested using a modified protocol based on previously published methods.[32, 182-184] In brief, 68% nitric acid was added to the kidney samples at a ratio of 1.0 mg tissue to 50 mL of acid solution. This mixture was placed in GC sampling glass bottles sealed with PTFE caps and

incubated on a benchtop orbital shaker at 120 rpm for three days at room temperature to ensure complete digestion of the tissue.

After digestion, the solution was transferred directly into Py-GC/MS sampling cups and placed on a heating block at 65 °C. The glass bottles were then rinsed with 200 µL of deionized water, and the rinse was added to the sampling cups for drying. To further recover any remaining MP/NPs, the bottles were also rinsed with 200 µL of methanol. Once the sampling cups had cooled, the methanol was transferred to the cups and evaporated at 50 °C. The samples were then ready for Py-GC/MS analysis.

### 2.15 Py-GC/MS method and plastics analysis

Py-GC/MS measurements were performed by a Multi-Shot Micro-furnace Pyrolyzer EGA/PY-3030D equipped with an Auto-Shot Sampler (AS-1020E) from Frontier Laboratories (Fukushima, Japan), coupled to an Agilent 8890 gas chromatography (Santa Clara, CA) linked with an Agilent 7000D mass-spectrometer detector. Py-GC/MS running parameters were modified based on protocols established in previous studies.[18, 19, 69, 73] Briefly, samples were analyzed using single-shot pyrolysis with a split ratio of 30:1. The pyrolysis temperature was set at 590 °C for 0.3 min, and the interface temperature was set at 300 °C. The system is applied with a 30 m × 0.25 mm I.D., 0.25 µm film Ultra Alloy 5 capillary column (Frontier Laboratories), with helium as the carrier gas (1.0 mL/min, constant velocity). Additional conditions included: oven ramp from 40 °C (2 min hold) to 320 °C at 20 °C/min (14 min hold); injection port at 300 °C; ion source at 230 °C; 70 eV ionization voltage; and a full scan mass range of m/z 10–550 (Table 1).

**Table 1. Conditions for single-shot Py-GC/MS measurements.**

| | |
|---|---|
| **Micro-furnace pyrolyzer** | Frontier EGA/PY-3030D |
| Carrier gas | Helium |
| Pyrolysis time | 0.3 min |
| Pyrolysis temperature | 590 °C |
| Interface temperature | 300 °C |
| **Gas chromatograph** | Agilent 8890 GC System |
| Column | Frontier Ultra Alloy 5; 30 m, 0.25 mm I.D., 0.25 µm film thickness |
| Column flow | 1 mL/min |
| Injector port temperature | 300 °C |
| Temperature program | 40 °C (2 min) ⟶ 320 °C (20 °C/min, 14 min) |
| Split mode | 30:1 |
| **Mass spectrometer** | Agilent 7000D GC/TQ |
| Ionization energy | 70 eV |
| Scan range | 10-550 m/z |
| Ion source temperature | 230 °C |

For plastics analysis, specific indicator compounds and ions are required to enable the identification and quantification of individual nanoplastic polymer types in environmental samples using Py-GC/MS. The characteristic pyrolysis products of each target nanoplastic were determined by analyzing their corresponding analytical standards or reference materials through Py-GC/MS. The resulting pyrograms were compared against existing literature and an in-house customized database.[18, 19, 69, 73] Since the MagNanoTrap system involved peptides that can cause a strong background for PVC analysis, PVC was out of consideration for the detection and quantification in environmental water samples. Specific indicator ions for the target NPs were then selected based on established criteria and the peptide background, especially for the analysis with MagNanoTrap-enriched samples.

External calibration curves were established by analyzing varying amounts (0.5 mg, 1 mg, 1.5 mg, 2 mg, and 2.5 mg) of the standard mixture (MPs-$SiO_2$-low set provided by Frontier Laboratories). Polymer identification within samples was confirmed by matching specific ions of each target plastic type. The Py-GC/MS method was validated by assessing linearity ($R^2$), limit of detection (LOD), and limit of quantification (LOQ), where LOD and LOQ were defined as signal-to-noise ratios of 3 and 10, respectively. Further details regarding the selected indicator ions, calibration curves, and corresponding LODs and LOQs are discussed in the Results and Discussion section (Tables 5 and 10).

### 2.16 MPs fluorescence detection in human kidney samples

The kidney samples were sectioned to a thickness of approximately 20 µm and mounted onto glass slides. To stain cell nuclei, a diluted working solution of the fluorescent dye DAPI was applied to the fixed tissue sections. The samples were incubated in the DAPI solution for 10 minutes, then rinsed with phosphate buffer (50 mM, pH 7). Next, the "plastibody" solution, comprising the material-binding peptide LCI_F16C conjugated with Alexa 647, was added to the samples to label MP/NPs.[58] The tissue sections were incubated in the plastibody solution for another 10 minutes, followed by a wash with Tris buffer (50 mM, pH 8). After this preparation, the samples were ready for fluorescence imaging using a confocal microscope.

### 2.17 SBR NPs degradation through ethenolysis after enrichment

Before the ethenolysis process, an upscaled enrichment of SBR NPs was conducted. Specifically, the prepared SBR NPs (15.1 mg) were mixed with film-coated $Fe_3O_4$ nanoparticles (4 or 8 mg) in 10 mL of 500 mM sodium chloride solution. The mixture was shaken for 10 minutes to allow saturated adsorption, after which the resulting microaggregates

were separated using an external magnetic field. These aggregates were then transferred into a mixture of THF and p-xylene (1:1, 4 mL) and sealed in a finger-autoclave. Ethylene gas was introduced at 25 bar under continuous stirring until pressure equilibrium was reached. The reaction mixture was stirred at 80 °C for 12 hours. Following the reaction, the $Fe_3O_4$ particles were removed, and the resulting solution was analyzed using $^1H$ NMR spectroscopy.

## 2.18 QC/QA

Strict quality assurance and control measures were implemented throughout all stages of nanoparticle sample collection, pretreatment, extraction, and analysis, with particular attention given to minimizing environmental contamination.[185, 186] While wastewater extraction and pretreatment were conducted in a standard laboratory setting, critical steps such as sample loading and drying were performed inside a fume hood. Laboratory personnel wore cotton lab coats and polymer-free nitrile gloves, which were thoroughly washed prior to use. To prevent airborne contamination, samples were covered with aluminum foil pre-cleaned using dichloromethane when not being actively processed. All stainless-steel membranes, glass bottles, separation funnels, and vacuum filtration devices were rinsed three times with ultrapure water before use. Although certain plastic items, such as ultrafiltration membranes, centrifuge tubes, and pipette tips, were necessary, they were also rinsed thoroughly three times with ultrapure water. For Py-GC/MS analysis, only new, single-use pyrolysis cups were employed to eliminate the risk of cross-contamination.

# 3 Results and discussions

## 3.1 MagNanoTrap for NPs enrichment, detection, and quantification

In a circular polymer economy, the environmental presence of NPs is expected to rise sharply, as increasing volumes of synthetic polymers are directed toward biodegradation or recycling.[6] These processes inevitably release vast quantities of NPs.[7, 8] Hydrophobic NPs, in particular, are known to act as carriers for toxic hydrophobic substances, such as polycyclic aromatic hydrocarbons (PAHs), plastic additives, and pharmaceuticals, posing significant risks to both ecological systems and human health.[27]

Given their typically low concentrations in environmental water bodies, there is an urgent need for effective enrichment methods capable of capturing a broad spectrum of NP types, especially in complex water matrices. Until now, membrane-based techniques have been the only broadly applicable approach reported for MP/NP monitoring in environmental water samples.[18, 19, 69, 73] These systems include cross-flow setups[18, 73] requiring 50 liters of water and dead-end filtration systems[19, 69] processing 1-liter samples. Both formats utilize PES membranes with a 0.01 µm cutoff and rely on Py-GC/MS for analysis of mixed plastic types such as PP, PE, PS, PET, PMMA, PC, Nylon 6, and Nylon 66, achieving recoveries greater than 50%.

Although these membrane-based approaches can efficiently concentrate NPs above the cutoff threshold, particles smaller than the membrane pores can pass through undetected. This is concerning because such ultra-small NPs, particularly those under 20 nm, can cross biological barriers like the blood-brain barrier and may lead to severe neurological effects.[37, 38]

To address this limitation, we developed and validated a new enrichment platform called MagNanoTrap, which utilizes a bifunctional peptide (LCI-DZ-MBP1) immobilized on superparamagnetic iron oxide nanoparticles. This platform effectively captures NPs across seven different types of environmental water samples and, when paired with Py-GC/MS, enables detection and quantification of eight common NP types (Figure 6).

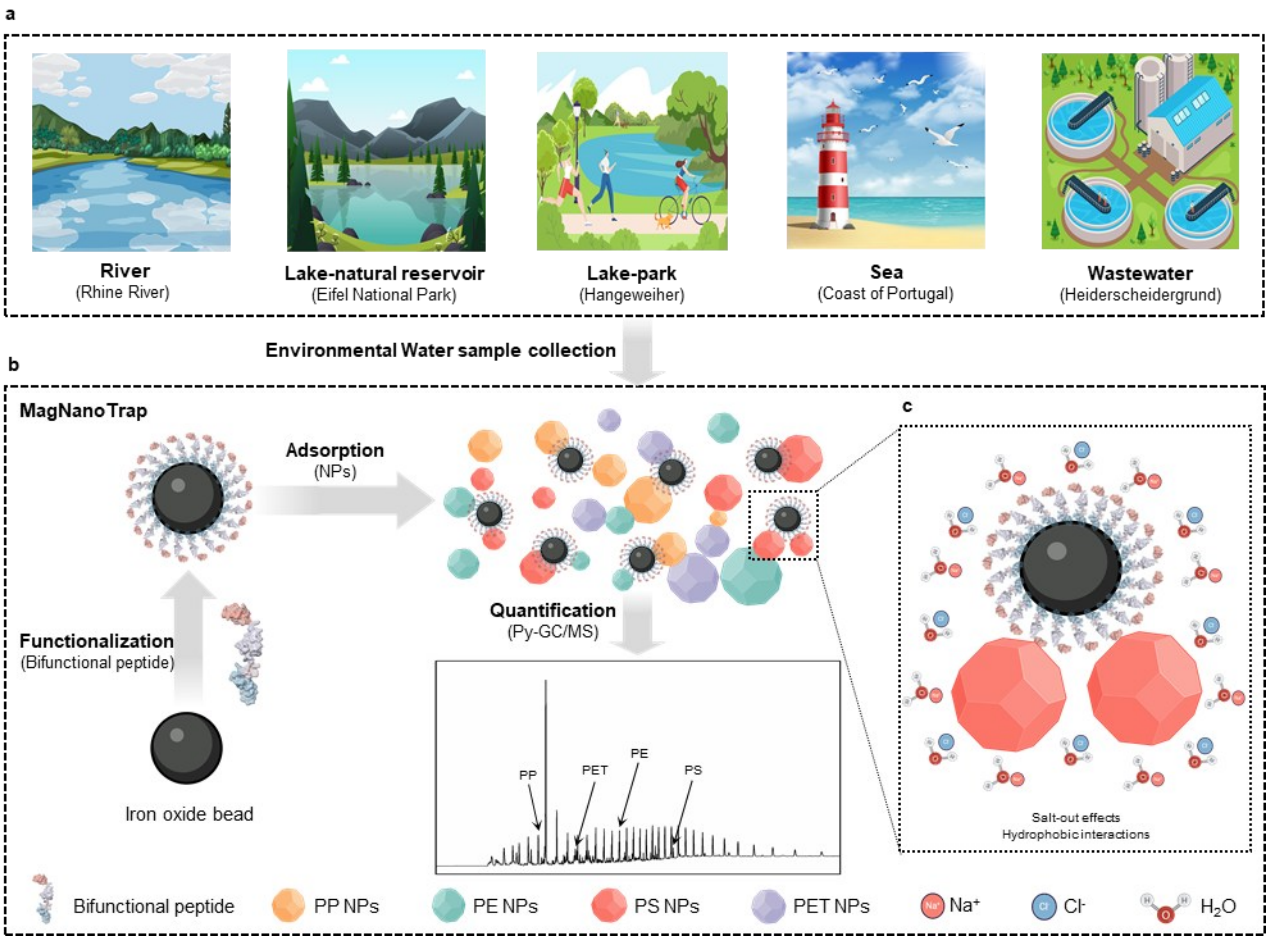


**Figure 6. Overview of MagNanoTrap monitoring platform for NPs enrichment and quantification in environmental water samples. a,** Origins of the environmental water samples analyzed in this study. **b,** Overview of the MagNanoTrap enrichment platform used to detect and quantify nanoplastic contamination in water samples via Py-GC/MS. Step 1 involves functionalizing SPIONs with the bifunctional peptide LCI-DZ-MBP1; step 2 captures NPs (PP, PE, PS, and PET) using the MagNanoTrap beads; and step 3 determines the composition and concentration of NPs through Py-GC/MS analysis. **c,** Illustration of the salt effect that enhances nanoplastic capture by MagNanoTrap beads.

To develop and validate the MagNanoTrap monitoring platform for NPs, the following steps were undertaken to characterize and assess its performance: (A) Functionalization of iron oxide beads, including identification of MBPs that bind to SPIONs as well as PP, PE, PS, and PET plastic surfaces; (B) Enrichment of PS NPs to evaluate key parameters such as iron oxide concentration, peptide concentration, and peptide functionalization duration; (C) Investigation of the effects of NaCl concentration and various cations on enrichment efficiency; (D) Assessment of recovery rates using the MagNanoTrap platform for 1 L water samples spiked with PP, PE, PS, and PET NPs, followed by Py-GC/MS analysis; and (E) Validation of the MagNanoTrap platform for quantifying NPs in environmental water samples via Py-GC/MS.

### 3.1.1 Custom design of bifunctional peptide LCI-DZ-MBP1

As illustrated in Figure 7, a biofunctionalized iron oxide bead was constructed using the bifunctional peptide LCI-strep-DZ-MBP1. In this design, the LCI peptide binds to the iron oxide surface, followed by a strep tag for purification and a linker DZ composed of three parallel α-helices. The MBP1 peptide is presented at the outermost layer, allowing it to bind effectively to a variety of plastic surfaces.

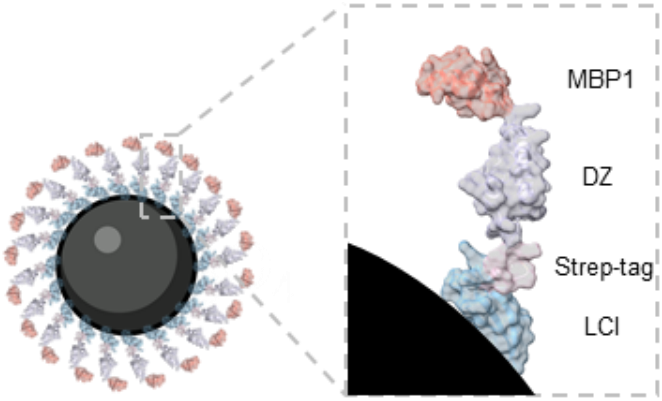


**Figure 7. Scheme showing the bifunctional peptide LCI-DZ-MBP1 decorated iron oxide bead.** Peptide LCI binds to SPION surface, and peptide MBP1 acts as a universal plastic-binder.

The bifunctional peptide LCI-strep-DZ-MBP1 has a height of 8.5 nm, as determined using PyMOL, enabling the formation of a thin bio-coating layer on the surface of the iron oxide beads (Figure 8).

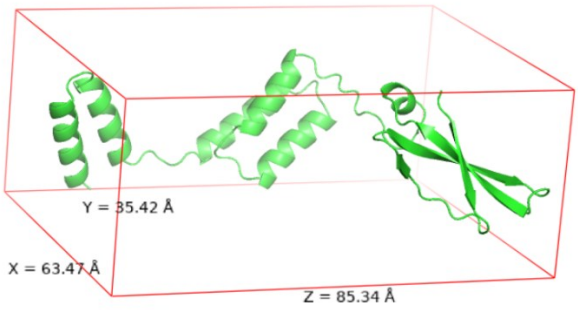


**Figure 8. Predicted size of LCI-strep-DZ-MBP1 bifunctional peptide by PyMOL.** It demonstrates the nanolayer coating on the SPION surface.

The bifunctional peptide LCI-strep-DZ-MBP1, along with its individual components (LCI-strep-DZ and strep-DZ-MBP1), was expressed in *E. coli* BL21 (DE3) using the pET-28a(+) vector. Following sonication and centrifugation, both the supernatant and pellet fractions were analyzed by SDS-PAGE to assess protein expression. The purified proteins were also loaded for evaluation of purity (Figure 9). The calculated molecular weights, 13 kDa for LCI-strep-DZ, 12 kDa for strep-DZ-MBP1, and 17 kDa for LCI-strep-DZ-MBP1, were consistent with the SDS-PAGE results.

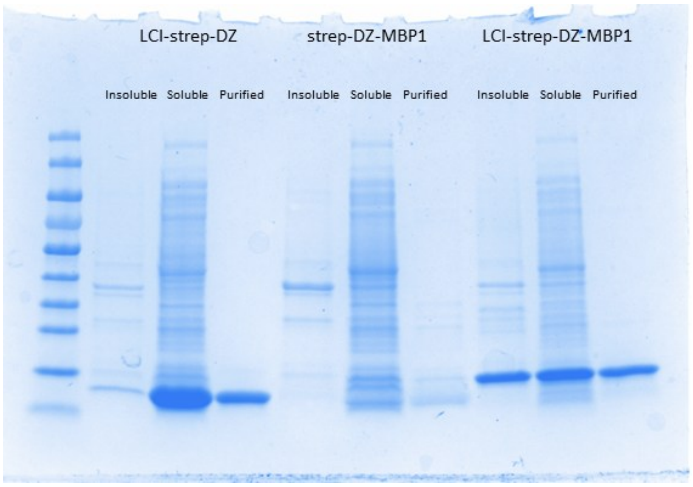


**Figure 9. SDS-PAGE of peptide LCI-strep-DZ, strep-DZ-MBP1, and LCI-strep-DZ-MBP1.** From left to right, the lanes represent the insoluble, soluble, and purified fractions of each respective construct.

The binding affinity of each fusion protein to the iron oxide surface was evaluated using a fluorescently labeled streptavidin dye, which specifically interacts with the strep-tag present in the constructs LCI-strep-DZ, strep-DZ-MBP1, and LCI-strep-DZ-MBP1 (Figure 10). In detail, following peptide decoration of the beads, 0.5 µL of Strep-Tactin®XT DY-649 was added to the bead suspension in Tris-HCl buffer (50 mM, pH 8) and shaken at 1200 rpm for 2 minutes. The beads were then washed twice with Tris buffer using magnetic separation. As a negative control, Alexa dye was mixed with unmodified iron oxide beads to confirm that the dye alone does not bind non-specifically. The results showed that the LCI domain in the LCI-strep-DZ fusion protein successfully binds to the iron oxide surface, whereas the MBP1 domain in strep-DZ-MBP1 did not produce a detectable fluorescence signal. The binding of the custom-designed bifunctional peptide LCI-strep-DZ-MBP1 to iron oxide was also confirmed through this fluorescence-based assay.

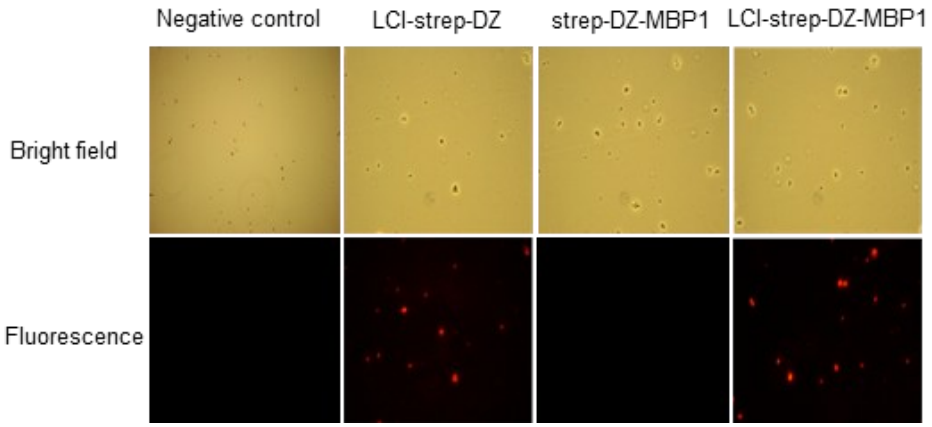


**Figure 10. Microscope images demonstrating the decoration of iron oxide beads with single peptides (LCI-strep-DZ and strep-DZ-MBP1) and the bifunctional peptide LCI-strep-DZ-MBP1.** Images under a bright field are shown on top, and images under a fluorescent field are shown at the bottom. It shows that only LCI is

the binder for SPIONs, indicating a good peptide design to avoid agglomeration during the functionalization process.

Further binding studies demonstrated that peptide MBP1, on the other side of the bifunctional peptide LCI-strep-DZ-MBP1, exhibits strong affinity toward a broad spectrum of synthetic polymers, including PP, PE, PS, and PET (Figure 11). To visualize the interaction, the strep-DZ-MBP1 peptide binding on the plastic surface was specifically labelled using the fluorescent dye Strep-Tactin®XT DY-649. Fluorescence analysis, using the dye alone as a negative control to rule out nonspecific staining of plastic surfaces, confirmed that the MBP1 peptide successfully bound to the surfaces of PP, PS, PE, and PET.

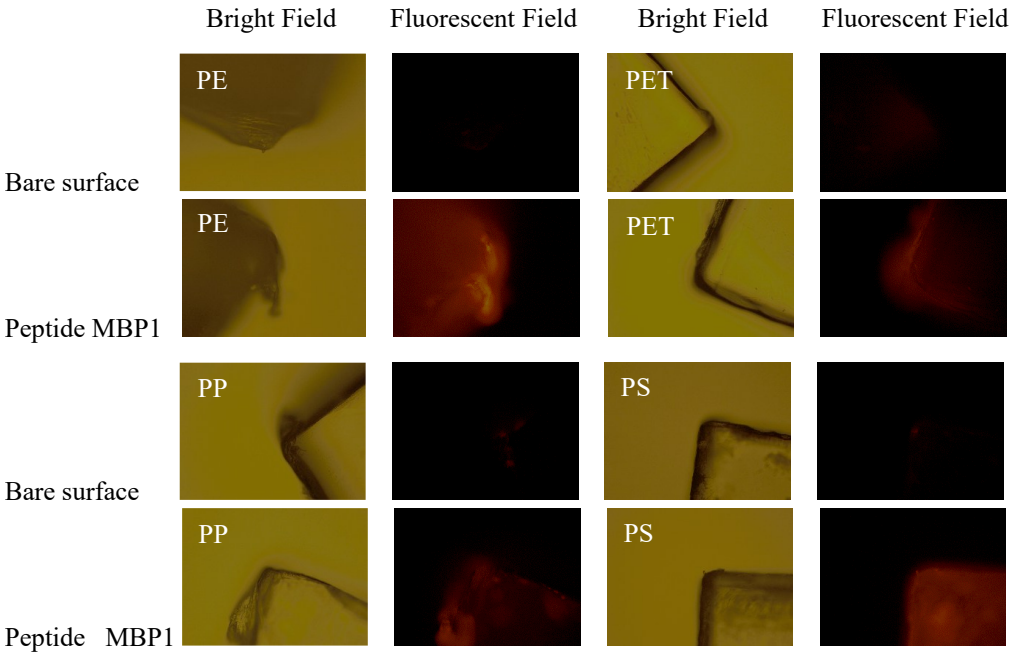


**Figure 11. Binding of peptide MBP1 to plastic surfaces.** Fluorescence analysis was performed to assess the binding of the MBP1 domain from strep-DZ-MBP1 to the surfaces of PP, PE, PS, and PET. It shows that MBP1 is the universal plastic-binder.

These binding results, confirmed by fluorescence, demonstrate that the combination of LCI and MBP1 forms an effective bifunctional peptide design for the development of the MagNanoTrap platform.

### 3.1.2 Preparation of PP, PE, and PET NPs

All NPs, including commercially available PS NPs with both positive and negative charges in sizes of 100 nm, 500 nm, and 1000 nm, as well as self-synthesized PP and PE NPs (via emulsification) and PET NPs (via nanoprecipitation), were characterized using DLS for size distribution, zeta potential measurements for surface charge, and SEM for morphological

analysis (Figure 12). The self-synthesized NPs in particular exhibited negative surface charges, sizes below 1 µm, and spherical morphology.

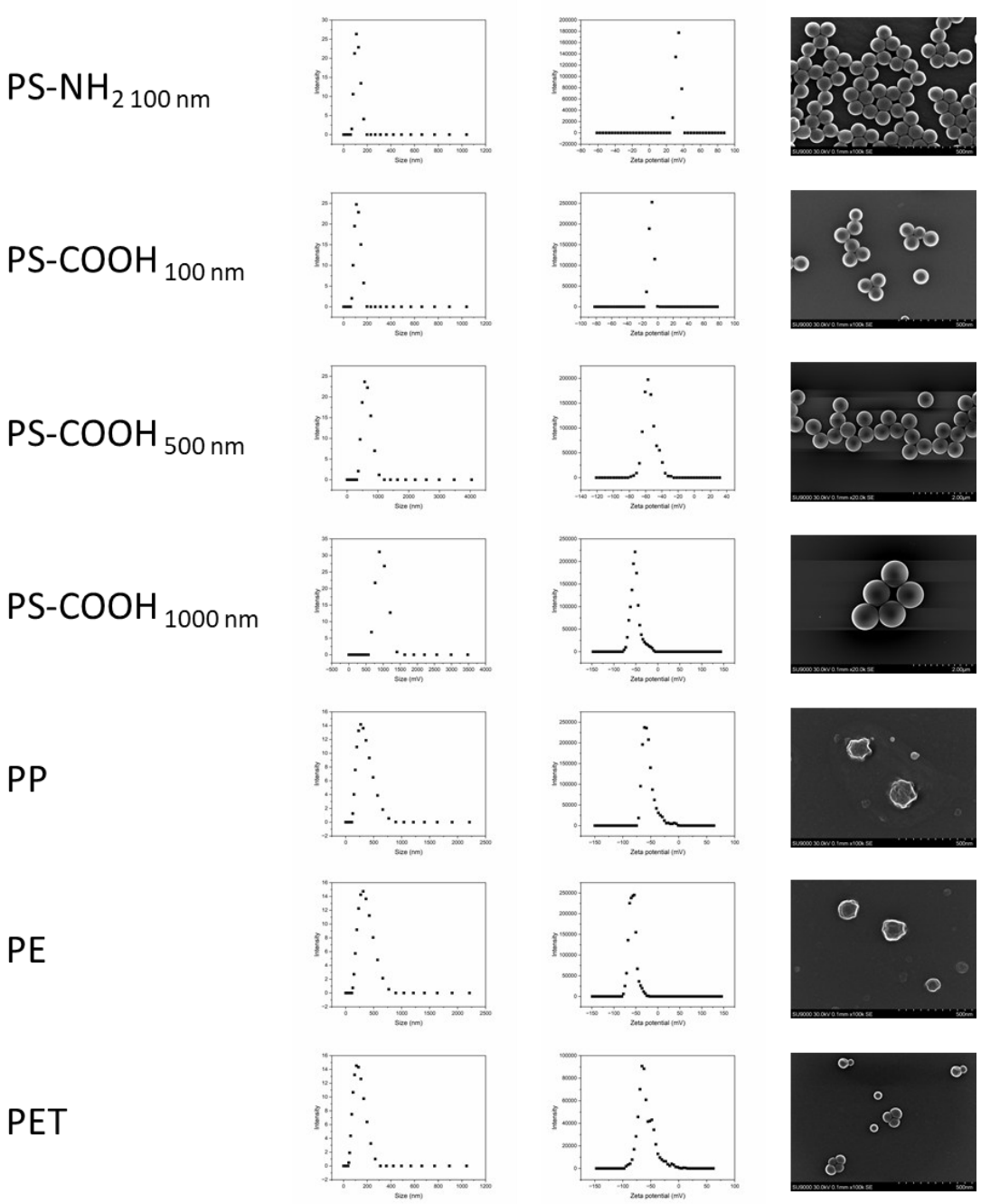


**Figure 12. Commercial and self-made NPs characterization.** DLS (left), Zeta potential (middle), and SEM (right) of commercial PS NPs and self-made PP, PE, and PET NPs. All of the NPs are negatively charged and in nano-size.

### 3.1.3 Investigation of successful peptide decoration by material characterization

Decoration of iron oxide beads with the bifunctional peptide was accomplished by simply suspending the beads in a peptide solution at room temperature, followed by a brief 1-minute incubation and a subsequent water wash. As described before, the LCI-strep-DZ-MBP1 peptide bound to the iron oxide surface was further labelled with the fluorescent dye Strep-Tactin®XT

DY-649. From FACS analysis, a clear fluorescence signal shift was detected in the peptide-coated MagNanoTrap beads, indicating successful functionalization of the iron oxide beads with more than 98% efficiency after a simple and fast shaking process (Figure 13).

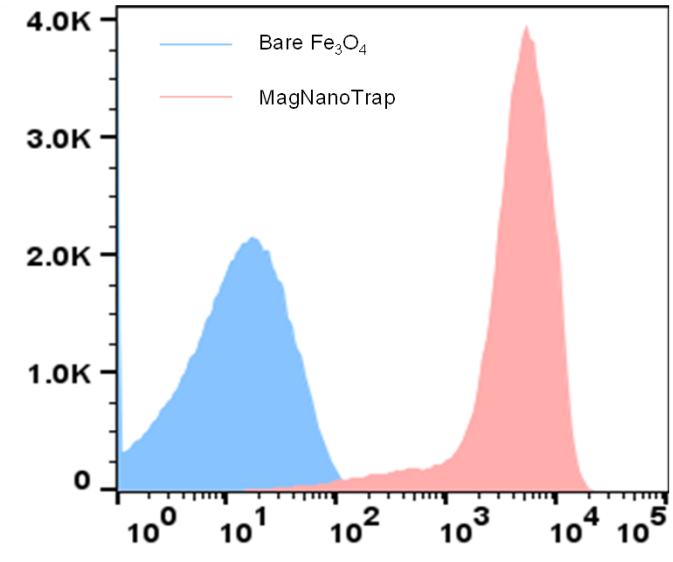


**Figure 13. FACS analysis of MagNanoTrap and bare iron oxide.** Bare iron oxide beads are shown in blue, and MagNanoTrap beads are shown in red. The obvious shift demonstrates effective functionalization of the beads.

Morphology and size distribution of iron oxide beads before and after functionalization were assessed using SEM and DLS (Figure 14). DLS analysis confirmed that MagNanoTrap beads remained well-dispersed without aggregation and exhibited an increased hydrodynamic radius from 550 nm to 680 nm, as anticipated. SEM images revealed that the iron oxide nanoparticles formed homogeneous aggregates before peptide decoration, and the peptide nano-layer didn't induce further aggregation.

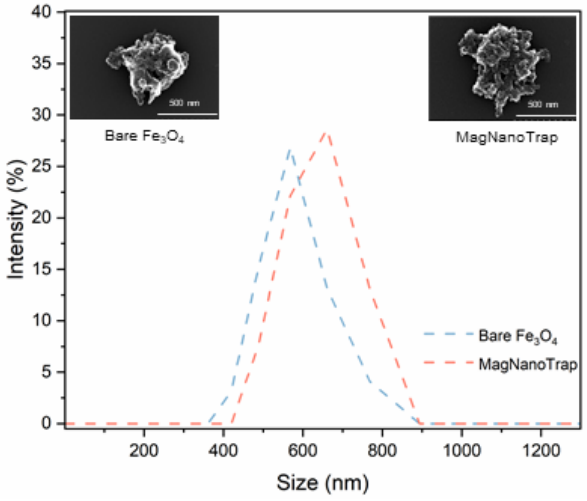


**Figure 14. DLS and SEM images of iron oxide beads before and after functionalization.** The size distribution of bare iron oxide is shown in blue, and that of the MagNanoTrap beads is shown in orange. The top left and right panels are the SEM images of iron oxide before and after functionalization. The nanocoating doesn't influence the amorphology and doesn't form aggregates.

TGA was performed by gradually increasing the temperature from 100 °C to 800 °C. The observed mass loss reflects the presence of an organic coating on the iron oxide surface. A significant mass reduction in MagNanoTrap beads (13.7%) compared to bare iron oxide (2.7%) confirmed successful peptide decoration (Figure 15). Additionally, the derivative TGA curve revealed an extra peak at 360 °C in the MagNanoTrap sample, further indicating the presence of the peptide coating.

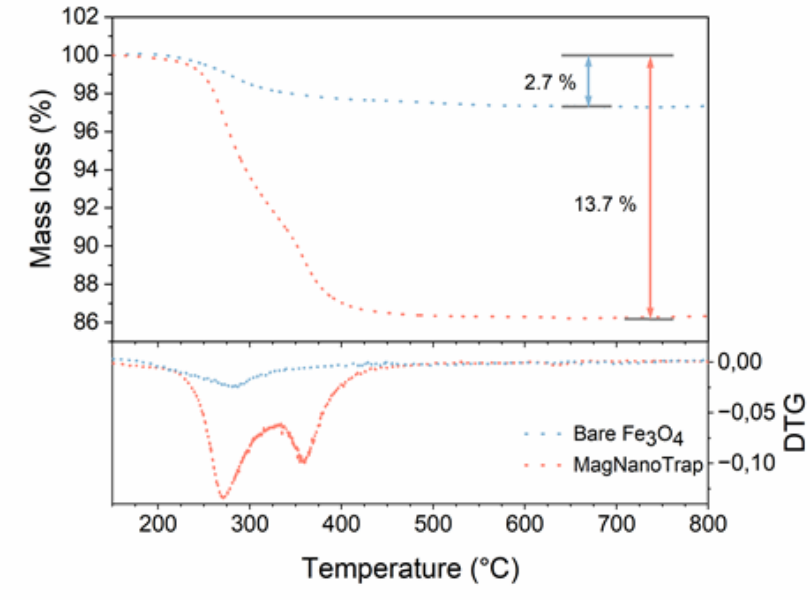


**Figure 15. TGA measurements of iron oxide before and after functionalization.** The mass loss of bare iron oxide is shown in blue, and that of MagNanoTrap beads is shown in orange. The derivatives of mass loss curves are presented at the bottom. The mass loss and one more peak showing in the derivative curve indicate the successful peptide decoration.

ESI-MS analysis was carried out to further verify the peptide decoration of the iron oxide beads (Figure 16). A distinct signal corresponding to the LCI-DZ-MBP1 peptide was detected in the MagNanoTrap beads. The observed molecular weight closely matched the expected size of 17.49 kDa, as previously determined by SDS-PAGE, confirming the successful peptide functionalization of the iron oxide surface.

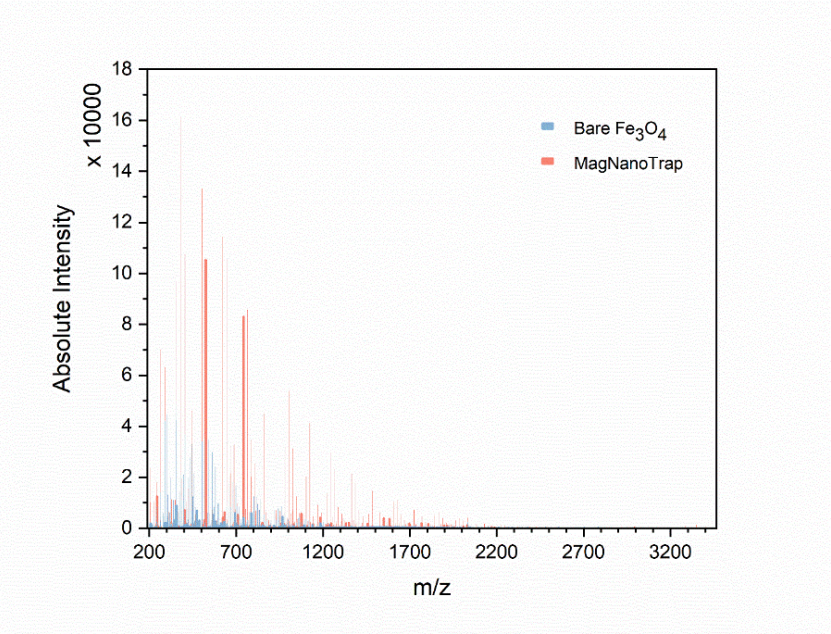


**Figure 16. ESI-MS analysis of iron oxide before and after functionalization.** The ionic fragments from bare iron oxide are shown in blue, and those from MagNanoTrap are shown in orange. The calculated molecular weight from the ESI-MS matches the SDS-PAGE results, demonstrating the successful peptide coating.

XPS analysis further validated the successful attachment of LCI-strep-DZ-MBP1 to the iron oxide surface through surface chemistry characterization (Figure 17). Specifically, in the O 1s spectra, both bare and decorated iron oxide showed peaks at 529.7 eV and 531.2 eV, corresponding to $O^{2-}$ and $OH^-$ groups from $Fe_3O_4$. Notably, the MagNanoTrap spectrum revealed an additional peak at 532.3 eV, characteristic of the peptide bond (-CONH-), indicating the presence of the peptide on the iron oxide surface.

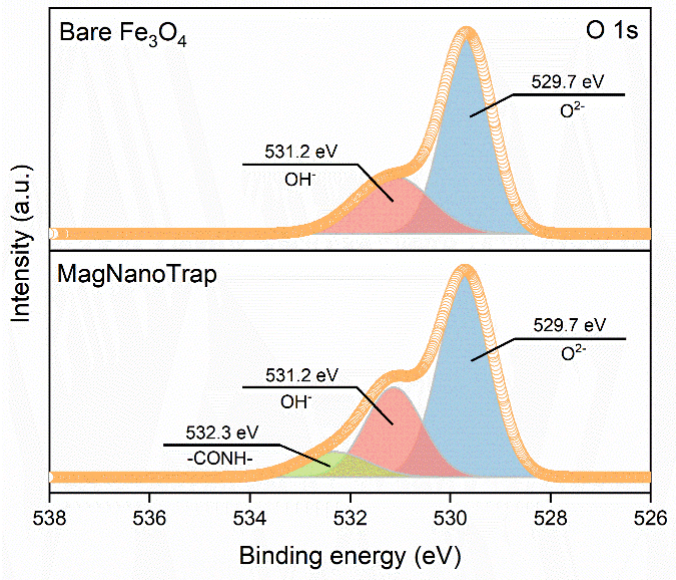


**Figure 17. XPS spectra (O 1s) of iron oxide before and after functionalization.** The spectra of bare iron oxide are shown on top, and those of MagNanoTrap are shown at the bottom. The signal of -CONH- bond indicates the successful peptide coating.

FTIR analysis provided further insight into the surface chemistry of the iron oxide (Figure 18). The bare iron oxide displayed some peaks that might be introduced on the iron oxide surface during the chemical synthesis process. Upon peptide functionalization, a significant increase in the peak associated with the N–H stretch of the Amide I bond was observed, confirming the successful attachment of the peptide to the iron oxide surface.

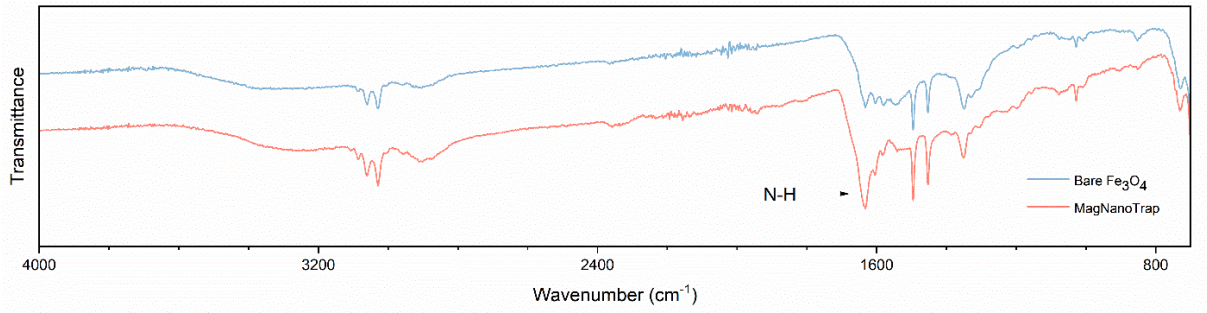


**Figure 18. FTIR analysis of iron oxide before and after functionalization.** The spectrum for bare iron oxide is shown in blue, and that for MagNanoTrap is shown in orange. The -NH bond signal indicates the peptide coating.

The magnetization curve obtained using a VSM demonstrated that the thin peptide nanolayer had a negligible impact on the magnetic moment and superparamagnetic properties of the iron oxide nanoparticles (Figure 19). This preserved magnetic behavior enabled rapid recovery of the NPs upon application of an external magnetic field.

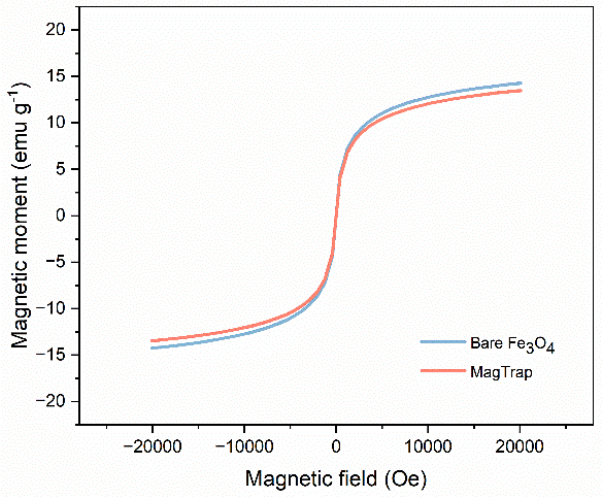


**Figure 19. Magnetization curve of iron oxide before and after functionalization.** The bare iron oxide is shown in blue, and the decorated iron oxide is shown in orange. The peptide nanocoating doesn't influence the superparamagnetic properties of SPIONs.

The above characterization confirms the successful functionalization of iron oxide beads with the bifunctional peptide LCI-DZ-MBP1, leading to the formation of MagNanoTrap beads, which will be employed in the following steps for NPs enrichment from water samples.

### 3.1.4 Evaluation of NPs enrichment performance by MagNanoTrap system in a 200 µL-scale reaction

Enrichment experiments using PS, PP, PE, and PET nanoparticles were conducted on a 200 µL scale to evaluate the efficiency and broad applicability of the MagNanoTrap enrichment system. Figure 20 outlines the four-step workflow established to assess the enrichment performance of the scalable MagNanoTrap technology, utilizing absorbance measurements to quantify enrichment efficiency. In step 1, iron oxide beads were functionalized with LCI-DZ-MBP1 in 50 mM Bicine buffer at pH 9; in step 2, the functionalized MagNanoTrap beads were rinsed with water and then incubated with NPs in the presence of 150 mM NaCl; in step 3, the MagNanoTrap-NP complexes were separated using a magnet; and in step 4, the remaining supernatant containing unbound NPs was collected for absorbance analysis.

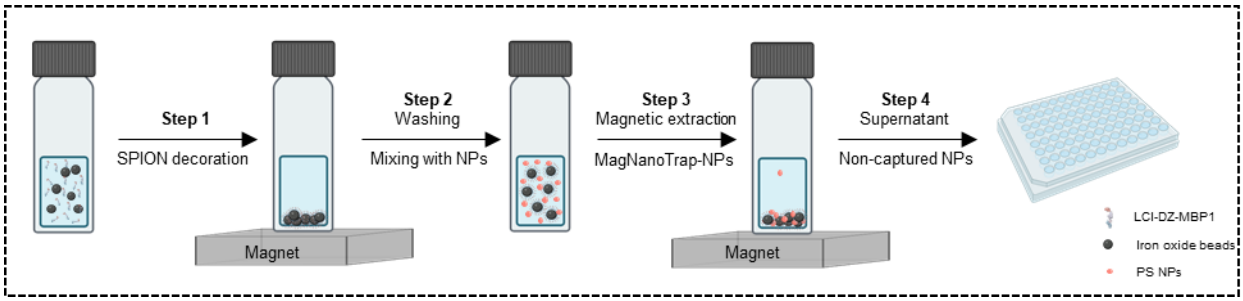


**Figure 20. Scheme of the four-step workflow developed for assessing the enrichment performance of MagNanoTrap technology on a 200 µL scale.** In step 1, SPIONs were decorated with LCI-DZ-MBP1 in 50 mM Bicine, pH 9; in step 2, the MagNanoTrap beads were washed with water, followed by mixing with NPs in the presence of 150 mM NaCl; in step 3, the MagNanoTrap-NPs complex was extracted by a magnet; and in step 4, the supernatant containing non-captured NPs was taken for absorbance measurement.

Before conducting the enrichment experiments, an absorbance-based quantification method was established for PS NPs. For each PS NP variant, differing in size and surface charge, a range of concentrations was analyzed across the full UV spectrum. The optimal wavelength that provided the best linear correlation within the relevant concentration range was selected for quantification. The selected wavelengths and corresponding plastic types are summarized in the table below, along with their respective calibration equations, all exhibiting a linearity ($R^2$) greater than 0.99 (Table 2). These calibration curves were subsequently used for quantifying PS NPs in a 200 µL scale enrichment and calculating recoveries.

**Table 2. Calibration curves of PS NPs with different sizes and charges characterized by absorbance measurement.**

| Plastic type | Wavelength | Linear range (g/L) | Calibration equation | Linearity ($R^2$) |
|---|---|---|---|---|
| PS-COOH $_{100\ nm}$ | 350 nm | 0.00625-0.4 | y=1.2586x-0.0053 | 0.9999 |
| PS-$NH_2$ $_{100\ nm}$ | 340 nm | 0.00625-0.2 | y=1.6657x-0.0018 | 0.9998 |
| PS-COOH $_{500\ nm}$ | 460 nm | 0.003125-0.2 | y=5.4455x+0.0041 | 0.9998 |
| PS-COOH $_{1000\ nm}$ | 550 nm | 0.003125-0.2 | y=4.6207x-0.0120 | 0.9990 |

The enrichment optimization involved evaluating several key parameters to understand their effects on the recovery of PS-$COOH_{500\ nm}$ NPs: the optimal concentration of iron oxide beads (Figure 21), the required amount of LCI-DZ-MBP1 for effective iron oxide beads decoration (Figure 22), the minimal incubation time needed for efficient peptide attachment (Figure 23), and the optimal NaCl concentration for the enrichment of NPs (Figure 24). Across all experiments, iron oxide beads were decorated using 5 µM LCI-DZ-MBP1 for 1-minute shaking to ensure saturated decoration. A 20-minute shaking process was used to maximize the capture of PS-$COOH_{500\ nm}$ NPs, with 150 mM NaCl added in Step 2, unless otherwise noted. As illustrated in Figure 21, using 0.3 g/L of peptide-decorated iron oxide beads enabled efficient recovery of 0.2 g/L PS-$COOH_{500\ nm}$ NPs, resulting in a high recovery rate of 96.1 ± 0.3%.

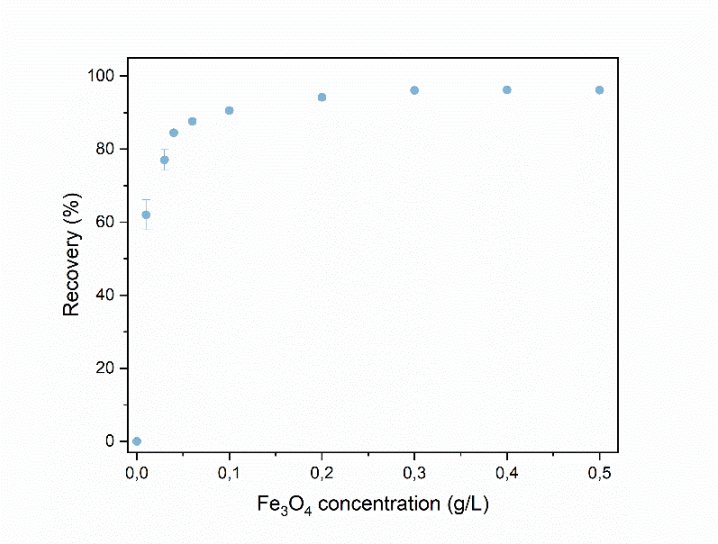


**Figure 21. The recovery of PS-$COOH_{500\ nm}$ determined at increasing MagNanoTrap concentrations.** The recovery reaches the maximum with 0.3 g/L SPIONs.

Using the optimized iron oxide concentration of 0.3 g/L, the peptide concentration for decoration was further refined. As shown in Figure 22, 1 µM of peptide was sufficient to fully functionalize 0.3 g/L of iron oxide beads. The LCI-DZ-MBP1 modification significantly enhanced NPs capture, increasing the recovery rate 10-fold compared to unmodified iron oxide beads.

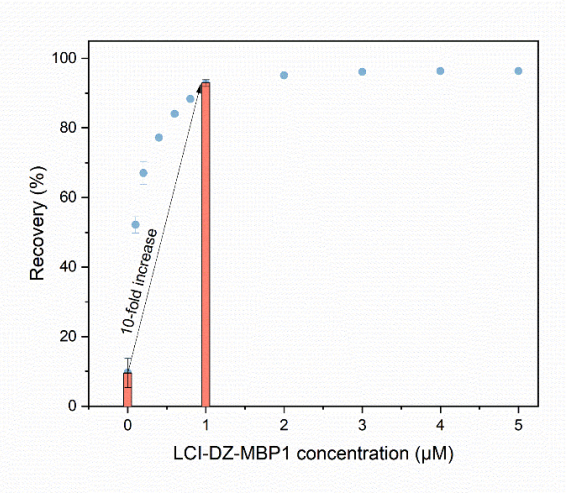


**Figure 22. The recovery of PS-COOH$_{500\ nm}$ determined at increasing LCI-DZ-MBP1 concentration.** The recovery reaches saturation with 1 µM peptide for 0.3 g/L SPIONs. The peptide functionalization improves the recovery by 10-fold.

Using the optimized iron oxide concentration of 0.3 g/L and peptide concentration of 1 µM in the enrichment system, the shaking time for peptide decoration was further investigated. Notably, as illustrated in Figure 23, only 3 seconds of shaking were enough to achieve effective iron oxide decoration, highlighting the advantage of rapid coating using material-binding peptide technology.

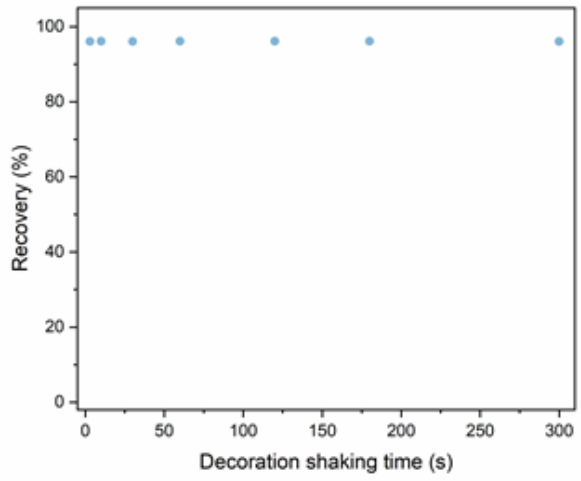


**Figure 23. The recovery of PS-COOH$_{500\ nm}$ determined at increasing peptide decoration shaking time.** The functionalization process by peptide is almost instant, with 3s shaking reaching the maximum recovery.

Peptide concentration and functionalization time were optimized to achieve efficient iron oxide decoration, while NaCl concentration was further adjusted to enhance the interaction between MagNanoTrap beads and PS NPs. Interestingly, enrichment occurred only in the presence of NaCl, with recovery reaching saturation at 150 mM (Figure 24). The effect of salt on these interactions will be explored in more detail in the following section (3.1.5).

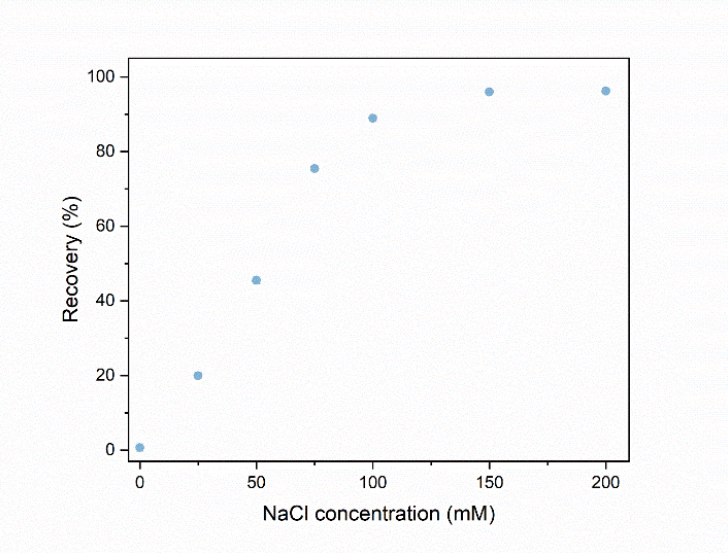


**Figure 24. The recovery of PS-COOH$_{500\ nm}$ determined at increasing NaCl concentration.** Only in the presence of NaCl, the interaction between functionalized SPIONs and PS NPs occurs, with 150 mM NaCl reaching the maximum recovery.

The broad applicability of the MagNanoTrap enrichment platform was evaluated using PS NPs functionalized with either amino (PS-NH$_2$, pKa 9–10) or carboxyl (PS-COOH, pKa 4.75) groups, with the optimized parameters. All experiments were conducted at pH 7, under which PS-NH$_2$ NPs carry a positive charge, while PS-COOH NPs are negatively charged. The adsorption capacities were measured as follows: $494.3 \pm 7.0$ mg/g for PS-NH$_{2\ 100\ nm}$, $607.6 \pm 9.5$ mg/g for PS-COOH$_{100\ nm}$, $639.8 \pm 3.2$ mg/g for PS-COOH$_{500\ nm}$, and $657.5 \pm 6.0$ mg/g for PS-COOH$_{1000\ nm}$ (Figure 25). A clear trend was observed that larger PS-COOH NPs sizes corresponded to increased adsorption capacity.

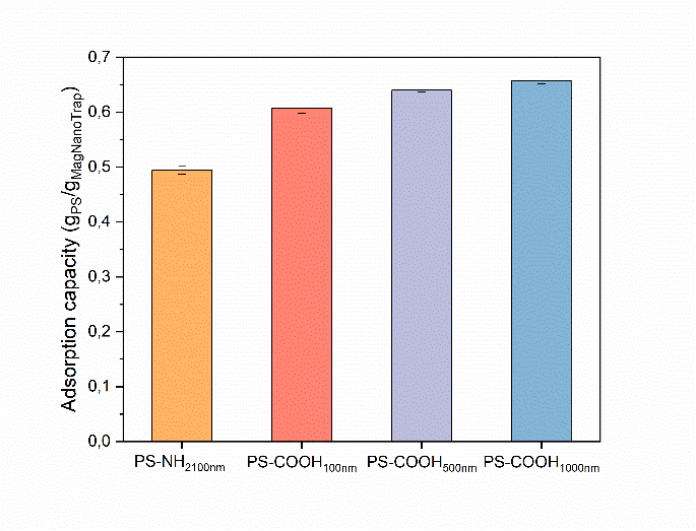


**Figure 25. Adsorption capacity of positively and negatively charged PS NPs with MagNanoTrap beads.** Positively charged PS-$NH_{2\ 100\ nm}$, as well as negatively charged PS-$COOH_{100\ nm}$, PS-$COOH_{500\ nm}$, and PS-$COOH_{1000\ nm}$ NPs, are used for the adsorption capacity. Smaller NPs have relatively larger surface area, with the same NaCl concentration showing less adsorption capacity.

Three additional NPs types, such as PP, PE, and PET, prepared by emulsification-solvent evaporation and nanoprecipitation, were tested to further validate the enrichment efficiency and broad applicability of the MagNanoTrap enrichment platform (Figure 26). Following incubation with MagNanoTrap beads and magnetic separation, the supernatants of all NP suspensions turned completely clear within 1 min, indicating effective and fast removal of the NPs.

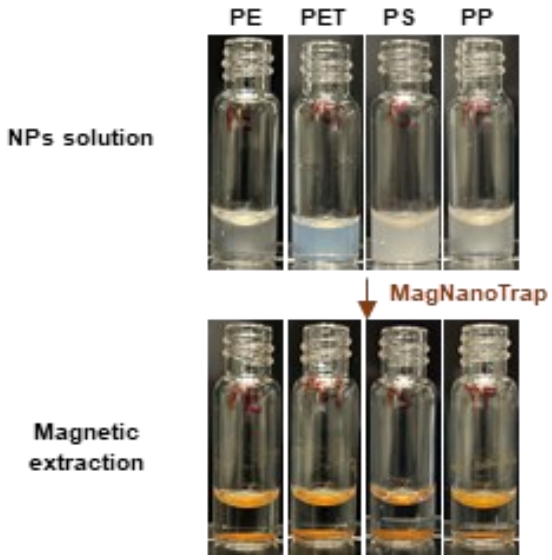


**Figure 26. Visualization of PP, PE, PET, and PS NPs dispersion before and after magnetic extraction.** Plastic dispersion is 0.2 g/L. All NPs solutions turn clear after magnetic extraction.

Moreover, SEM/EDXS imaging of MagNanoTrap beads after capturing PS-$COOH_{500\ nm}$ NPs further confirmed the successful functionalization of SPIONs (yellow color on iron oxide

surface, which is from the peptide) and the effective adsorption of NPs (spherical yellow shape, which represents PS NP; Figure 27).

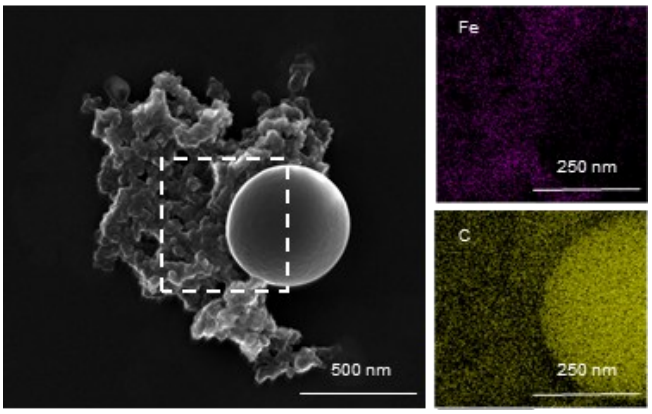


**Figure 27. SEM coupled with EDXS images showing that PS NP was captured by MagNanoTrap beads.** Purple represents Fe elements in iron oxide nanoparticles (top right), and yellow represents C elements in PS NPs and MagNanoTrap beads.

In all, these findings demonstrate the robustness of the biofunctionalized MagNanoTrap as a versatile platform for NPs enrichment.

### 3.1.5 Investigation of NPs adsorption by MagNanoTrap system under the salt effect

Salt concentrations are known to affect protein binding behavior in hydrophobic interaction chromatography.[187] The impact of salt on the binding efficiency of the exposed MBP1 peptide to PS NPs was examined to ensure the broad applicability of the MagNanoTrap enrichment platform. Sodium chloride (NaCl) was chosen to reflect conditions relevant to seawater environments, and NaCl can be supplemented to all kinds of environmental water samples to ensure the efficient adsorption of NPs via the MagNanoTrap enrichment platform. During the adsorption process, NaCl ions likely interfered with the interactions between water molecules and charged groups on the surfaces of both MagNanoTrap beads and PS NPs (Figure 28). Salt effects from NaCl weakened the hydration shell around the nanoparticles, thereby exposing more hydrophobic regions and enhancing hydrophobic interactions.[188]

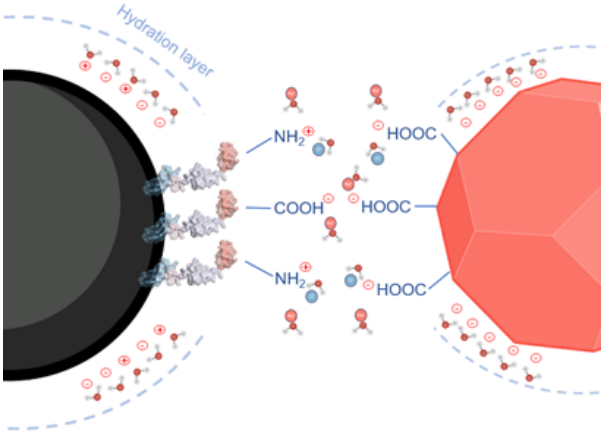


**Figure 28. Scheme illustrating the NaCl effects on NPs adsorption by MagNanoTrap beads.**

The NaCl effects on adsorption kinetics and isotherms were evaluated by introducing varying concentrations of NaCl into the MagNanoTrap enrichment system to gain a clearer understanding of its role in PS NPs adsorption. Kinetic analysis revealed that 0.2 g/L of PS-$COOH_{500\,nm}$ NPs were rapidly adsorbed by 0.3 g/L of MagNanoTrap beads, reaching saturation within 13 minutes (Figure 29). The experimental data exhibited a strong fit with the pseudo-second-order kinetic model, achieving an $R^2$ value above 0.99, in contrast to the lower linearity (~0.97) observed with the pseudo-first-order model. This indicates that the adsorption process is primarily governed by the availability of binding sites.[180] Moreover, the adsorption rate constant ($k_2$) increased significantly with rising salt concentrations, from 1.36 ± 0.16 g/(g·min) at 100 mM NaCl to 4.04 ± 0.29 g/(g·min) at 200 mM, highlighting the key role of NaCl in enhancing adsorption kinetics. In contrast, the equilibrium adsorption capacity ($q_e$) remained relatively stable across conditions, with values of 0.63 ± 0.01 g/g, 0.66 ± 0.01 g/g, and 0.64 ± 0.01 g/g at 100 mM, 150 mM, and 200 mM NaCl, respectively (Table 3).

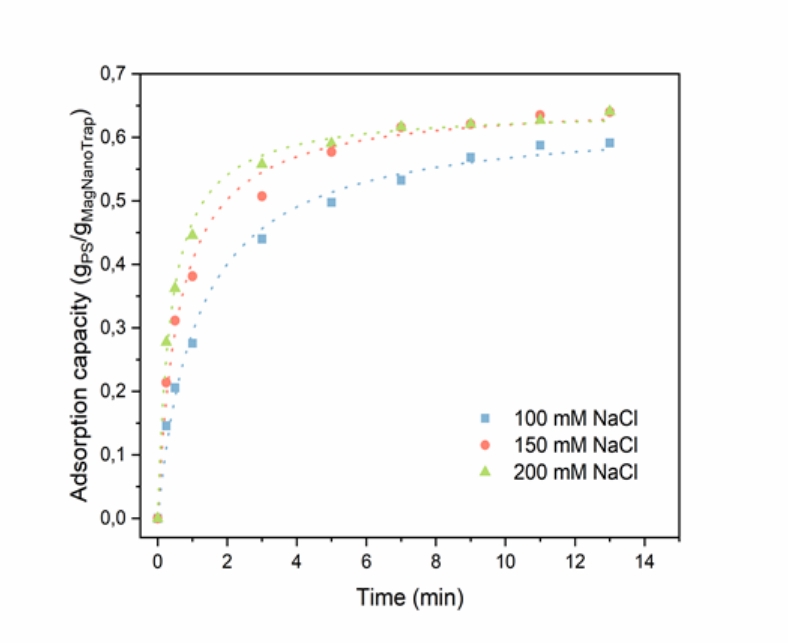


**Figure 29. Adsorption kinetics of the MagNanoTrap platform for PS-COOH$_{500\ nm}$ NPs at different salt concentrations.** Enrichment was performed with 100 mM, 150 mM, and 200 mM NaCl, and the kinetics were fitted with the pseudo-second-order model. The adsorption process is facilitated by the NaCl concentration.

**Table 3. Parameters of the adsorption kinetics equation of MagNanoTrap against PS-COOH$_{500\ nm}$ at different NaCl concentrations.**

| | Pseudo-first-order model | | | Pseudo-second-order model | | |
|---|---|---|---|---|---|---|
| NaCl concentration | $q_e$ (g/g) | $k_1$ (min$^{-1}$) | $R^2$ | $q_e$ (g/g) | $k_2$ (g/(g·min)) | $R^2$ |
| 100 mM | 0.56 | 0.70 | 0.9709 | 0.63 | 1.36 | 0.9934 |
| 150 mM | 0.60 | 1.23 | 0.9623 | 0.66 | 2.44 | 0.9918 |
| 200 mM | 0.61 | 1.79 | 0.9711 | 0.64 | 4.04 | 0.9962 |

In addition to the adsorption kinetic studies, adsorption isotherms were evaluated and fitted using both Langmuir and Freundlich models to investigate the impact of NaCl concentration on the adsorption affinity and maximum capacity of MagNanoTrap for PS-COOH $_{500nm}$ NPs (Figure 30, Table 4).[181] The data aligned closely with the Langmuir model, indicated by correlation coefficients exceeding 0.99, which suggests monolayer adsorption on a homogeneous surface. Notably, the Langmuir constant ($K_L$) increased from 0.85 ± 0.05 L/g at 100 mM NaCl to 1.85 ± 0.21 L/g at 200 mM, reflecting enhanced adsorption affinity with higher salt concentrations. The maximum adsorption capacities ($q_m$) calculated from the model were 3.05 ± 0.08 g/g at 100 mM, 3.80 ± 0.09 g/g at 150 mM, and 3.95 ± 0.14 g/g at 200 mM

NaCl, significantly surpassing those of previously reported adsorbents such as biomass fibrous foam (444.6 ± 22.3 mg/g)[189] and SPIONs-PAC[105] (0.69 ± 0.26 g/g) for PS NPs.

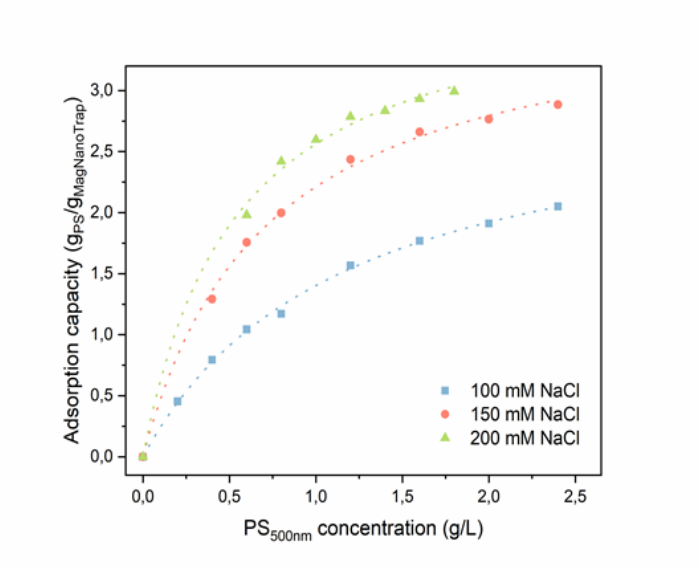


**Figure 30. Adsorption isotherms of the MagNanoTrap platform for PS-COOH$_{500\ nm}$ NPs at different salt concentrations.** Enrichment was performed with 100 mM, 150 mM, and 200 mM NaCl, and the isotherms were fitted with the Langmuir model. The adsorption affinity is higher when more NaCl is supplemented.

**Table 4. Parameters of the adsorption isotherm equation of MagNanoTrap against PS-COOH$_{500\ nm}$ at different NaCl concentrations.**

| | Freundlich model | | | Langmuir model | | |
|---|---|---|---|---|---|---|
| NaCl concentration | 1/n | $K_F$ (L/g) | $R^2$ | $q_m$ (g/g) | $K_L$ (L/g) | $R^2$ |
| 100 mM | 0.54 | 1.33 | 0.9855 | 3.05 | 0.85 | 0.9985 |
| 150 mM | 0.40 | 2.13 | 0.9587 | 3.80 | 1.40 | 0.9981 |
| 200 mM | 0.33 | 2.53 | 0.9331 | 3.95 | 1.85 | 0.9970 |

Interestingly, smaller PS-COOH NPs exhibited lower adsorption capacities compared to larger ones at the same NaCl concentration (Figure 31). For example, with 100 mM NaCl, the adsorption capacities were 517.6 ± 10.6 mg/g for 100 nm PS NPs, 591.2 ± 2.2 mg/g for 500 nm PS NPs, and 649.4 ± 5.2 mg/g for 1000 nm PS NPs. This trend likely results from the higher surface area of smaller NPs, which demands more NaCl to effectively neutralize surface charges and promote adsorption.

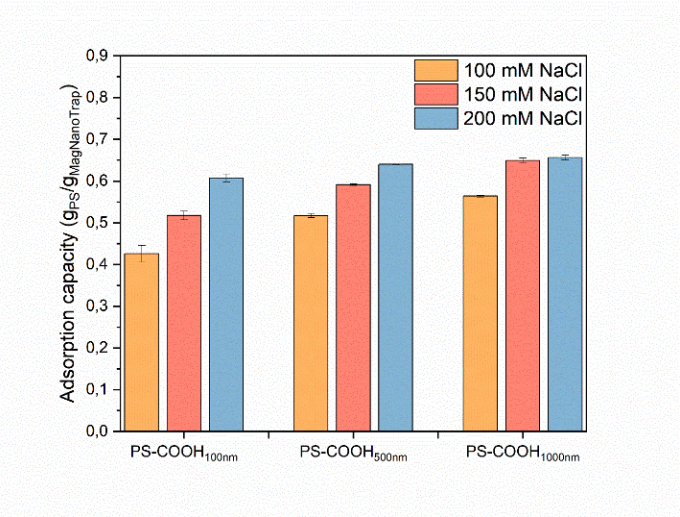


**Figure 31. Adsorption capacity of PS-COOH NPs with different sizes at different NaCl concentrations.** Smaller NPs with a larger surface area require more NaCl to neutralize the surface charges.

Enrichment experiments were conducted using 50 mM of various monovalent cations over a 30-second reaction period to further test the salt effect hypothesis. The resulting adsorption capacities of MagNanoTrap against PS-COOH$_{500\ nm}$ NPs followed the order $NH_4^+ > K^+ > Rb^+ > Cs^+ > Na^+ > Li^+$, aligning with the Hofmeister series and reflecting the cations' salting-out effects (Figure 32).[190]

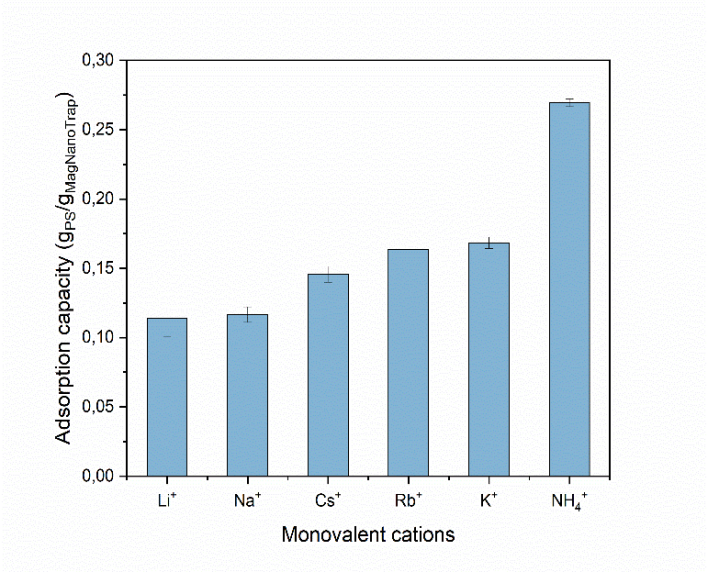


**Figure 32. Adsorption capacity of PS-COOH$_{500\ nm}$ NPs by MagNanoTrap enrichment platform in the presence of 50 mM monovalent cations.** The enrichment reactions were performed with a 30-second shaking, and follow the Hofmeister series.

Enrichment experiments were also conducted using heavy metal ions, such as $Cd^{2+}$, $Zn^{2+}$, $Cu^{2+}$, and $Ni^{2+}$, in place of NaCl, to evaluate the applicability of the MagNanoTrap enrichment platform in environmental water, especially from wastewater sources, containing heavy metal

ions that can be adsorbed on NPs' surfaces.[191] The results showed that PS-COOH$_{500\ nm}$ NPs were recovered with over 99% efficiency, indicating that the presence of these heavy metal ions can also drive the enrichment process (Figure 33).

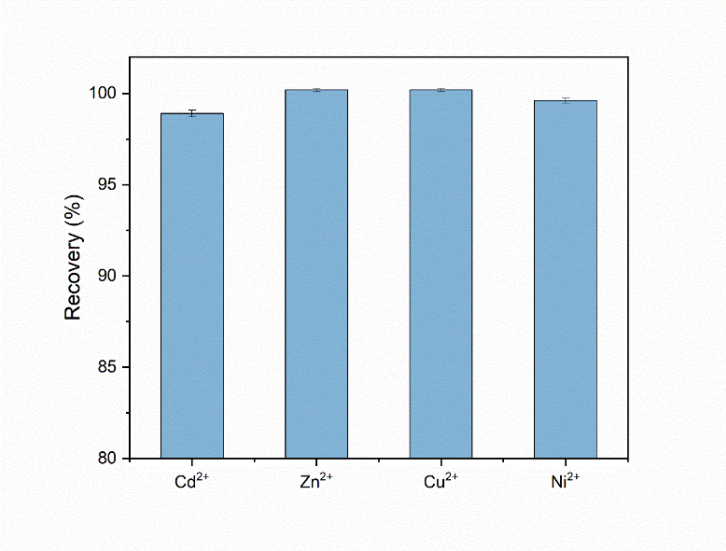


**Figure 33. Recovery of PS-COOH $_{500nm}$ NPs with the addition of heavy metal ions.** Heavy metal ions used for the enrichment assay are $Cd^{2+}$, $Zn^{2+}$, $Cu^{2+}$, and $Ni^{2+}$. Heavy metals don't influence the interaction between the functionalized beads and NPs.

Taking $Mg^{2+}$ ions as an example, the heavy metal ions may play a role as a bridging reagent between MagNanoTrap beads and PS-COOH NPs through Lewis acid-base interactions (Figure 34). The peptide-decorated iron oxide surface contains abundant -$NH_2$ and -COOH groups, both of which function as Lewis bases. Similarly, the PS NPs are carboxylated. $Mg^{2+}$, a well-known Lewis acid, can coordinate with these Lewis base groups on both surfaces, forming a strong coordinate covalent bond.[192]

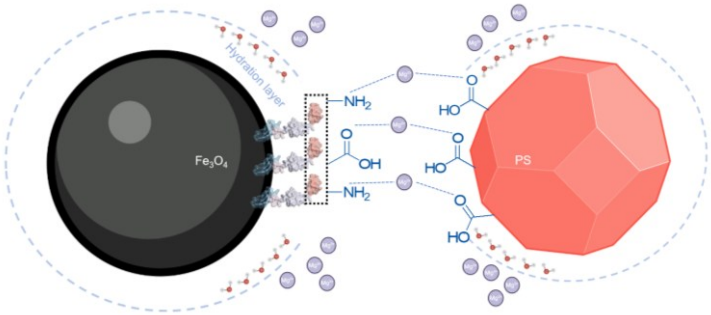


**Figure 34. Scheme illustrating the Mg2+ effects on NPs adsorption by MagNanoTrap beads.**

The role of Lewis acid-base interactions in adsorption was further confirmed by testing metal ions with varying Lewis acid strengths, including $Na^{+}$, $Mg^{2+}$, and $Al^{3+}$, which follow the order $Al^{3+} > Mg^{2+} > Na^{+}$ (Figure 35). In a 30-second adsorption assay, increasing salt concentrations enhanced adsorption capacity. Notably, the weakest Lewis acid, $Na^{+}$, required a high

concentration of 800 mM to achieve maximum adsorption. In contrast, the strongest Lewis acid, $Al^{3+}$, reached equilibrium at just 2 mM. $Mg^{2+}$, with intermediate strength, achieved saturation at 25 mM. These results clearly demonstrate that adsorption capacity under fixed reaction time correlates with the Lewis acid strength of the metal ions, supporting the proposed mechanism of Lewis acid-base interaction-driven enrichment.

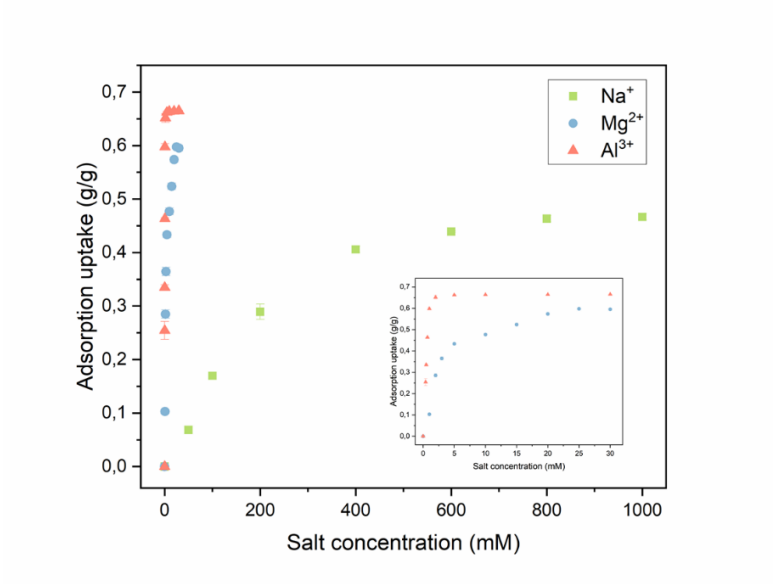


**Figure 35. Adsorption uptake of PS-COOH$_{500\ nm}$ NPs by MagNanoTrap in the presence of $Na^+$ (square), $Mg^{2+}$ (circle), and $Al^{3+}$ (triangle) ions.** The inner figure is the zoomed-in view showing the details for $Mg^{2+}$ and $Al^{3+}$ induced adsorption. The adsorption is facilitated by Lewis acid-base interaction.

Using $Mg^{2+}$ as a representative ion, adsorption behavior was further explored through kinetic and isotherm studies (Figure 36). The kinetic data fit best with a pseudo-second-order model, reaching saturation within 2 minutes, faster and more efficient than $Na^+$-driven adsorption, and requiring less salt. Interestingly, the adsorption isotherm exhibited two distinct phases. The initial phase followed the Freundlich model, indicating multilayer adsorption, with a maximum adsorption capacity of approximately 25 g/g, significantly higher than the ~3.8 g/g observed with $Na^+$. This enhanced performance is attributed to coordination bonds formed through Lewis acid-base interactions, which are stronger than hydrophobic interactions. In the first layer, $Mg^{2+}$ acts as a Lewis acid, bridging the electron-donating groups (–$NH_2$ and –COOH) on the peptide-functionalized iron oxide beads and the carboxylated PS NPs. Subsequent layers are formed by $Mg^{2+}$ bridging between PS-COOH NPs. However, once a critical size or complexity is reached, the structure becomes unstable, and the adsorption capacity declines due to loss of structural integrity.

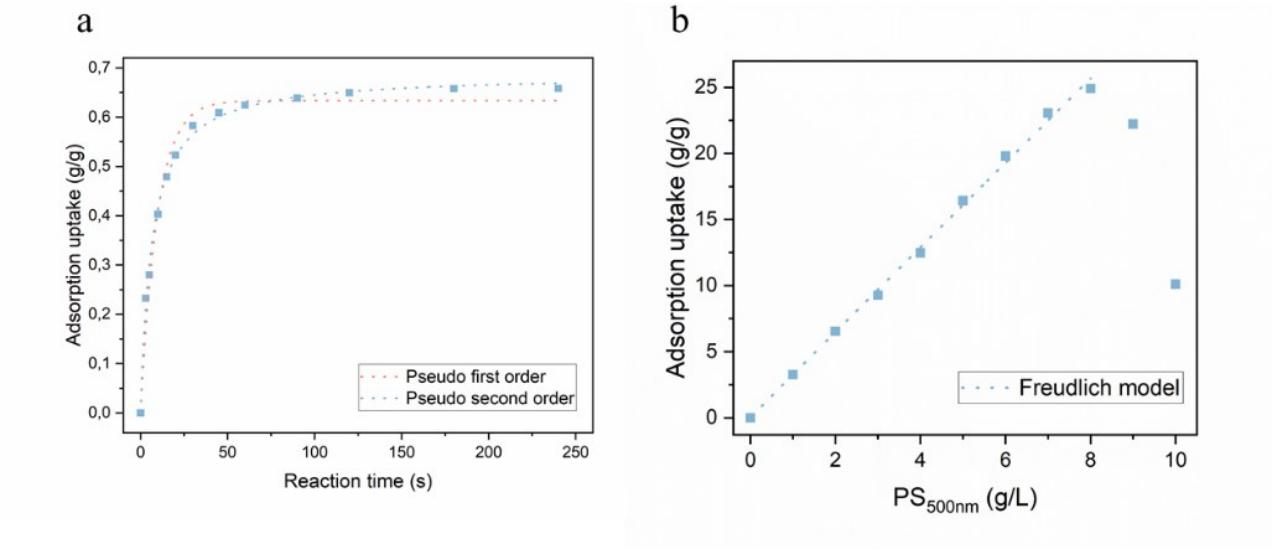


**Figure 36. Adsorption kinetics (a) and isotherms (b) of the MagNanoTrap platform for PS-COOH$_{500\ nm}$ NPs adsorption in the presence of 25 mM $Mg^{2+}$.** The kinetics are fitted to both Pseudo-first-order and Pseudo-second-order, and the isotherm is fitted with the Freudlich model. The adsorption process is faster when the adsorption is initialized by $Mg^{2+}$ compared with that by $Na^{+}$.

Using $Zn^{2+}$ as a model ion, the adsorption uptake of MagNanoTrap beads and PS-COOH$_{500\ nm}$ NPs was assessed individually and in combination for heavy metal uptake (Figure 37). At a $Zn^{2+}$ concentration of 20 mM, MagNanoTrap beads (0.3 g/L) alone adsorbed 1292.3 ± 55.5 µM of $Zn^{2+}$, while PS-COOH 500 nm NPs (0.2 g/L) independently captured 538.5 ± 40.7 µM. However, when both components were incubated together, the total $Zn^{2+}$ adsorption reached only 1456.4 ± 38.7 µM, less than the sum of their individual capacities. This reduction further suggests that $Zn^{2+}$ ions likely act as bridging agents between the MagNanoTrap beads and the PS-COOH NPs during the adsorption process.

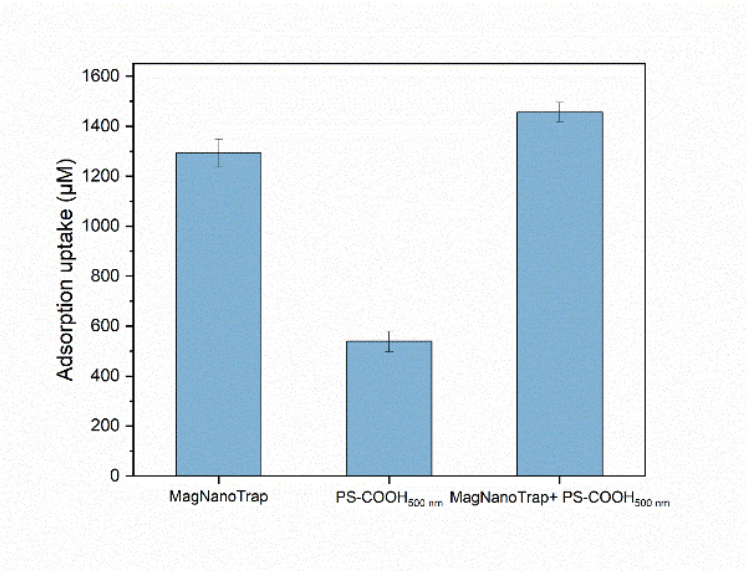


**Figure 37. Adsorption uptake of $Zn^{2+}$ by MagNanoTrap and PS-COOH$_{500\ nm}$, both individually and in combination.** Zn2+ plays the role of a bridging reagent between the MagNanoTrap and PS NPs.

The results above demonstrate that NaCl supplementation enhances MBP1 binding to plastic surfaces, while the presence of heavy metals does not interfere with the enrichment process. This underscores the broad applicability of the MagNanoTrap platform, which can be effectively used across various natural aqueous environments, including lakes, rivers, seawater, and wastewater, since NaCl can be readily introduced to facilitate the enrichment when needed.

### 3.1.6 Evaluation of NPs enrichment performance by MagNanoTrap system in a 1 L-scale reaction

This section aims to demonstrate that the NaCl-assisted enrichment protocol is scalable to a 1-liter volume by evaluating the recovery of spiked mixed polymer nanoparticles, including PP, PE, PET, and PS, in deionized water. As illustrated in Figure 38, a seven-step workflow was developed to assess the enrichment performance of the MagNanoTrap technology at this scale, utilizing Py-GC/MS for detection and quantification of the plastic nanoparticles.

In the first step, the water samples were subjected to 1 µm glass-fiber filtration to remove the large aggregates, followed by hydrogen peroxide ($H_2O_2$) digestion at 60 °C with shaking for two days to eliminate organic matter. In the second step, MagNanoTrap beads were introduced into the pretreated samples along with NaCl to promote binding. Steps three and four involved magnetic extraction of the MagNanoTrap-NPs complexes, effectively reducing the sample volume. In step five, the complexes were digested with 37% hydrochloric acid at 65 °C, followed by filtration using 10 kDa centrifugal filters (PES membrane) to remove the acid and keep the enriched NPs. The sixth step involved recovering the complexes with methanol and transferring them to Py-GC/MS sampling cups. Finally, in step seven, the NPs were analyzed and quantified using Py-GC/MS analysis.

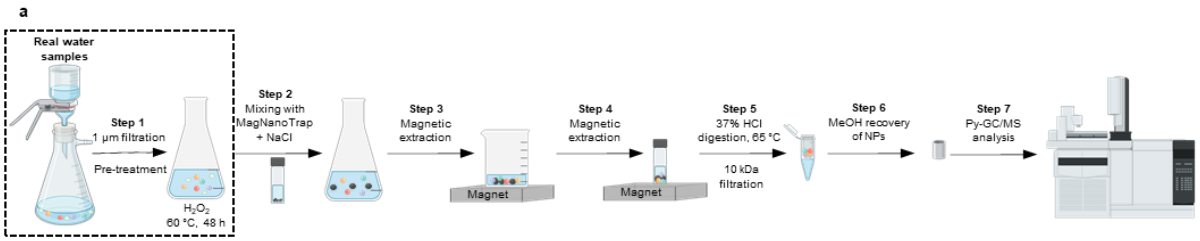


**Figure 38. Scheme of the seven-step workflow developed for assessing the enrichment performance of MagNanoTrap technology on 1 1 L scale.** In step 1, 1 µm filtration and H2O2 digestion were done to remove the large aggregates and organic matter; in step 2, MagNanoTrap beads were added to the pretreated environmental water samples with the supplementation of NaCl; in steps 3 and 4, MagNanoTrap-NPs complex was extracted by a magnet to reduce the volume; in step 5, MagNanoTrap-NPs complex was digested by 37% HCl at 65 °C, followed by filtration with 10 kDa centrifugal filters; in step 6, the complex was recovered with methanol and transferred to Py-GC/MS sampling cups; and in step 7, NP quantification was done by Py-GC/MS.

Before performing the 1-liter scale enrichment, specific indicator ions for the nine target NPs were selected based on prior identifications and literature sources.[18, 19, 69, 73, 193] Analytical standards for each plastic type were examined using Py-GC/MS to determine their characteristic pyrolysis products and corresponding ions (Table 5, Figure 39). Additionally, potential interferences from peptide-related signals were evaluated to ensure specificity.

The pyrolysis markers selected for each polymer are summarized in Table 5. For PMMA, methyl methacrylate (m/z 100) was chosen as the quantifier due to its high specificity and sensitivity. In the case of PP, 2,4-dimethyl-1-heptene (m/z 126) was identified as the most suitable marker. Regarding PC, isopropenylphenol (m/z 134) was used as the qualifying indicator compound due to its specificity. For Nylon 6, although ε-caprolactam (m/z 113) is widely recognized as a highly specific marker, it also overlapped with signals from the peptide matrix. Therefore, N-(5-cyanopentyl)hex-5-enamide (m/z 154) was chosen instead for Nylon 6 qualification to reduce interference. For Nylon 66, the primary pyrolysis product, cyclopentanone (m/z 84), was selected as the main quantifier. However, because this compound is also generated from the pyrolysis of other nylon types (e.g., Nylon 4,6, Nylon 12,6, Nylon MXD6, and various nylon copolymers such as Nylon 6/66),[194] it was used to represent the total contribution from all cyclopentanone-based nylons. This broader classification is denoted in this study as ∑Nylon 66.

PS pyrolysis yields three major products: styrene monomer (m/z 104), its dimer (3-butene-1,3-diyldibenzene; m/z 91 and 208), and trimer (5-hexene-1,3,5-triyltribenzene; m/z 91 and 312). While the styrene monomer is the most abundant and commonly used in clean samples, it is also known to arise from natural organic matter such as chitin, lignin, albumin, and fish proteins, compromising its specificity in environmental matrices.[44, 113, 116, 195, 196] Therefore, for environmental analysis, the dimer and trimer, whose formation is unique to polystyrene, offer greater reliability. Among these, the styrene trimer, though less abundant, was selected as the quantification marker due to its specificity and the strong molecular ion signal at m/z 91.[18, 44, 116, 195, 196]

For PET analysis, vinyl benzoate (m/z 105) is commonly used as the quantifier ion, with benzoic acid (m/z 122) serving as the qualifier. However, during this study, it was found that peptides exhibited overlapping signals at these same m/z values, compromising the specificity of PET detection. To avoid this interference, monomethyl terephthalate (also m/z 105), a more distinct pyrolysis product for PET, was selected as the quantifier instead.[193]

PE pyrolysis yields a variety of long-chain hydrocarbons, including alkanes, alkenes, and alkadienes. While these compounds can be used for quantification, they are also commonly produced from other hydrocarbon-containing substances such as lipids, oils, waxes, surfactants, and natural fats, introducing substantial matrix interference, particularly in complex environmental samples.[195-199] Among these, n-alkadienes, though less intense in signal, have been shown to be the most specific indicators for PE, especially in avoiding interference from biogenic materials. Thus, in this study, n-alkadiene C17 (m/z 125) was selected for PE quantification, ensuring minimal interference from the peptide background.

For PVC, 1-methylnaphthalene and 2-methylnaphthalene (both m/z 142) were selected for quantification, despite their relatively low specificity. Naphthalene (m/z 128) was chosen as the qualifier due to its strong signal intensity and sensitivity, which were superior to other potential markers. However, interference from the peptide background rendered PVC detection unreliable within the MagNanoTrap system. As a result, data for PVC were excluded from further analysis and discussion in this study.

The selected indicator ions for all analyzed plastics showed strong linearity in their calibration curves in the range of 0.5 – 2.5 mg $SiO_2$ complex/cup, with correlation coefficients around 0.99, confirming the reliability of the quantification approach. The LODs, calculated based on concentrations obtained from laboratory and procedural blanks, were 0.059 µg/L for PE, 0.201 µg/L for PP, 0.061 µg/L for PS, 0.043 µg/L for PET, 0.001 µg/L for PMMA, 0.001 µg/L for PC, 0.013 µg/L for Nylon 6, and 0.145 µg/L for Nylon 66. These low LODs enable reliable quantification of nanoplastic particle mass concentrations in water samples using the proposed method. Notably, the LOD values obtained are consistent with those reported in previous studies on NPs in environmental water samples.[18, 19, 69, 73]

**Table 5 Characteristic components and calibration functions of the eight analyzed nanoplastic polymer types.**

| Polymer | Indicator compound | Indicator ions (m/z) | Calibration functions | Linearity ($R^2$) | LOD (ng) | LOQ (ng) |
|---|---|---|---|---|---|---|
| PE | 1-Heptadecene (C17) | 125 | y=9639.058x+17634.639 | 0.994 | 58.62 | 177.64 |
| PP | 2,4,6-Dimethyl-1-heptene | 126 | y=19794.827x+5293.108 | 0.996 | 200.50 | 607.57 |
| PS | Styrene trimer | 91 | y=3620170.055x+91565.638 | 0.999 | 60.67 | 183.84 |
| PET | Monomethyl terephthalate | 105 | y=624495.860x-6139.633 | 0.996 | 42.76 | 129.60 |
| PMMA | Methyl methacrylate | 100 | y=2774172.354x-865.402 | 0.999 | 1.30 | 3.95 |
| PC | p-Isopropenylphenol | 134 | y=3438297.015x+23987.357 | 0.987 | 0.81 | 2.45 |
| Nylon 6 | *N*-(5-cyanopentyl)hex-5-enamide | 154 | y=2690993.850x+133328.500 | 0.990 | 13.12 | 39.76 |
| Nylon 66 | Cyclopentanone | 84 | y=697560.697x+168218.346 | 0.990 | 145.26 | 440.18 |

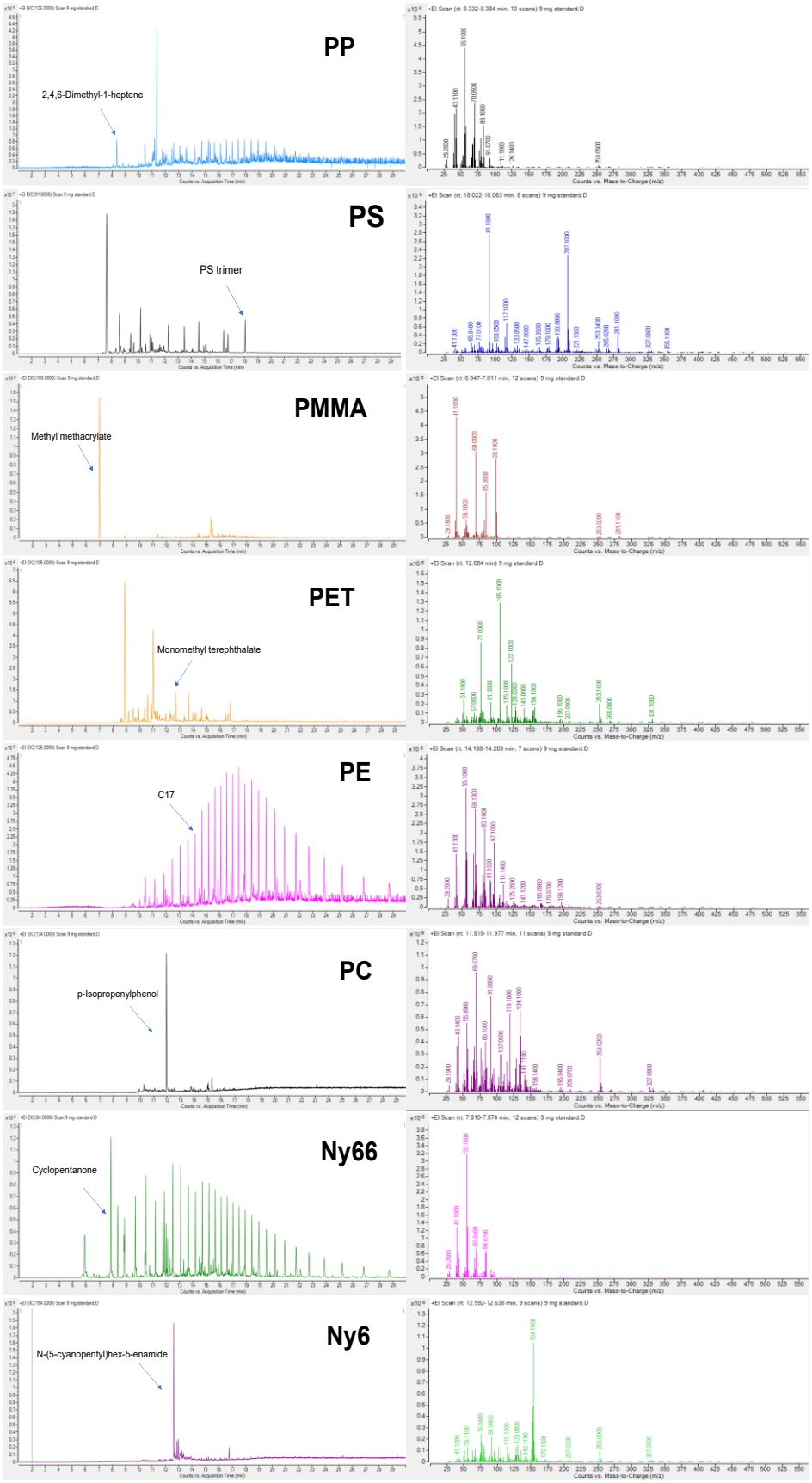


**Figure 39. GC/MS spectrum chromatography of each plastic type, including PP, PS, PMMA, PET, PE, PC, Ny6, and Ny66.** Unfortunately, the figure could not be increased in size. In detail, the results show the retention time and specific compound for each polymer, together with the corresponding mass spectroscopy.

Since the enriched NPs mixed with peptides were combined for subsequent Py-GC/MS analysis, it is crucial to verify that the selected indicator compounds produce signals specific to plastics and not to the peptides to ensure reliable quantification. As shown in Figure 40, all plastic types analyzed using the MagNanoTrap enrichment technology exhibited signals exclusively from the plastics, confirming that peptides do not interfere with the identification of PE, PET, PP, PS, PMMA, PC, Ny6, and Ny66 NPs.

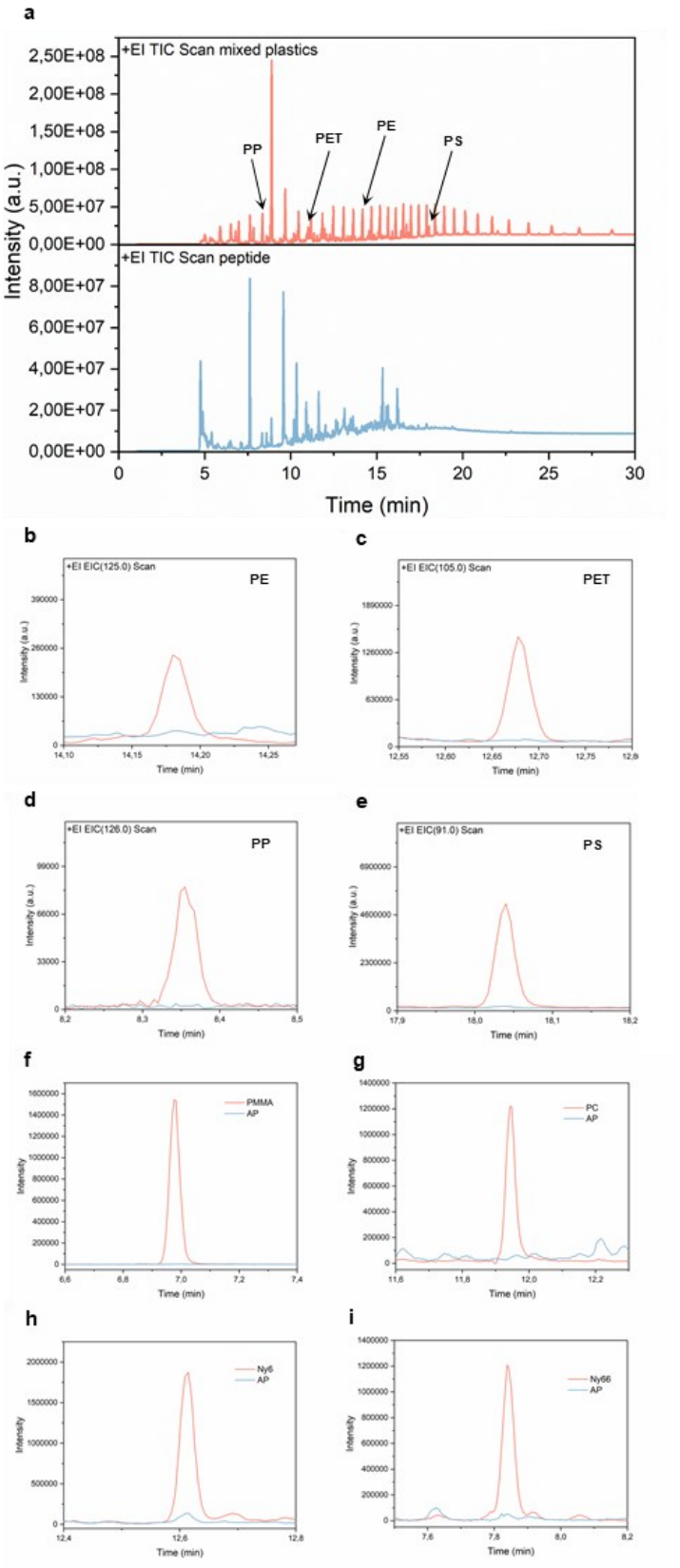


**Figure 40. Py-GC/MS chromatograms from plastics and peptides. a,** Chromatograms of mixed plastics, containing PP, PE, PET, PS, PMMA, PC, PVC, Nylon 6, Nylon 66, ABS, and SBR (top) and the peptide LCI-DZ-MBP1 (bottom). Chromatograms with the extraction of indicator compounds for each plastic type, including **b,** PE, **c,** PET, **d,** PP, **e,** PS, **f,** PMMA, **g,** PC, **h,** nylon 6, and **i,** nylon 66, compared with the peptide. It shows that the peptide doesn't influence the plastic analysis.

The potential interference from iron oxide in nanoparticle quantification was further examined using PS as a model. PS NPs captured by MagNanoTrap beads were analyzed both with and without HCl acid digestion. As shown in Figure 41, without the digestion of the iron oxide, the characteristic peak (m/z 91) corresponding to the PS trimer appeared split into two peaks, accompanied by a significant reduction in signal intensity. This highlights the critical need to remove iron oxide prior to plastics analysis by Py-GC/MS.

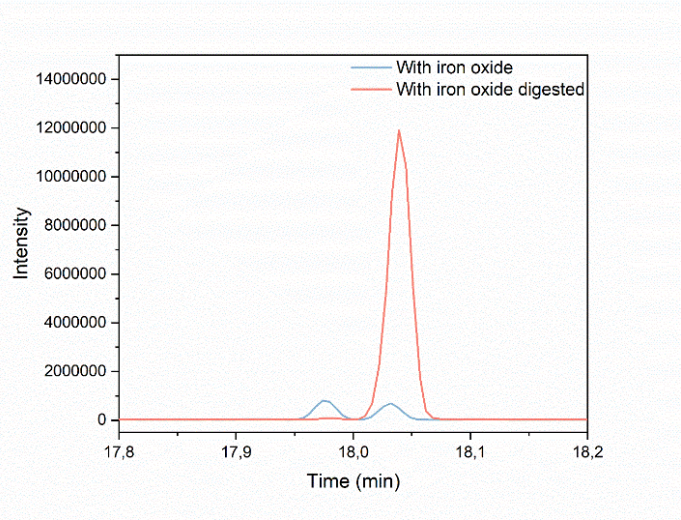


**Figure 41. Py-GC/MS chromatography of 5 µg PS NPs captured by the MagNanoTrap beads with and without acid digestion.** The presence of iron will interfere with the quantification of plastics.

The reliable quantification based on the MagNanoTrap enrichment platform was established by eliminating peptide background and iron oxide interference. The subsequent parameter optimization focused on determining the optimal amount of MagNanoTrap beads, the required incubation time for efficient PS-COOH NPs recovery, and the ideal NaCl concentration to assess the 1 L-scale enrichment capability of the MagNanoTrap platform for trace amounts of PS-COOH $_{500nm}$ NPs. In detail, when spiking 5 µg of PS-COOH $_{500nm}$ NPs, increasing the quantity of MagNanoTrap beads enhanced recovery, with 16 mg of beads achieving a recovery rate of 64.3% (Figure 42a). The relationships between PS NPs recovery and both incubation time and NaCl concentration were non-linear, with the highest recoveries observed at 2 hours of shaking and 1 M NaCl, respectively (Figure 42b and 42c). The broad applicability of the method was further demonstrated by enriching a mixed nanoparticle suspension containing 1 µg each of PP, PE, PET, and PS, resulting in recoveries of 65.8%, 68.0%, 67.7%, and 58.7%, respectively (Figure 42d).

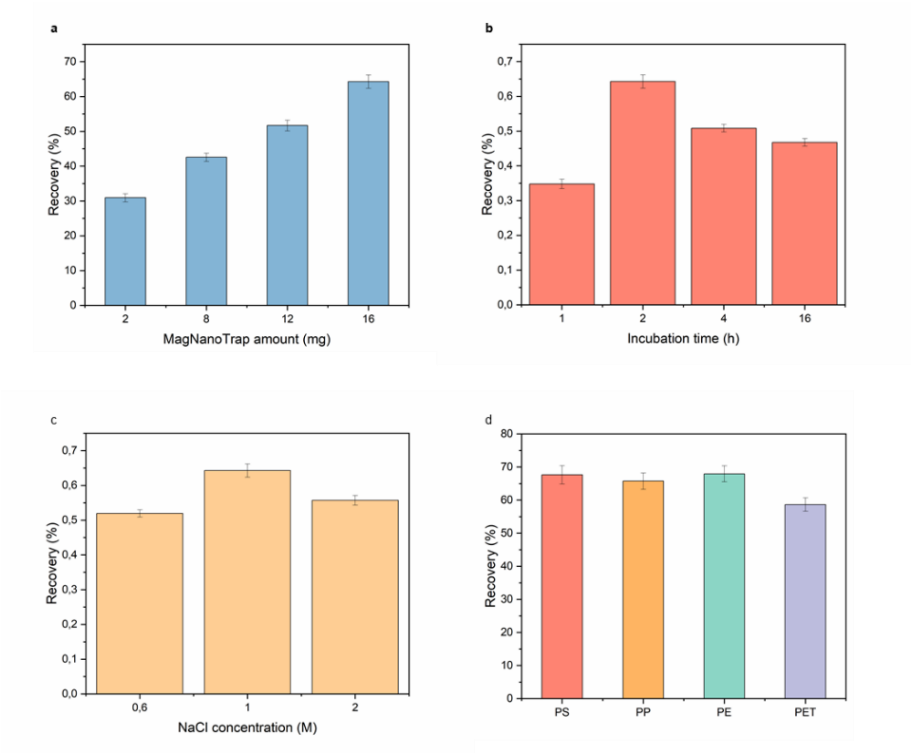


**Figure 42. One-liter scale enrichment characterized by Py-GC/MS. a,** Recovery of PS-COOH 500nm NPs (5 µg spiked in 1 L deionized water) at different amounts of MagNanoTrap beads, with 1 M NaCl and 2 h shaking. **b,** Recovery of PS-COOH 500nm NPs (5 µg spiked in 1 L deionized water) at different shaking times, with 1 M NaCl and 16 mg MagNanoTrap beads. **c,** Recovery of PS-COOH 500nm NPs (5 µg spiked in 1 L deionized water) at different NaCl concentrations, with 2 h shaking time and 16 mg MagNanoTrap beads. **d,** Recovery of mixed NPs (PS, PP, PE, and PET, each spiked with 1 µg in 1 L deionized water) by 16 mg MagNanoTrap beads.

Overall, the results shown above demonstrate the scalability of the MagNanoTrap platform with enrichment of trace amounts of mixed NPs, down to 1 µg/L, spiked in 1 L of water. It makes the MagNanoTrap enrichment technology an attractive tool for NPs detection and quantification in environmental water samples.

### 3.1.7 NPs detection and quantification in environmental water samples

The applicability of the MagNanoTrap enrichment technology for monitoring nanoplastic contamination in environmental water samples was evaluated using seven distinct waters. These sources included freshwater from the Rhine River (Düsseldorf, Germany, Figure 43), seawater from the coast (Portugal), lake water from Hangeweiher Park (Aachen, Germany, a site with high human activity), lake water from the Eifel natural reservoir (Schleiden, Germany, a site with low human activity), and wastewater from the effluent of the wastewater treatment plant (WWTP, Heiderscheidergrund, Luxembourg). Additional wastewater samples were collected after sand filtration and ultrafiltration to assess the impact of advanced treatment processes. This diverse selection of samples, spanning freshwater, saltwater, and treated wastewater, allowed for a comprehensive assessment of the MagNanoTrap technology's

versatility. Prior to analysis, all samples were pretreated with $H_2O_2$ to remove organic matter from the NP surfaces, thereby facilitating effective MBP1 binding and enabling accurate quantification via Py-GC/MS analysis based on pyrolysis products, characteristic ions, and their corresponding intensities (Figure 40).[19, 69]


**Figure 43. Representative sampling site of the river sample in the Rhine River, Düsseldorf, Germany.** A sample of 1 L of river water was collected for later NPs detection and quantification.

NPs of varying sizes and polymer compositions are anticipated to be present in environmental water;[18, 73] however, commercially available analytical standards for many nanoplastic types are still lacking.[18, 44, 72, 73, 77, 113, 116, 200, 201] To address this, a combination of commercially sourced 500 nm PS NPs and lab-synthesized nanoparticles of PP, PE, and PET, with average sizes of 340 nm (PP and PE) and 115 nm (PET), was used in this study. These particles were selected as the closest practical surrogates for the targeted NPs to assess their recovery efficiency. Although these model standards serve as useful proxies, it's important to note that even polymer-matched NPs might not fully reflect the diversity of NPs found in the environment. This is primarily due to the limited information available on environmental plastics smaller than 10 µm, including their shapes, size distributions, surface properties, and tendency to aggregate. Hence, while recovery testing provides valuable insight, comprehensive characterization of environmental NPs remains a critical step in further understanding this pollutant class.

In this study, quantitative recovery of each nanoplastic type (PP, PE, PET, and PS) was achieved at a spiking level of 1 µg/L across seven environmental water matrices, which included river, lake, seawater, and treated wastewater samples (Table 6). The observed recovery rates in these environmental samples ranged from 51.9% to 60.6%, whereas those in deionized water ranged between 58.7% and 68.0%. Although these recoveries fell below 70%,

they are consistent with values reported in similar studies. For example, prior work using large-volume ultrafiltration combined with $H_2O_2$ digestion and Py-GC/MS analysis reported PS NPs recoveries between 58.3%–60.1% in Milli-Q water and 54.6%–58.1% in wastewater. Similarly, PMMA NPs recoveries were reported in the range of 65.4%–68.1% for Milli-Q water and 57.8%–64.2% for wastewater.[19, 69]

**Table 6. Determination of the concentration and spiked recovery of NPs in environmental waters by the proposed method.** For each type of environmental water sample, 1 µg of PP, PE, PS, and PET NPs were spiked into 1 L of water samples to study the recovery.

| | PP | | PE | | PS | | PET | | PMMA | Ny66 | N6 | PC | SUM |
|---|---|---|---|---|---|---|---|---|---|---|---|---|---|
| Sample | Detected (µg/L) | Recovery (%) | Detected (µg/L) | Recovery (%) | Detected (µg/L) | Recovery (%) | Detected (µg/L) | Recovery (%) | Detected (µg/L) | Detected (µg/L) | Detected (µg/L) | Detected (µg/L) | Detected (µg/L) |
| River | 1,089 | | 2,609 | | 0,148 | | 0,239 | | 0,035 | 1,416 | 0,090 | 0,008 | 5,636 |
| Spiked | 1,630 | 54,09 | 3,198 | 58,82 | 0,725 | 57,68 | 0,762 | 52,21 | | | | | |
| Lake in the park | 1,410 | | 3,684 | | 1,863 | | 0,103 | | 0,033 | 1,415 | 0,078 | 0,012 | 8,598 |
| Spiked | 1,969 | 55,86 | 4,270 | 58,60 | 2,441 | 57,88 | 0,623 | 51,99 | | | | | |
| Lake in the natural reservoir | 0,259 | | 1,402 | | 0,211 | | ND | | 0,019 | 0,641 | 0,072 | 0,001 | 2,605 |
| Spiked | 0,839 | 57,99 | 2,003 | 60,09 | 0,810 | 59,88 | 0,555 | 55,48 | | | | | |
| Sea | 0,433 | | 1,220 | | 0,061 | | ND | | 0,013 | 1,412 | 0,018 | 0,005 | 3,160 |
| Spiked | 1,039 | 60,61 | 1,783 | 56,33 | 0,603 | 54,21 | 0,543 | 54,35 | | | | | |
| Wastewater | 4,046 | | 4,265 | | 1,746 | | 0,624 | | 0,062 | 2,267 | 0,084 | 0,069 | 13,161 |
| Spiked | 4,620 | 57,43 | 4,840 | 57,51 | 2,327 | 58,02 | 1,149 | 52,50 | | | | | |
| Wastewater after sand filtration | 2,176 | | 1,340 | | 0,893 | | 0,367 | | 0,034 | 1,318 | 0,077 | 0,021 | 6,226 |
| Spiked | 2,762 | 58,60 | 1,901 | 56,09 | 1,470 | 57,72 | 0,886 | 51,92 | | | | | |
| Wastewater after ultrafiltration | 0,388 | | 0,062 | | 0,272 | | 0,069 | | 0,022 | 0,468 | 0,052 | 0,018 | 1,350 |
| Spiked | 0,955 | 56,75 | 0,647 | 58,47 | 0,832 | 56,00 | 0,593 | 52,42 | | | | | |

It is important to acknowledge that this study did not examine the effects of natural aging or weathering on the selected NPs. However, previous research has demonstrated that extensive environmental weathering of plastic particles can alter the signal intensity of pyrolysis-derived indicator compounds used for quantification via Py-GC/MS, often resulting in decreased or variable responses depending on UV exposure duration.[202, 203] Based on these findings, we propose that quantifying NPs in water samples that have undergone prolonged weathering, such as exposure to sunlight, oxidation, or microbial activity, may be affected when using calibration standards made from unweathered, virgin polymers. This is particularly relevant because such changes could compromise the accuracy of quantification if the aged materials respond differently during pyrolysis. As previously discussed, the lack of comprehensive surface and chemical characterization data for environmental NPs adds a layer of uncertainty to these analyses. This limitation stems from our incomplete understanding of the physical and chemical transformations that environmental NPs undergo over time. To reduce this uncertainty and improve the reliability of quantitative assessments, further studies are needed to investigate how environmental aging alters nanoplastic properties and their resulting pyrolysis profiles.

Overall, the aforementioned findings highlight the robustness of our method, particularly given the absence of standardized, validated approaches capable of quantifying a broad spectrum of NPs across diverse environmental matrices.[18, 19, 69, 73, 113, 204] That said, it's essential to acknowledge that several procedural steps during sample preparation, such as microfiltration, $H_2O_2$ digestion, transfers between glass containers, HCl treatment, and cup loading for Py-GC/MS, may introduce particle loss. These losses likely arise from NPs adhering to container surfaces, membranes, or pipette tips during handling. Furthermore, particles that aggregated with each other or bound to larger particulates may have been excluded during filtration with a 1 μm pore-size membrane, contributing to the underestimation of actual concentrations.

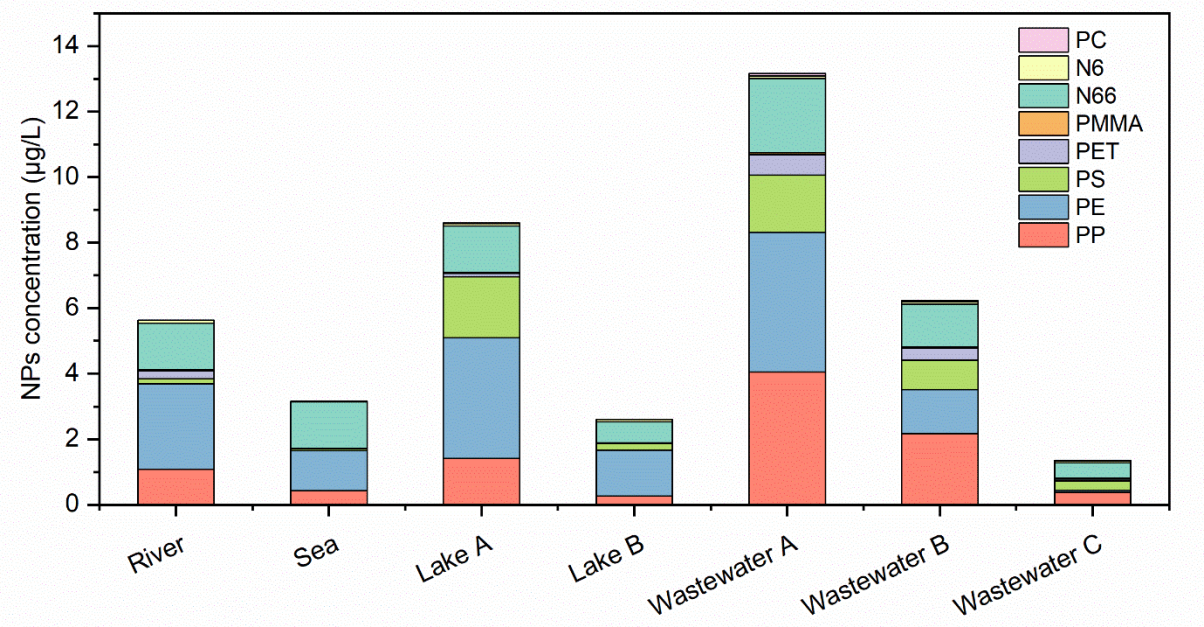


**Figure 44. Quantification and determination of plastic composition in seven types of environmental water samples.** It includes river water from the Rhine River, seawater from the coast of Portugal, lake water from the Hangeweiher Park (Lake A) with high human activity, lake water from the Eifel natural reservoir (Lake B) with restricted human activity, wastewater samples obtained from the effluent of the wastewater treatment plant Heiderscheidergrund (Wastewater A), wastewater after sand filtration (Wastewater B) and wastewater after ultrafiltration (Wastewater C).

The effectiveness of the hyphenated analytical method was validated by examining environmental water samples collected from diverse locations across Portugal, Luxembourg, and Germany. NP concentrations were quantified using calibration curves derived from the peak areas of specific indicator ions. In the absence of peptide-related peak interference, eight different types of plastic particles, including PP, PE, PS, PET, PMMA, Nylon 6, Nylon 66, and PC, were accurately identified and quantified. The results, summarized in Table 6, reveal the measured NP mass concentrations in each sample.

The total concentrations of NPs found in river water, seawater, lake water from a park, lake water from a natural reservoir, untreated wastewater effluent, wastewater after sand filtration, and wastewater after ultrafiltration were 5.64 µg/L, 3.16 µg/L, 8.60 µg/L, 2.61 µg/L, 13.16 µg/L, 6.23 µg/L, and 1.35 µg/L, respectively (Fiugre 44). Among the detected polymers, PE, PP, and Nylon 66 were present in relatively higher concentrations, ranging from 1.220 to 4.265 µg/L, 0.259 to 4.046 µg/L, and 0.641 to 2.267 µg/L, respectively. These were followed by PS (0.061–1.746 µg/L), PET (below detection limit to 0.624 µg/L), Nylon 6 (0.018–0.084 µg/L), PC (0.001–0.069 µg/L), and PMMA (0.013–0.062 µg/L). Our quantified results for wastewater are relatively high compared to the values reported in the literature. For instance, Py-GC/MS analysis of NPs in treated effluent from a WWTP in Australia reported concentrations ranging from 0.8 to 12.4 µg/L.[73] These variations may reflect differences in the pollution levels and

treatment technologies employed at the WWTPs, as well as discrepancies in the quantification methods used.

Notably, lake water from an urban park, where human activity is more prominent, contained approximately 3.3 times more NPs than water from a natural reservoir. This highlights the significant contribution of anthropogenic activities to environmental plastic pollution. In terms of wastewater treatment performance, notable reductions in NPs concentrations were observed. Sand filtration removed approximately 52.7% of NPs, while ultrafiltration achieved a higher removal efficiency of up to 89.7%.

With the exception of PET, which was not detected in seawater or the natural reservoir lake, all other target nanoplastic types were identified and quantified in the environmental samples, confirming their widespread presence in natural water systems. Among these, PP, PE, and Nylon 66 emerged as the most dominant NPs, collectively accounting for more than 75% of the total detected plastic content (Figure 45). Notably, PP and PE consistently appear as the most abundant plastic types in prior studies, regardless of whether the samples originated from surface waters or wastewater sources.[18, 19, 69, 73] Interestingly, while Nylon 66 was not commonly analyzed or reported as a major nanoplastic in earlier studies, it ranked among the top three most prevalent polymers detected in this investigation. This discrepancy may stem from differences in sampling strategies, analytical techniques, local sources of plastic pollution, or variations in wastewater treatment processes. The prominent presence of Nylon 66 in river, lake, sea, and wastewater samples suggests it is a significant contributor to environmental nanoplastic pollution and underscores the need to include it in future monitoring and analytical frameworks for NPs in aquatic environments.

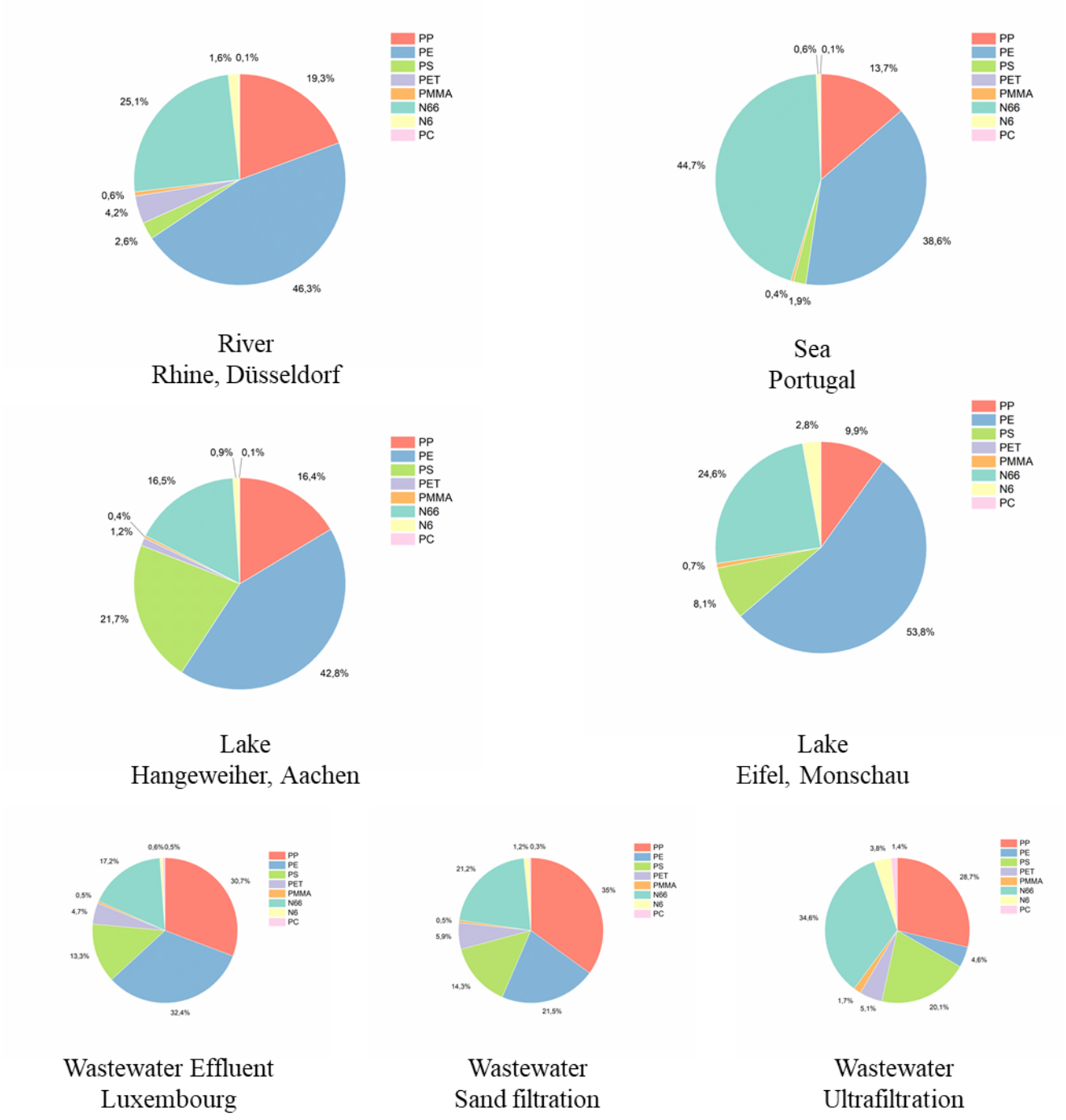


**Figure 45. Plastic distribution in detected environmental water samples.** PP, PE, and Nylon 66 are the top three dominant plastic types in environmental water.

While the morphological characterization of nanoplastic particles is important for understanding their environmental behavior and toxicological impact, direct visualization in non-concentrated water samples remains highly challenging. However, following enrichment using the developed MagNanoTrap platform, SEM analysis enabled the observation of various NP shapes, including fiber-like, flake-like, and ball-stick morphologies, which is consistent

with observations reported in previous studies (Figure 46).[66] The fiber-like forms of NPs were particularly prominent in samples from ultrafiltrated wastewater and were predominantly below 100 nm in size. Since treated wastewater is often released back into domestic water systems, the presence of such small-sized NPs raises concern. Due to their high surface-to-volume ratio, these particles have a heightened ability to adsorb toxic substances.[27] Once ingested by animals or humans, they can carry these harmful compounds into the body.[205] This risk is especially pronounced for NPs smaller than 20 nm, as they have the potential to cross the blood-brain barrier, possibly leading to serious health effects.[37, 38]

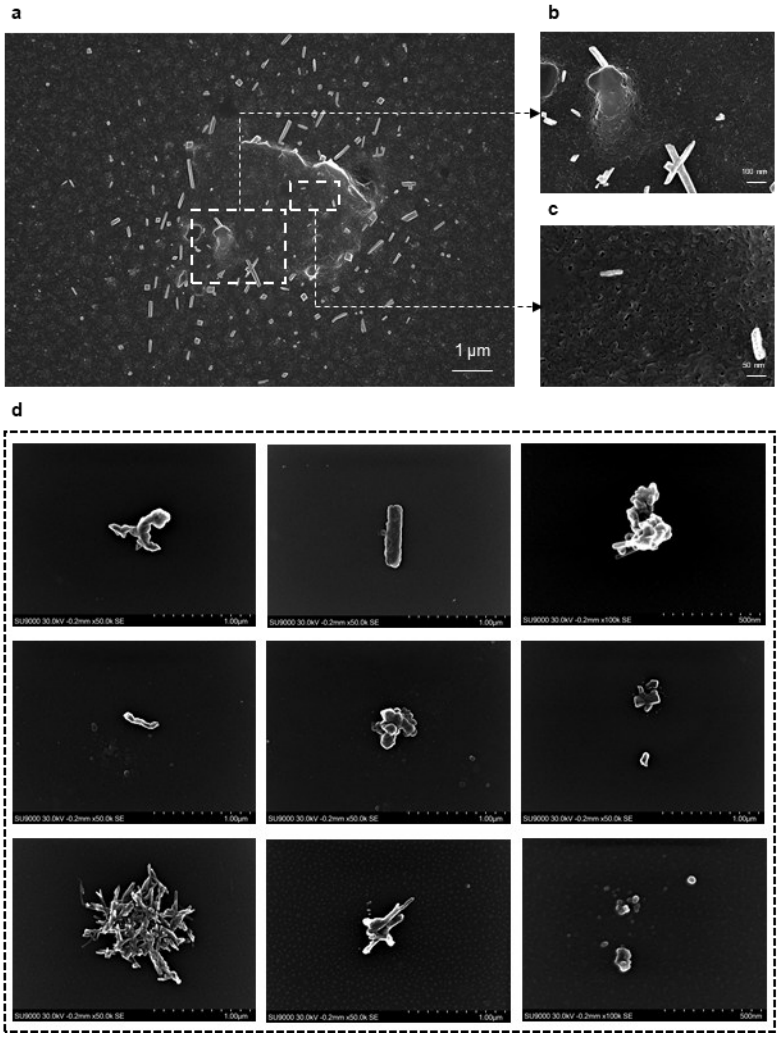


**Figure 46. SEM images of NPs in the environmental water samples.** NPs in environmental water are of irregular shapes.

In summary, it is essential to monitor micro/nanoplastic pollution to support a circular polymer economy, as these contaminants pose risks to environmental, animal, and human health. The European Commission has acknowledged a critical gap in reliable analytical tools for detecting, quantifying, and removing MPs and NPs, which hampers regulatory efforts.[52, 53] This

underscores the urgent need for enrichment and detection technologies that are broadly applicable.

In this study, the integrated use of bifunctional peptides, SPIONs, and Py-GC/MS offers a robust solution for quantifying NPs in a range of environmental waters, including lakes, rivers, seas, and wastewater. Using just one liter of sample, this method enabled the accurate detection and quantification of several nanoplastic types, including PP, PE, PS, PET, PC, Nylon 6, and Nylon 66, with detection limits as low as 0.81 ng for PC. The modular design of the bifunctional peptides ensures broad applicability. By replacing the NP-binding domain with peptides specific to other materials, the system can be adapted to capture various synthetic polymers (e.g., Teflon, carbon fibers) and inorganic particles (e.g., metals, metal oxides, silica).[137, 206-208] Given its versatility, the MagNanoTrap platform holds promise for use beyond environmental monitoring, where it may also be effective in analyzing industrial effluents, food matrices, or biological samples such as human tissues. Over time, it is anticipated that MagNanoTrap could become a standard tool for NP detection, supporting both researchers and policymakers in achieving Sustainable Development Goal 6 (SDG6) for clean and safe water.[209]

### 3.2 "Hooked for Decay" for NPs capture and degradation

Plastic pollution has become a significant environmental issue, particularly due to the persistence of MP/NPs, which need to be either removed or broken down efficiently to safeguard both environmental and human health. Achieving MP/NP-free water systems is a considerable challenge, as traditional water treatment technologies, such as coagulation, sedimentation, filtration, and disinfection, are generally inadequate for removing these particles effectively.[210-212] Many widely used polyolefins like PE, PS, and synthetic rubbers are chemically inert and resist natural degradation, largely due to the absence of effective biological catalysts.[213-215] Among these, elastomers such as SBR, a key component of tire polymers, are especially concerning. These materials break down into micro- and nanoscale fragments through mechanical abrasion and environmental weathering, contributing significantly to plastic contamination.[48, 49]

Recent research has introduced promising biohybrid catalysts based on the MBP LCI. One example includes a catalyst incorporating GH cofactor, which facilitates ring-opening metathesis polymerization (ROMP) of an oxanorbornene derivative to form a hydrophilic polynorbornene coating on surfaces like silica wafers and PP.[151] Another study reported a

Co(TACD)-based catalyst (TACD = 1,4,7,11-tetraazacyclododecane), which was immobilized on PS MPs via LCI and used oxone to drive oxidative degradation.[152]

In this section, we present a system termed "Hooked for Decay," which utilizes $Fe_3O_4$ magnetic beads coated with a hydrophobic film formed by a ROMP reaction. This system was created by immobilizing a GH-type cofactor onto $Fe_3O_4$ beads via the LCI_F16C peptide and catalyzing the polymerization of a modified hydrophobic norbornene derivative (Nor-C18). The resulting hydrophobic surface enabled these beads to "hook" and enrich various NPs from aqueous solutions. The captured SBR NPs were then subjected to ethenolysis, a degradation process targeting the internal C=C bonds in the 1,4-butadiene units, carried out in an organic solvent with ethylene gas but without requiring additional catalysts, thus demonstrating the system's "decay" function (Figure 47).

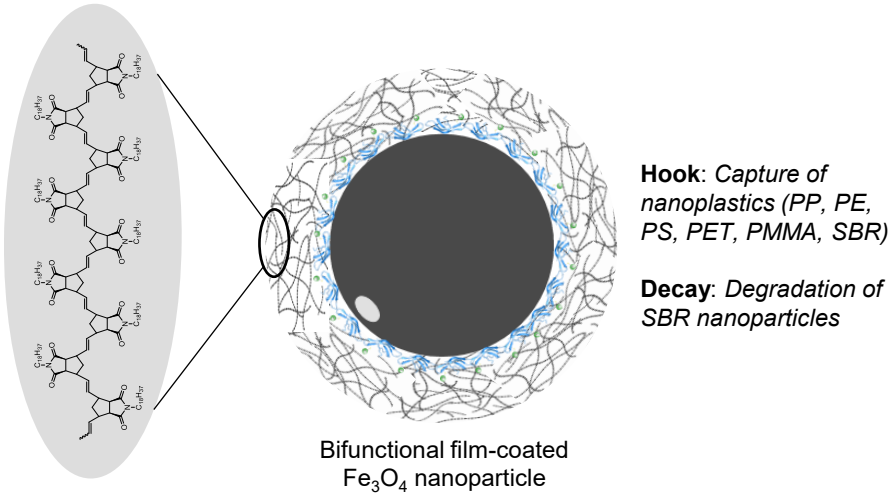


**Figure 47. Overview of the Hooked for Decay process for NPs capture and SBR degradation.** The GH-cofactors are immobilized on the SPION surface via peptide LCI, and initiate ROMP reaction to form a hydrophobic film for NPs capture. The GH-cofactor retains its ethenolysis catalytic function and breaks the internal C=C bonds of SBR.

To establish and validate the "Hooked for Decay" strategy for NPs capture and degradation, the following key steps were performed: (A) GH-cofactors were conjugated to the LCI_F16C peptide to create functional biohybrid catalysts; (B) The functionalized $Fe_3O_4$ particles were analyzed to confirm the successful formation of a polymer layer while ensuring uninfluenced magnetic properties; (C) Capture conditions were optimized, and assessment of the salt-out effects on NPs enrichment efficiency were investigated; and (D) The degradation of SBR was studied via ethenolysis, using the embedded GH-cofactors as catalysts.

### 3.2.1 Custom design of a biohybrid catalyst

Grubbs-Hoveyda cofactors **GH-C3**, **GH-C5**, and **GH-C10**, each featuring maleimide linkers of different spacer lengths, were synthesized according to a previously reported protocol for this study. These cofactors were covalently attached to the LCI_F16C peptide variant via the cysteine residue at position 16 using a Michael addition reaction (Figure 48). The conjugation was carried out in Tris-HCl buffer (20 mM, pH 7.5, 150 mM NaCl) containing 5% DMSO (v/v).

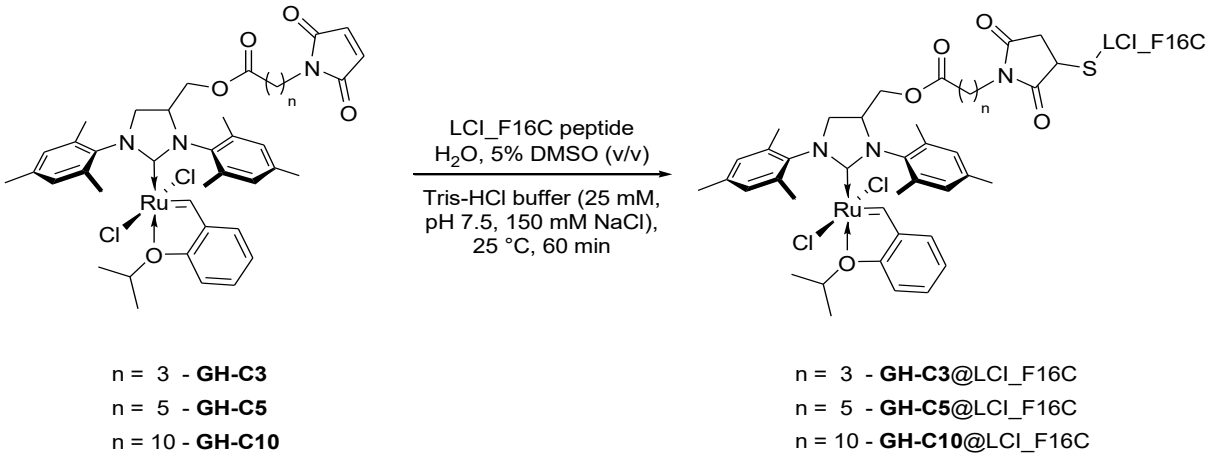


**Figure 48. Conjugation of GH-cofactors to LCI_F16C.** The conjugation is done by click chemistry between the maleimide linker and the free cysteine group in LCI.

To prevent disulfide bond formation between LCI_F16C peptides, dithiothreitol (DTT) was added prior to the conjugation with GH-cofactors. The resulting biohybrid catalysts, denoted as **GH-Cn**@LCI_F16C (where n = 3, 5, 10), were structurally modeled using YASARA software. These simulations were based on the resolved crystal structure of LCI available in the Protein Data Bank (PDB ID: 2B9K;[146] see Figure 49).

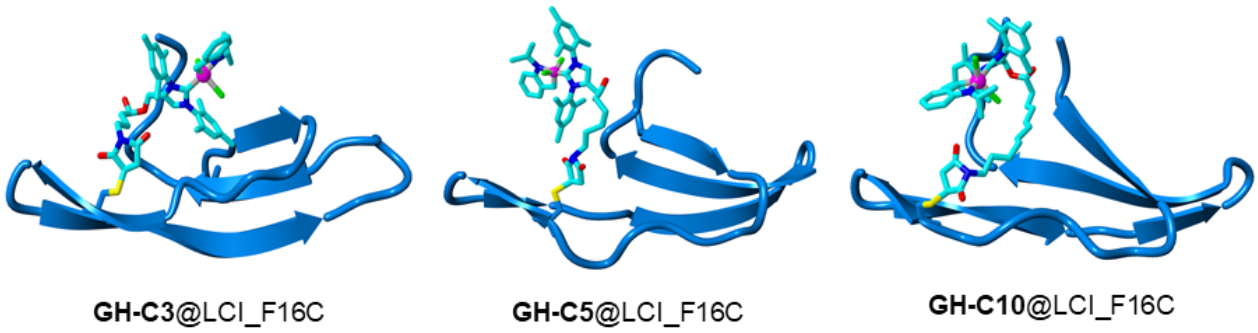


**Figure 49. Protein modelling of GH-C3@LCI_F16C, GH-C5@LCI_F16C, and GH-C10@LCI_F16C.**

The conjugation efficiency of GH-cofactors to LCI_F16C peptides, regardless of linker length, was assessed using ICP-OES. Results showed efficiencies exceeding 90%, confirming that each LCI_F16C peptide was successfully conjugated with one GH cofactor (Table 7).

**Table 7. ICP-OES results for conjugation of GH-cofactors to LCI_F16C.** The conjugation efficiency is around 90% confirmed by ICP-OES.

| Entry | Catalyst | Expected Ru content (ppm) | Measured Ru content (ppm) | Conjugation efficiency |
|---|---|---|---|---|
| 1 | no catalyst | 0.00 | 0.05 | --- |
| 2 | **GH-C3**@LCI_F16C | 3.61 | 3.27 ± 0.05 | 91% |
| 3 | **GH-C5**@LCI_F16C | 3.48 | 3.12 ± 0.05 | 90% |
| 4 | **GH-C10**@LCI_F16C | 3.96 | 3.51 ± 0.05 | 89% |

To further verify the conjugation yield, a cysteine titration assay was performed using the maleimide-based fluorescent probe ThioGlo-1. This method helps account for any potential non-covalent or nonspecific binding of GH cofactors to the peptide surface (Figure 50).[216, 217] When ThioGlo-1 was added to a solution containing free LCI_F16C, a substantial increase in fluorescence intensity was observed compared to the control without peptide. In contrast, the **GH-C3**@LCI_F16C, **GH-C5**@LCI_F16C, and **GH-C10**@LCI_F16C samples showed only a slight increase in fluorescence over the negative control. These results indicate that nearly all cysteine residues were conjugated, supporting a coupling efficiency of approximately 90%, consistent with the data obtained from ICP-OES analysis.

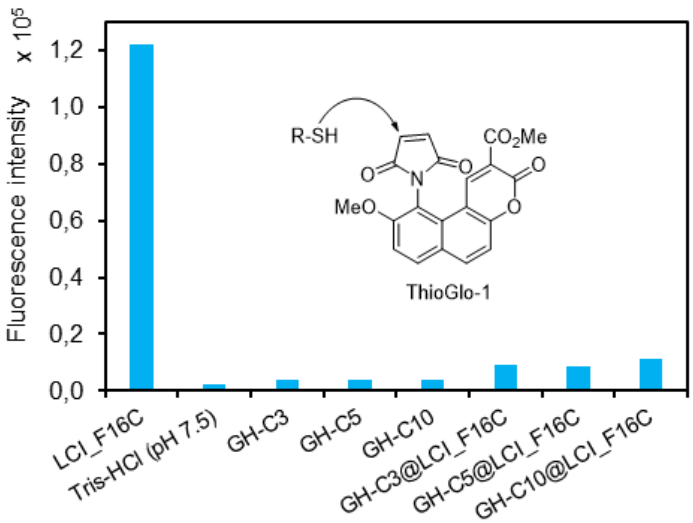


**Figure 50. Coupling of fluorescence indicator ThioGlo-1 to the biohybrid catalysts to determine the content of non-reacted -SH groups in LCI_F16C.** The conjugation efficiency is over 90% confirmed by the cysteine titration assay.

CD spectroscopy, measured in Tris-HCl buffer (50 mM, pH 8.0) at 25 °C, indicated by the characteristic minimum at λ = 210 nm (Figure 51), confirmed that the structural integrity of the LCI_F16C peptide was maintained in the biohybrid catalysts.

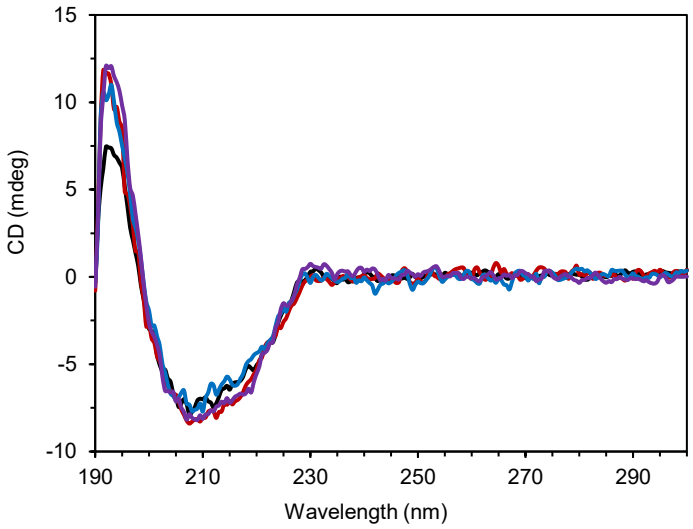


**Figure 51. CD spectra of LCI_F16C with and without conjugation of GH-cofactors.** The three-dimensional structure of LCI is not influenced by the cofactor conjugation.

The results above confirmed that the synthesized GH-cofactors were efficiently and successfully conjugated to the LCI_F16C peptide. The resulting biohybrid catalysts will next be evaluated for their functional performance, specifically assessing the ring-opening metathesis and ethenolysis activities contributed by the GH-cofactors, as well as the material-binding capability provided by the LCI peptide.

### 3.2.2 Investigation of successful film coating by material characterization

Figure 52 provides a schematic representation of the iron oxide nanoparticle coated with a hydrophobic film. In this design, the biohybrid catalyst **GH-C3**@LCI_F16C is anchored onto the iron oxide surface through the binding interaction of the LCI_F16C peptide. Simultaneously, the attached GH-cofactors, which incorporate a ruthenium catalytic center, rapidly drive a fast ROMP reaction, proceeding efficiently in water with methanol as a cosolvent at room temperature. This reaction produces an outer hydrophobic polynorbornene layer, formed from a custom-designed norbornene monomer bearing a modified C18 hydrophobic tail.

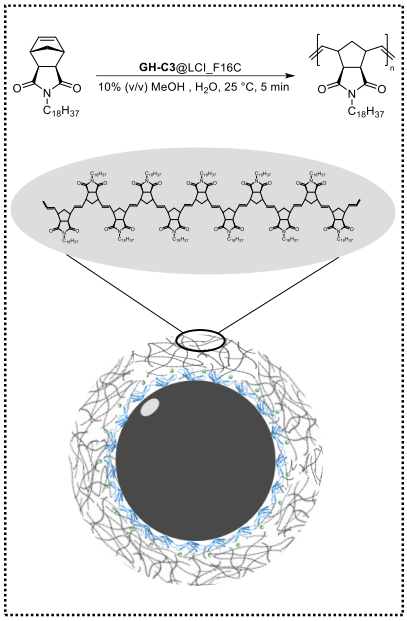


**Figure 52. Scheme illustrating the decoration of an iron oxide bead with a hydrophobic polynorbornene film.**

The successful immobilization of the biohybrid catalyst and formation of the polymer film were confirmed using fluorescence microscopy. A red fluorescent signal was detected after staining the biohybrid catalyst-coated iron oxide particles with Alexa Fluor 647-conjugated streptavidin, which specifically binds to the Strep-tag on the LCI peptide (Figure 53, left). Additionally, the formation of the polymer film on the $Fe_3O_4$ surface was validated by incorporating a thiol-containing monomer (Nor-SH, Figure 53, right) during polymerization. This was followed by labeling with the ThioGlo-1 dye, which reacts with thiol groups via a maleimide reaction, producing a green fluorescent signal.

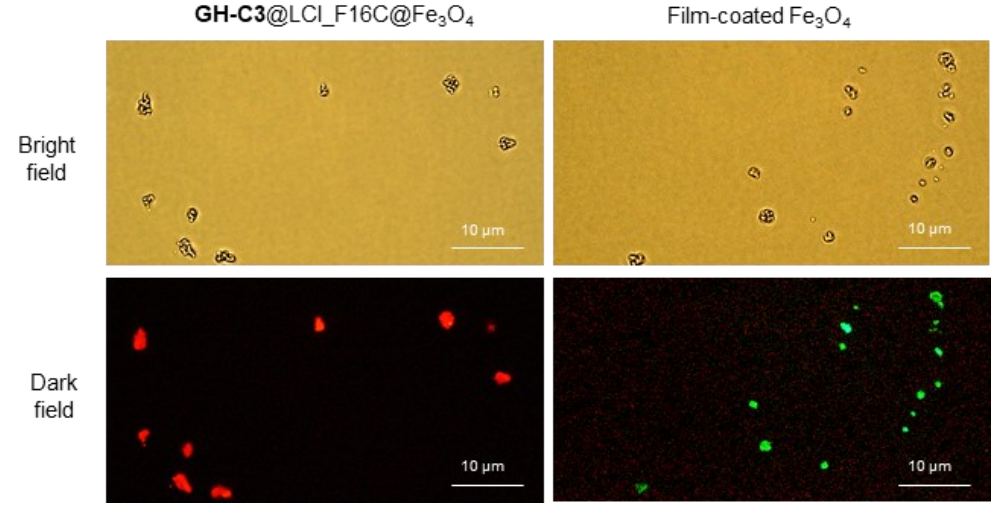


**Figure 53. Microscope images demonstrating the decoration of iron oxide nanoparticles with biohybrid catalyst GH-C3@LCI_F16C (left) and with generated polymer film (right).** The red fluorescence confirms the binding of LCI on SPION surface via interaction between the strep tag and streptavidin dye. The green fluorescence confirms the polymerization via the monomer with a free thiol group.

TGA revealed a clear and progressive increase in mass loss with each modification step (Figure 54). The initial mass loss of 6.5% observed for bare $Fe_3O_4$ rose to 16.3% after functionalization with the **GH-C3**@LCI_F16C biohybrid catalyst. Upon polymer film coating, the total mass loss further increased to 47.1%. The derivative thermogravimetric (DTG) curves displayed distinct peaks, each corresponding to a specific component introduced during the functionalization process, thereby confirming the successful incorporation of organic compounds onto the SPION surface. Collectively, these findings validate the efficient immobilization of the biohybrid catalyst and the subsequent formation of a polymeric layer.

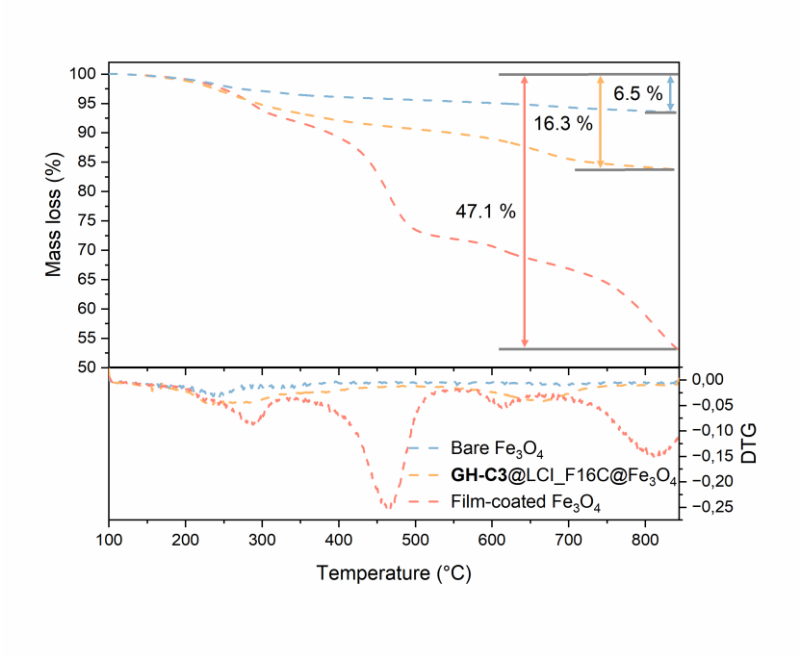


**Figure 54. TGA measurements of bare iron oxide (blue), GH-C3@LCI_F16C@iron oxide (orange), and film-coated iron oxide (red).** The stepwise mass loss and more peaks showing in the derivative curve indicate the successful peptide decoration and film formation.

XPS was used to analyze the surface chemical composition of the samples (Figure 55). As expected, the spectrum of bare $Fe_3O_4$ primarily showed signals for iron (Fe) and oxygen (O). A carbon (C) signal was also present, likely introduced during the nanoparticle synthesis process. Upon immobilization of the **GH-C3**@LCI_F16C biohybrid catalyst, a distinct nitrogen (N 1s) peak appeared, confirming the successful attachment of the LCI peptide to the iron oxide surface. In the case of the film-coated $Fe_3O_4$, a significant increase in the carbon (C 1s) peak was observed compared to the uncoated sample, indicating the successful formation of the polymer film. Together, these results confirm both the effective decoration of the biohybrid catalyst and the subsequent deposition of the hydrophobic polymer coating on the iron oxide surface.

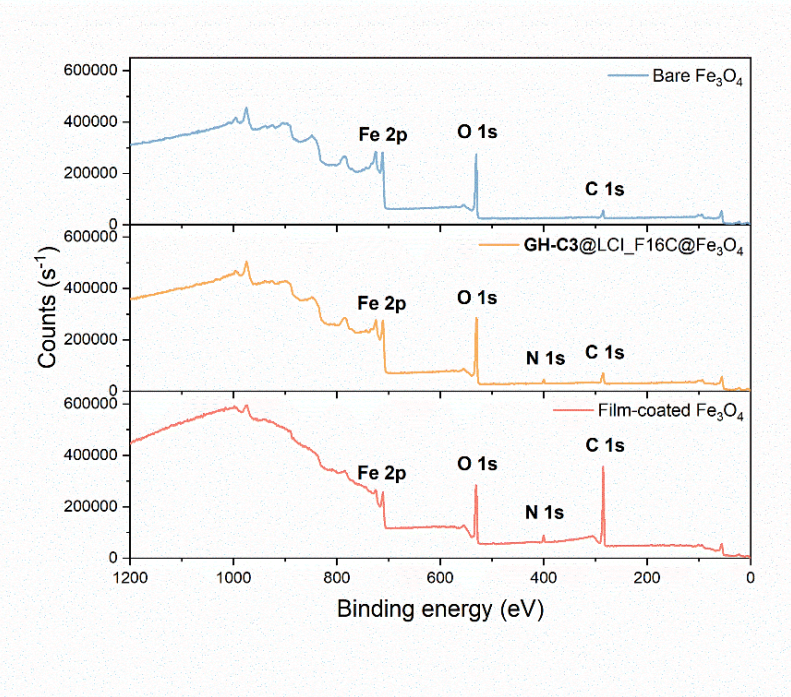


**Figure 55. XPS spectra of bare iron oxide (top), GH-C3@LCI_F16C@iron oxide (middle), and film-coated iron oxide (bottom).** The appearance of N 1s indicates the successful peptide decoration. The increase of the C 1s signal demonstrates the outer film formation.

FTIR was used to further investigate the surface modifications of iron oxide (Figure 56). For **GH-C3**@LCI_F16C@$Fe_3O_4$, new absorption peaks appeared at 1248, 1539, and 1643 $cm^{-1}$, corresponding to the amide III, II, and I bands, respectively. These signals confirmed the successful attachment of the peptide to the nanoparticle surface. Additionally, weak peaks at 2909 and 2982 $cm^{-1}$ were observed, which can be attributed to C–H stretching vibrations from the aliphatic side chains of the peptide. In the case of the film-coated $Fe_3O_4$, strong peaks at 2848 and 2915 $cm^{-1}$ were detected, indicating the presence of long $C_{18}$ hydrocarbon chains from the monomer. A distinct peak at 1697 $cm^{-1}$ was also present, corresponding to the C=O stretching of the monomer backbone. These spectral features collectively verified the successful attachment of the biohybrid catalyst and formation of a hydrophobic polymer film surrounding the $Fe_3O_4$ nanoparticles.

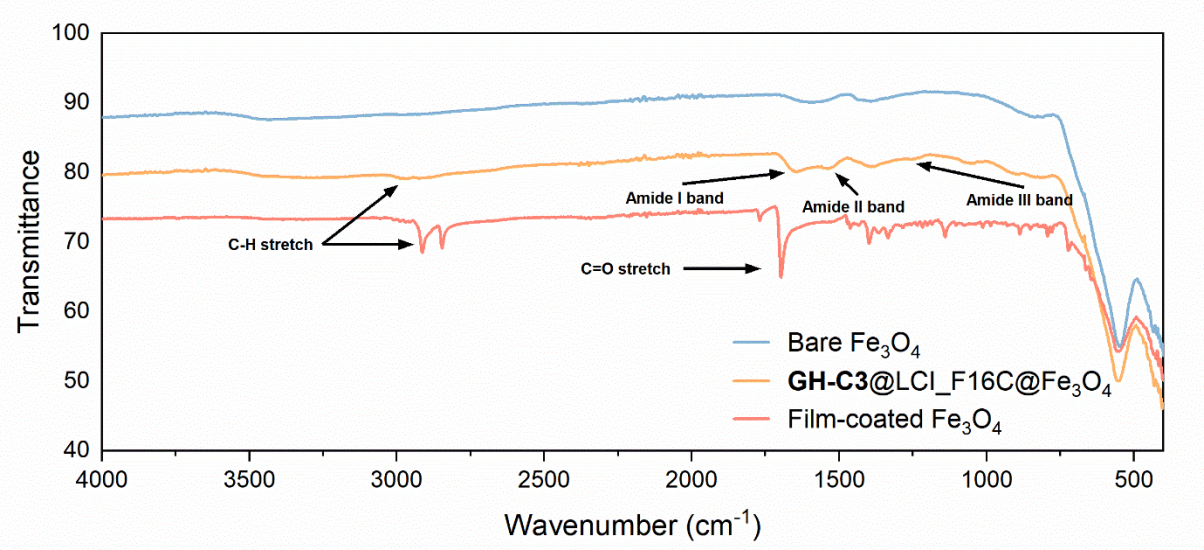


**Figure 56. FTIR spectra of bare iron oxide (blue), GH-C3@LCI_F16C@iron oxide (orange), and film-coated iron oxide (red).** The amide bands and C-H stretch signals represent peptide presence. The C=O stretch is from the monomer structure, indicating the film formation.

The polymer film (poly-Nor-C18), generated through ROMP of Nor-C18, was analyzed using $^{1}$H NMR spectroscopy (Figure 57). The spectrum displayed characteristic olefinic proton signals in the range of 5.4 to 5.7 ppm, confirming successful polymer formation.

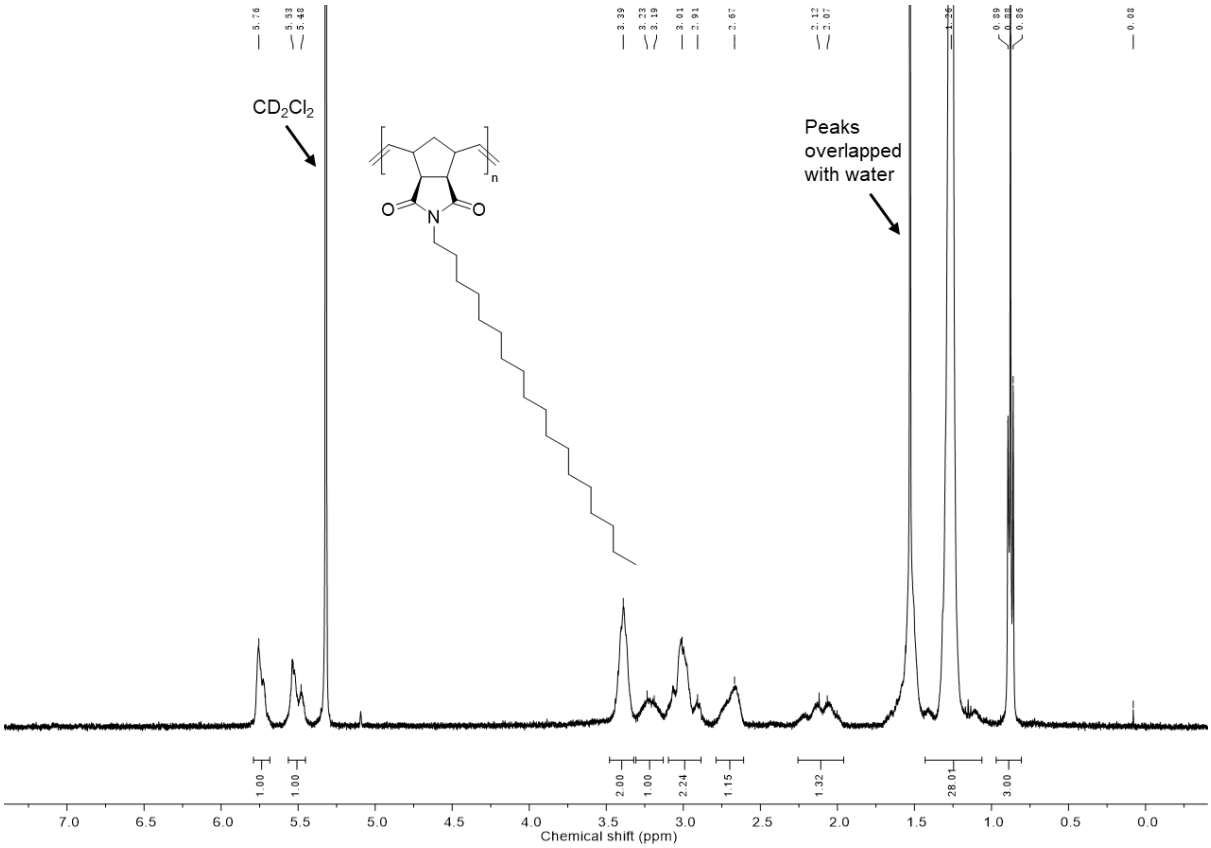


**Figure 57. 1H NMR spectrum of the film formed after ROMP of Nor-C18 (400 MHz, CD2Cl2, 298 K).**

Vibrating sample magnetometry (VSM) analysis revealed that the magnetic properties of the iron oxide remained unaffected by the decoration of the polymer film (Figure 58). The iron oxide nanoparticles retained their superparamagnetic behavior, exhibiting a magnetic moment exceeding 40 emu/g.

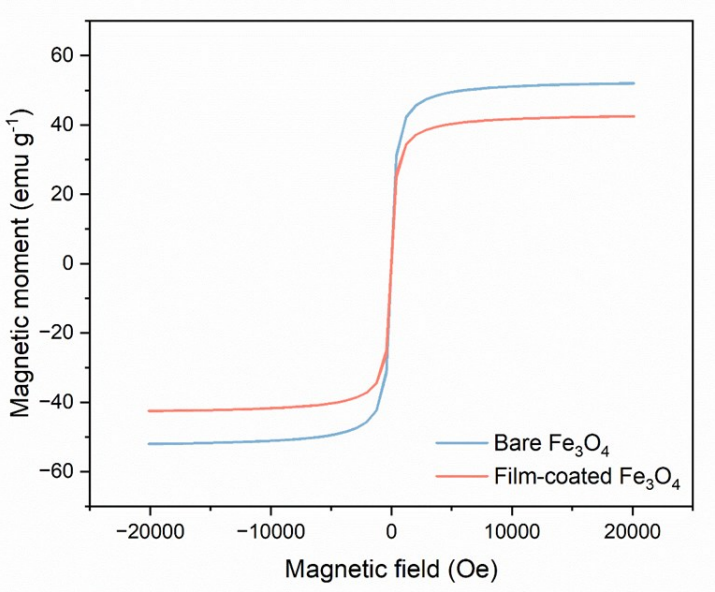


**Figure 58. Magnetization of bare Fe3O4 (blue) and film-coated Fe3O4 (red) through a vibrating sample magnetometer.** The nanocoating of the thin film doesn't affect the superparamagnetic properties of SPIONs.

SEM images revealed that the iron oxide nanoparticles aggregated into secondary structures with an average size of around 500 nm (Figure 59). After polymer film decoration, these aggregates displayed a noticeably smoother surface morphology compared to the bare iron oxide particles.

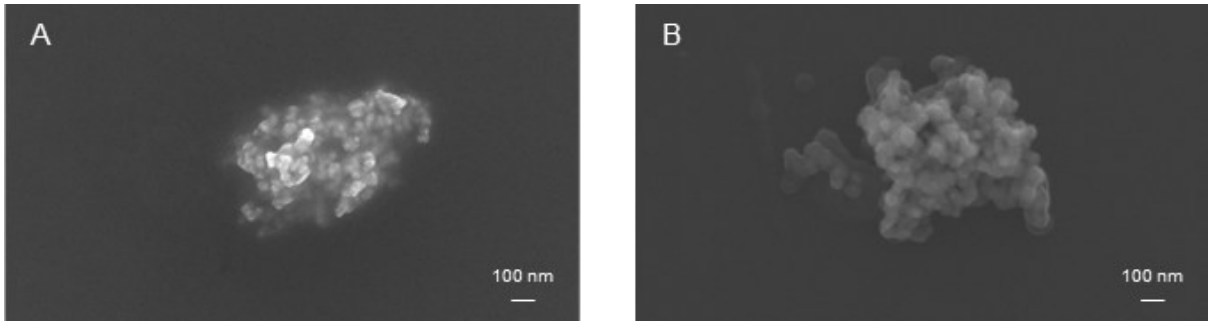


**Figure 59. SEM images of bare iron oxide (A) and film-coated iron oxide (B) nanoparticles.** The film formation makes the surface smoother, compared with the bare iron oxide.

The characterization results collectively verify the successful functionalization of iron oxide beads with the biohybrid catalyst **GH**@LCI_F16C, along with the formation of the polynorbornene outer film. This decorated system will be utilized in the subsequent experiments for NPs capture from water and the degradation of SBR NPs.

### 3.2.3 Evaluation of NPs enrichment performance by "Hooked for Decay" system in a 200 µL-scale reaction

Enrichment experiments were conducted using 500 nm PS-COOH NPs in a reaction volume of 200 µL to assess the performance of the film-coated iron oxide beads. As illustrated in Figure 60, a six-step workflow was developed to evaluate the enrichment efficiency of the platform, incorporating an absorbance-based method to quantify nanoparticle capture. In the first step, iron oxide beads were functionalized with the **GH-C3**@LCI_F16C biohybrid catalyst in Tris buffer (50 mM, pH 8). In the second step, the decorated beads were washed with water and subsequently incubated with the norbornene monomer dissolved in methanol. In the third step, another washing step with water was performed to remove excess monomer. In step four, the film-coated beads were incubated with PS-COOH$_{500\ nm}$ NPs in the presence of NaCl to facilitate enrichment. During step five, magnetic separation was applied to isolate the bead–NP complexes. Finally, in step six, the supernatant containing the non-captured PS-COOH$_{500\ nm}$ NPs was collected, and its absorbance was measured to determine the efficiency of NPs capture.

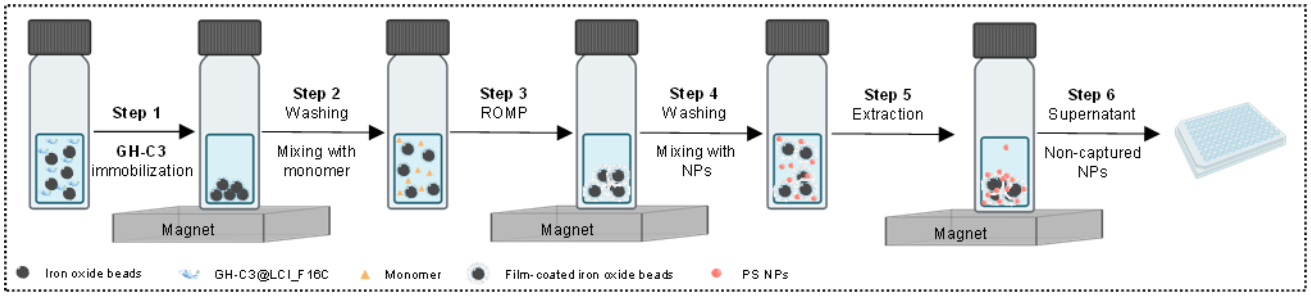


**Figure 60. Scheme of the six-step workflow developed for assessing the enrichment performance of the "Hooked for Decay" platform on a 200 µL scale.** In Step 1, SPIONs were decorated with GH-C3@LCI_F16C in 50 mM Tris, pH 8; in Step 2, the coated beads were washed with water, followed by mixing with monomer dissolved in methanol; in Step 3, the further coated beads were washed again with water; in Step 4, the coated beads were mixed with NPs in the presence of NaCl; in Step 5, beads-NPs complex was extracted by a magnet; and in Step 6, the supernatant containing non-captured NPs was taken for absorbance measurement.

Prior to conducting the enrichment of PS NPs, the optimal concentration of the biohybrid catalyst **GH**@LCI_F16C for decorating iron oxide beads was determined using fluorescence-based analysis. A range of LCI_F16C peptide concentrations (post-DTT reduction) was incubated with bare iron oxide beads under shaking conditions (1200 rpm for 1 minute). After incubation, the supernatant from each sample containing unbound peptide was collected and reacted with ThioGlo-1 dye. This dye specifically binds to free thiol groups present on LCI_F16C, resulting in a fluorescent signal. Fluorescence intensity was then measured to quantify the amount of peptide that bound to the bead surface.

A calibration curve for LCI_F16C concentration versus fluorescence was established using the equation y = 10915.2x – 191.2 ($R^2$ = 0.9994), which was valid for peptide concentrations between 2 µM and 10 µM (Figure 61). Based on these measurements, it was determined that a concentration of 3 µM LCI_F16C was sufficient to achieve saturated binding to 0.075 g/L of $Fe_3O_4$ nanoparticles.

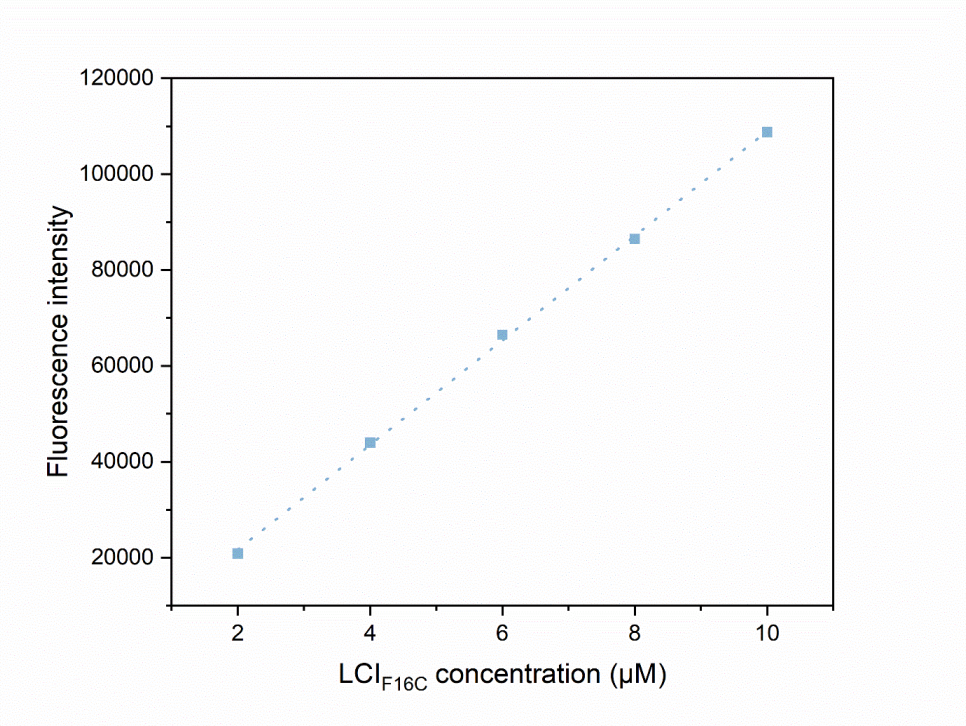


**Figure 61. Standard curve of LCI_F16C protein concentration.**

As described in the workflow, an absorbance-based method was developed to quantify PS NPs. To establish this method, various concentrations of PS-$COOH_{500\ nm}$ NPs were analyzed across the full UV spectrum. The goal was to identify the wavelength that offered the most reliable linear relationship within the expected concentration range.

For PS-$COOH_{500\ nm}$ NPs, 460 nm was determined to be the optimal wavelength for measurement. At this wavelength, the absorbance data produced a calibration curve with the equation y = 5.4455x + 0.0041 and an excellent correlation coefficient ($R^2$ = 0.9998, Figure 62). This calibration curve was then applied to quantify PS NPs during the 200 µL enrichment experiments and to calculate NPs recoveries.

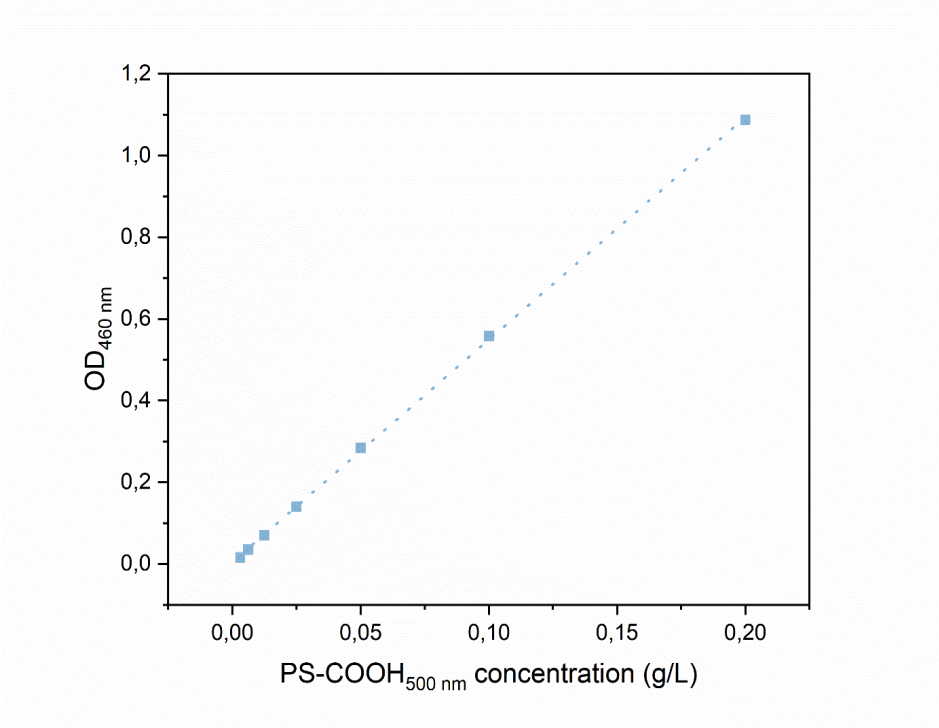


**Figure 62. Standard curve of PS-COOH$_{500\ nm}$ at OD460 measured by UV absorbance measurement.**

To fine-tune the ROMP reaction conditions for effective outer film formation, key variables, including monomer concentration, polymerization duration, and the linker length between the GH-cofactor and the LCI_F16C peptide, were systematically assessed. Each condition was evaluated based on its impact on NPs enrichment performance.

The optimization experiments were conducted using 0.075 g/L iron oxide beads decorated with the biohybrid catalyst GH-C3@LCI_F16C and 0.2 g/L PS-COOH$_{500\ nm}$ NPs, in the presence of 100 mM NaCl with a 30s shaking period. As illustrated in Figure 63, the optimal condition was identified as a monomer concentration of 500 µM with a polymerization time of five minutes, which yielded the highest NPs adsorption capacity. With a shorter reaction time, the polymer film is not formed completely to cover the $Fe_3O_4$ nanoparticles, leading to inefficient adsorption. If the reaction time is too long, the $Fe_3O_4$ nanoparticles will aggregate, leading to less adsorption capacity.

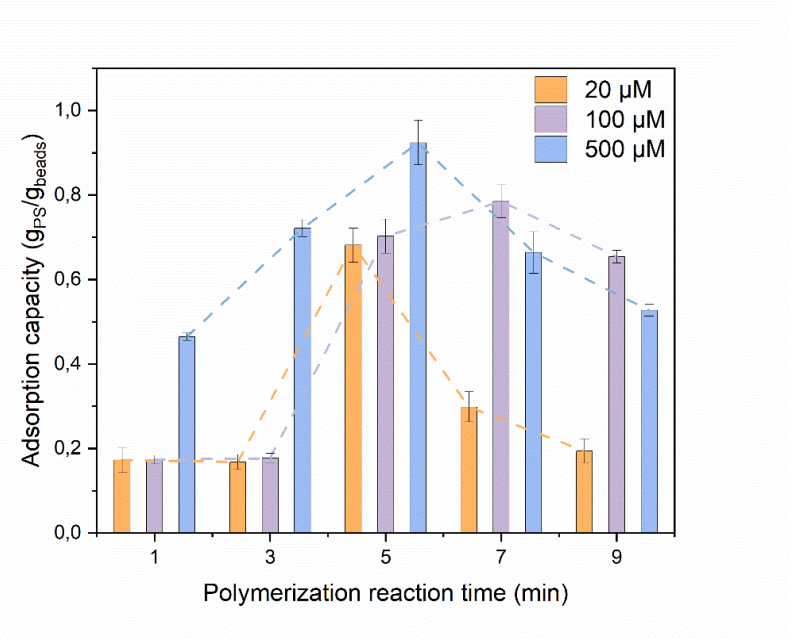


**Figure 63. Adsorption capacity of PS-COOH$_{500\ nm}$ NPs at increasing monomer concentration and polymerization time.** With a short polymerization time, the formed film is not intact, leading to poor enrichment efficiency. With a long polymerization time, the film-coated beads form aggregation, resulting in decreased adsorption.

Figure 64 demonstrates that the biohybrid catalyst **GH-C3**@LCI_F16C, which incorporates the shortest linker, exhibits superior enrichment performance compared to the variants with longer linkers, GH-C5 and GH-C10. This improved performance is likely due to the positioning of the ruthenium center in closer proximity to the surface of LCI_F16C, which optimizes the interaction between the catalyst and its surrounding environment.

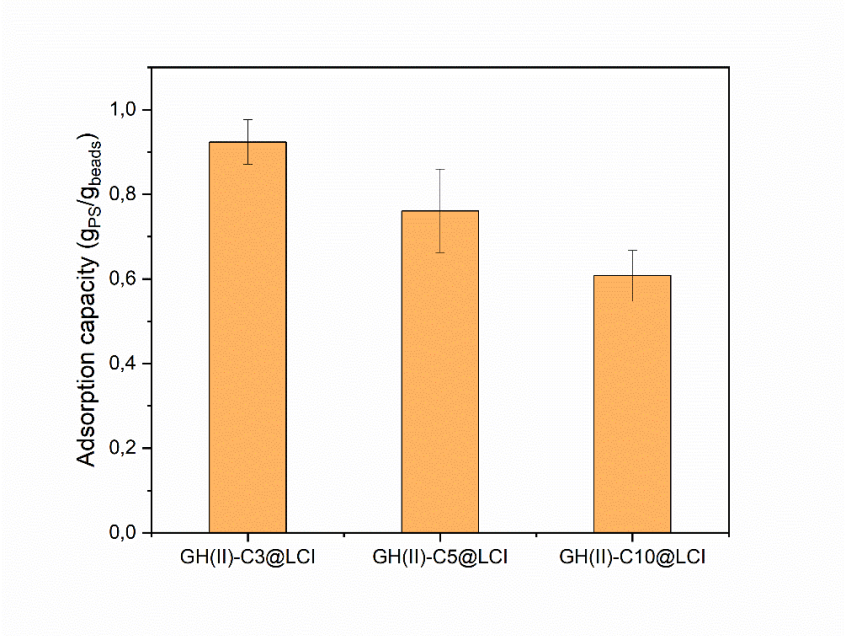


**Figure 64. Adsorption capacity of PS-COOH$_{500\ nm}$ NPs at increasing linker length between the GH-cofactor and LCI_F16C peptide.** With a short linker, the GH-cofactor center is closer to the protein surface, optimizing the interaction between the metal and the surrounding environment.

Using the optimized conditions for outer film formation, the film-coated iron oxide beads achieved a 99% recovery rate for PS-$COOH_{500\ nm}$ NPs. In comparison, unmodified iron oxide beads captured only 3% of the NPs (Figure 65). This stark contrast confirms that the polymer outer film significantly enhances the NPs capture efficiency.

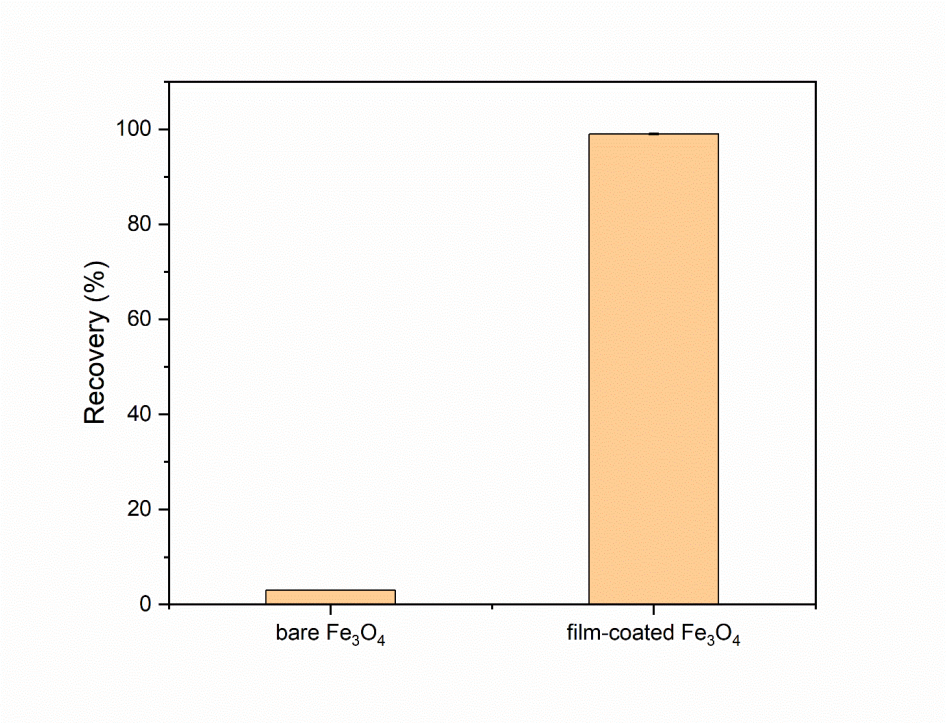


**Figure 65. Recovery of bare and film-coated iron oxide beads (75 mg/L) for 0.1 g/L PS-$COOH_{500\ nm}$ NPs at 100 mM NaCl.** The formed hydrophobic film around the SPIONs significantly enhances the NPs' adsorption.

Scanning electron microscopy (SEM) provided visual confirmation of agglomerate formation, indicating that the PS-$COOH_{500\ nm}$ NPs were successfully captured by the film-coated $Fe_3O_4$ beads (Figure 66).

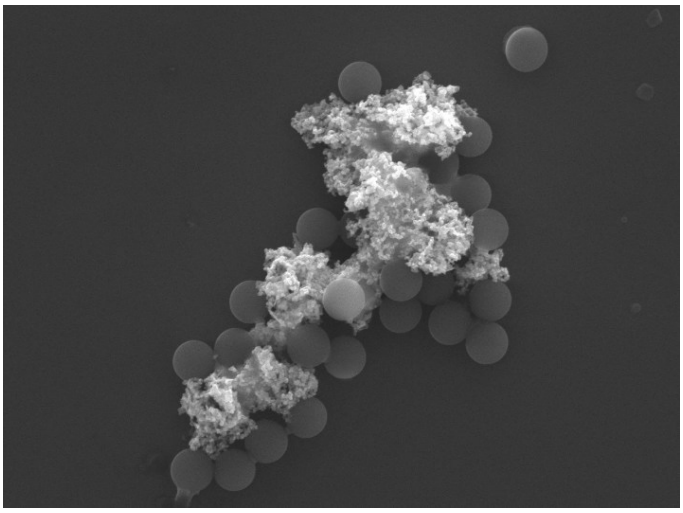

**Figure 66. SEM images of PS-$COOH_{500\ nm}$ NPs captured by film-coated iron oxide beads.**

To demonstrate the broad applicability of the film-coated $Fe_3O_4$ beads, five additional types of NPs were introduced into deionized water. These included commercially available PMMA NPs, as well as PP, PE, and SBR NPs synthesized via an emulsification–solvent evaporation method, and PET NPs prepared through nanoprecipitation. Additionally, PS NPs were spiked into four different environmental water samples, including wastewater, river, lake, and seawater. Upon treatment with the film-coated $Fe_3O_4$ and 10 minutes of shaking, all NP suspensions became visually clear after magnetic extraction, as shown in Figures 67 and 68. This observation confirms the effective magnetic capture and removal capability of the system, highlighting the versatile potential of the "Hooked for Decay" platform across diverse plastic nanoparticle types.

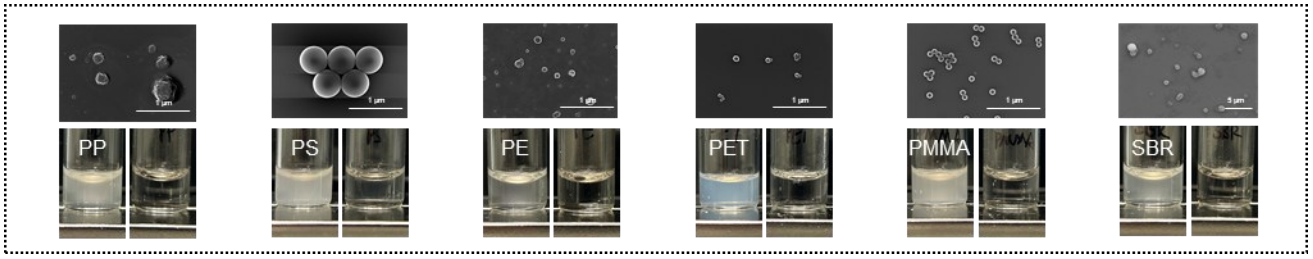


**Figure 67. Visualization of 0.2 g/L of dispersed PP, PS, PE, PET, PMMA, and SBR NPs (SEM images, top) before (bottom left) and after magnetic extraction (bottom right) by employing film-coated iron oxide beads.** The film-coated SPIONs can be applied to various types of NPs enrichment.

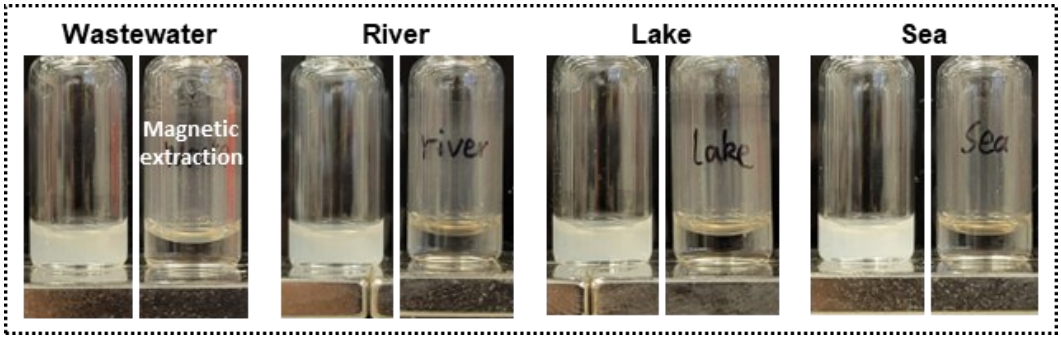


**Figure 68. Visualization of 0.2 g/L of dispersed PS NPs in wastewater, river, lake, and sea before (left) and after magnetic extraction (right) by employing film-coated iron oxide beads.** The film-coated SPIONs can be applied to various environmental matrices for NPs enrichment.

### 3.2.4 Investigation of NPs adsorption by "Hooked for Decay" system under the salting-out effect

The influence of NaCl on the adsorption behavior of PS NPs was assessed by varying salt concentrations in the "Hooked for Decay" enrichment system. This evaluation aimed to clarify how ionic strength affects both adsorption kinetics and isotherms. At higher NaCl concentrations, the interactions between water and both the film-coated $Fe_3O_4$ beads and PS NPs are reduced, promoting hydrophobic interactions as the dominant driving force for NPs binding.[188]

Kinetic studies demonstrated that 0.2 g/L of PS-COOH$_{500\ nm}$ NPs were rapidly captured by 0.075 g/L of film-coated $Fe_3O_4$ in the presence of 100 mM NaCl, with the system reaching adsorption saturation within 10 minutes (Figure 69). The data aligned closely with the pseudo-second-order kinetic model, showing an $R^2$ value greater than 0.99, suggesting that the process is largely controlled by the number of available binding sites.[180] In comparison, the pseudo-first-order model showed a slightly lower fit, with an $R^2$ of approximately 0.985 (Table 8).

The adsorption rate constant ($k_2$) was found to increase markedly with higher salt concentrations, rising from 0.39 ± 0.02 g/(g·min) at 100 mM NaCl to 0.67 ± 0.05 g/(g·min) at 200 mM, indicating that salt significantly enhances adsorption kinetics. Meanwhile, the equilibrium adsorption capacity ($q_e$) remained relatively stable under varying salt concentrations, with values of 2.10 ± 0.03 g/g, 2.12 ± 0.03 g/g, and 2.19 ± 0.03 g/g at 100, 150, and 200 mM NaCl, respectively.

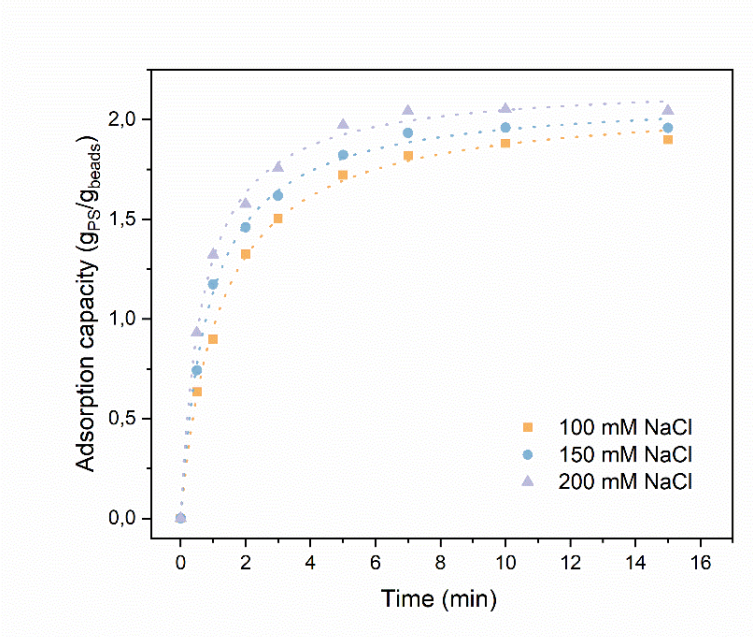


**Figure 69. Adsorption kinetics to determine enrichment of PS-COOH$_{500\ nm}$ NPs at varied salt concentrations fitted with a pseudo-second-order model.** With higher NaCl concentration, the reaction becomes faster and reaches the maximum adsorption within 10 min of shaking.

**Table 8. Parameters of the adsorption kinetics equation of film-coated $Fe_3O_4$ against PS-COOH$_{500\ nm}$ NPs at different NaCl concentrations.**

| | Pseudo-first-order model | | | Pseudo-second-order model | | |
|---|---|---|---|---|---|---|
| NaCl concentration | $q_e$ (g/g) | $k_1$ (min$^{-1}$) | $R^2$ | $q_e$ (g/g) | $k_2$ (g/(g·min)) | $R^2$ |
| 100 mM | 1.84 | 0.65 | 0.9917 | 2.10 | 0.39 | 0.9979 |
| 150 mM | 1.90 | 0.85 | 0.9855 | 2.12 | 0.54 | 0.9977 |
| 200 mM | 1.99 | 1.02 | 0.9803 | 2.19 | 0.67 | 0.9970 |

Isotherm studies were also carried out to analyze the adsorption behavior, with the data fitted to both the Langmuir and the Freundlich models.[181] The results showed a strong correlation with the Langmuir model, with $R^2$ values exceeding 0.99, suggesting that the adsorption occurs as a monolayer on a homogeneous surface (Figure 70 and Table 9). In contrast, the Freundlich model showed a poorer fit, with $R^2$ values below 0.92.

The maximum adsorption capacity ($q_m$), as determined from the Langmuir model, increased with rising NaCl concentrations, reaching 5.53 ± 0.29 g/g at 200 mM NaCl. This capacity significantly exceeds those of many previously reported systems, including SPIONs-PAC18,[105] which achieved 0.69 g/g for PS NPs, and iron oxide nanoflowers,[218] which showed 1 g/g for PE MPs.

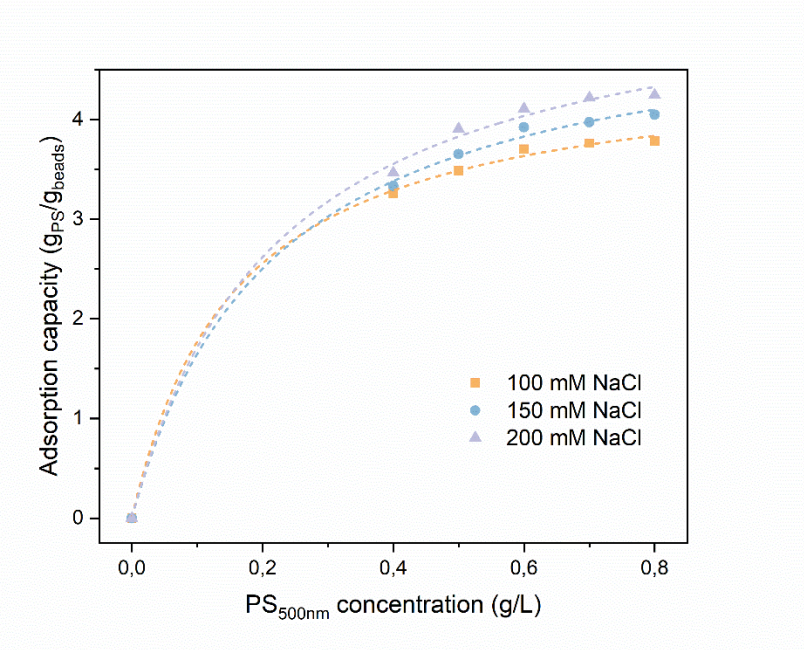


**Figure 70. Adsorption isotherms to determine enrichment of PS-COOH$_{500\ nm}$ NPs at varied salt concentrations fitted with a Langmuir model.** Adsorption capacity reaches 5.53 g/g for PS NPs.

**Table 9. Parameters of the adsorption isotherm equation of film-coated $Fe_3O_4$ against PS-COOH$_{500\ nm}$ at different NaCl concentrations.**

| | Freundlich model | | | Langmuir model | | |
|---|---|---|---|---|---|---|
| NaCl concentration | 1/n | $K_F$ (L/g) | $R^2$ | $q_m$ (g/g) | $K_L$ (L/g) | $R^2$ |
| 100 mM | 0.22 | 4.04 | 0.9242 | 4.60 | 6.25 | 0.9992 |
| 150 mM | 0.27 | 4.38 | 0.9279 | 5.21 | 4.62 | 0.9988 |
| 200 mM | 0.28 | 4.62 | 0.8942 | 5.53 | 4.50 | 0.9980 |

To further evaluate the salt effect hypothesis, enrichment experiments were performed using 100 mM solutions of various monovalent cations, with a reaction time of 30 seconds. The film-

coated iron oxide beads exhibited different adsorption capacities toward PS-COOH$_{500\ nm}$ NPs depending on the cation present. The observed trend in adsorption followed the sequence: $NH_4^+$ > $K^+$ > $Rb^+$ > $Cs^+$ > $Na^+$ > $Li^+$ (Figure 71). This order is consistent with the Hofmeister series and highlights the influence of cation-induced salting-out effects on NPs adsorption.

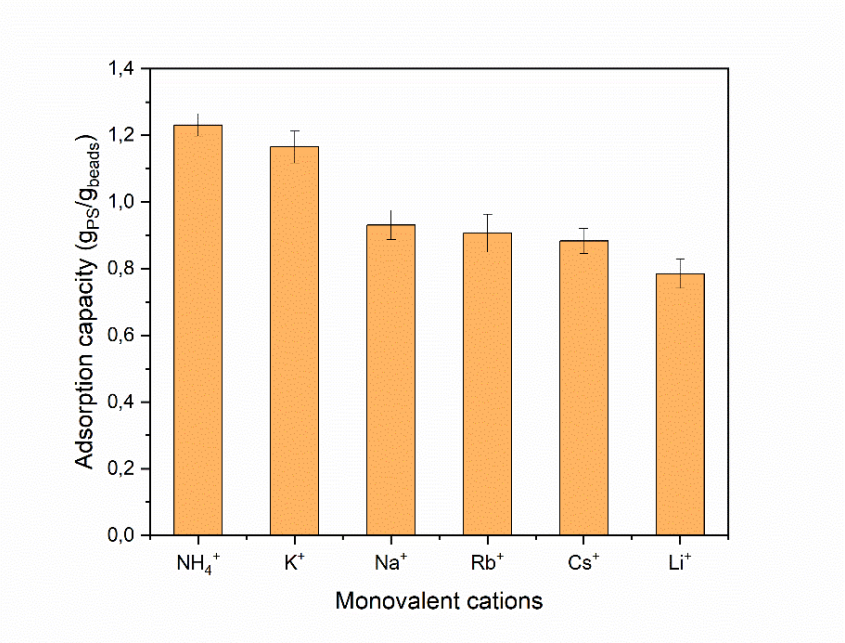


**Figure 71. Adsorption capacity of PS-COOH$_{500\ nm}$ NPs by employing film-coated iron oxide in the presence of 100 mM monovalent cations during a 30-s shaking period.** The enrichment performance follows the Hofmeister series.

The use of high salt concentrations extends the applicability of the "Hooked for Decay" system to a wide range of water samples by promoting hydrophobic interactions as the dominant force driving NPs binding to the film-coated $Fe_3O_4$ beads.

### 3.2.5 SBR degradation

The previous results highlight the "Hooked" capability of the film-coated iron oxide beads in capturing NPs, and the "Decay" function is demonstrated by the following data. After the enrichment step, the SBR NPs were further degraded through ethenolysis, catalyzed by the embedded biohybrid catalyst (**GH-C3**@LCI_F16C), which targets the polymer's internal C=C bonds (Figure 72). In this step, microaggregates formed from the enriched SBR NPs on film-coated $Fe_3O_4$ beads were directly transferred into an organic solvent mixture (*p*-xylene/THF, 1:1) to dissolve the SBR material. As both the SBR NPs and the polynorbornene film dissolve, the embedded biohybrid catalyst becomes exposed, enabling it to interact with the SBR polymer as its substrate.

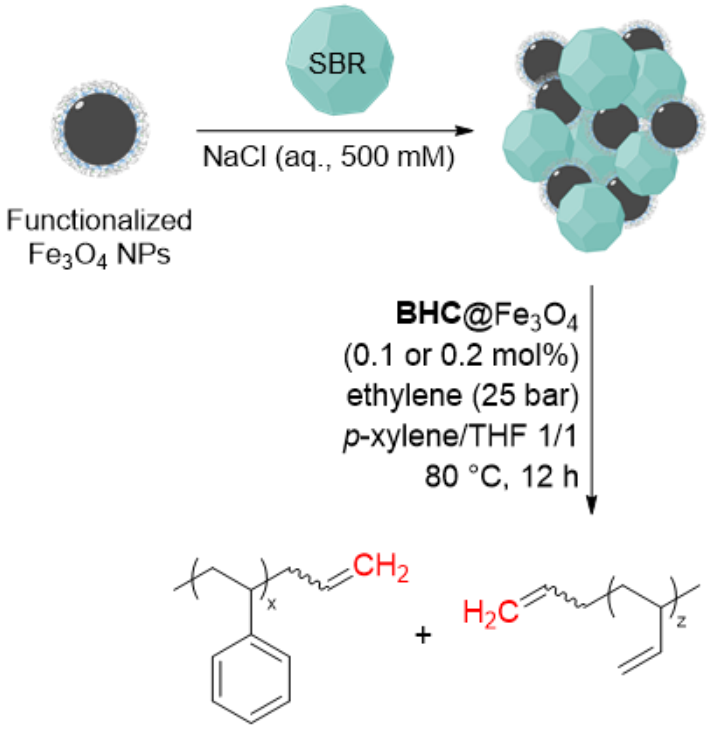


**Figure 72. Enrichment of SBR nanoparticles using film-coated $Fe_3O_4$ beads with subsequent ethenolysis reaction catalyzed by GH-C3@LCI_F16C to break down the internal C=C bonds.**

The degradation reaction was carried out in a sealed stainless-steel reactor charged with ethylene gas. To maintain a sufficient ethylene concentration at the reaction temperature of 80 °C, the initial pressure was set to 25 bars. The ethylene pressure was tracked over a 12-hour period, during which a slight decline was observed, indicating that ethylene was being consumed during the reaction (Figure 73).

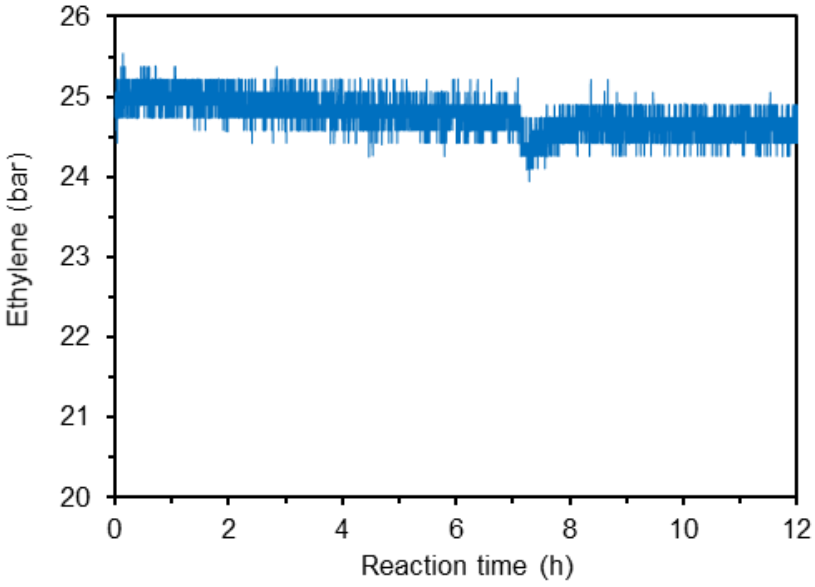


**Figure 73. Pressure monitoring during the ethenolysis process.** The decrease in ethylene pressure indicates the breaking of internal C=C bonds in SBR.

Following the ethenolysis reaction, the biohybrid catalyst immobilized on iron oxide beads was easily separated from the reaction mixture using an external magnetic field. The resulting degradation products were then analyzed and quantified using $^{1}$H NMR spectroscopy (Figure 74). In comparison to the untreated SBR polymer, new signals appeared in the 4.9–4.5 ppm region, corresponding to the protons of terminal C=C bonds, confirming the formation of degraded SBR fragments. Based on the $^{1}$H NMR spectra, the degradation efficiency of SBR NPs was determined to be between 4.1% and 6.5%, depending on the catalyst loading (0.1 and 0.2 mol%, respectively), relative to the 1,4-butadiene units. The biohybrid catalyst maintained its catalytic activity during the ethenolysis process, likely due to the protective effect of the hydrophobic polymer film surrounding the GH-cofactors (**GH-C3**), which helps shield it from potentially deactivating salt ions. These findings highlight the stability and dual catalytic functionality of the **GH-C3**@LCI_F16C system in both NPs enrichment ("Hook") and degradation ("Decay").

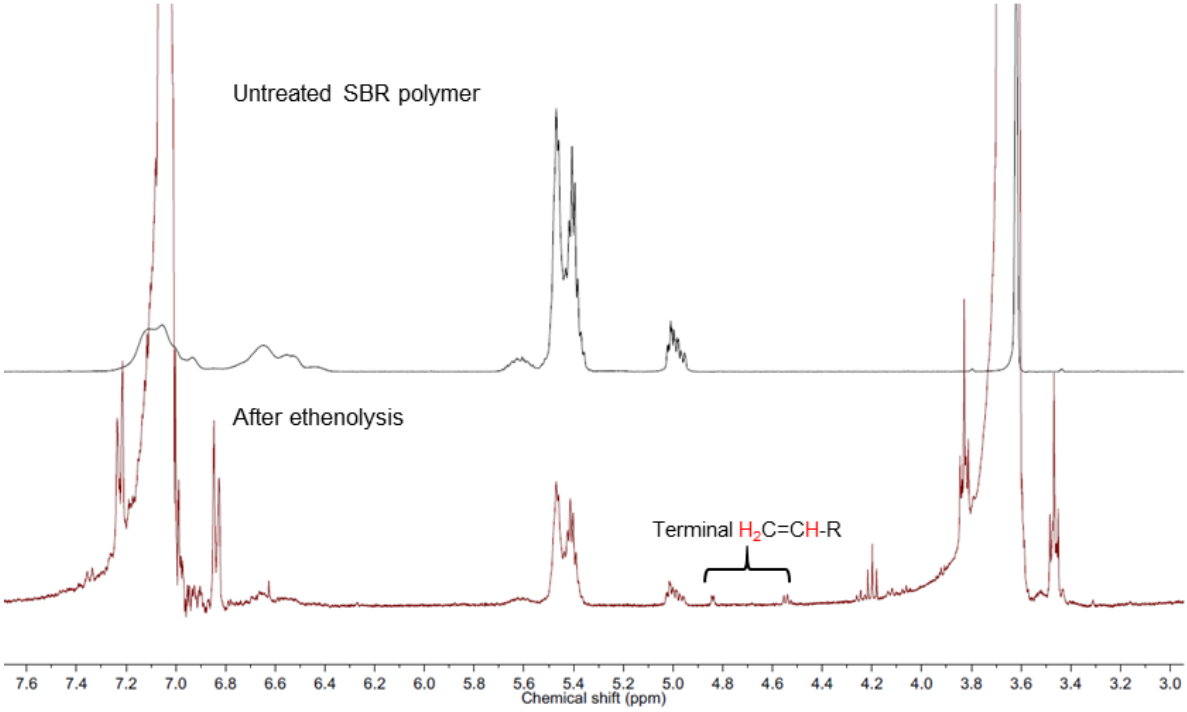


**Figure 74. $^{1}$H NMR spectra of SBR polymer before (top) and after (bottom) ethenolysis.** The appearance of the terminal C=C bond signal indicates the breaking of the internal C=C bond in SBR.

In summary, the bifunctional "Hooked for Decay" biohybrid catalyst (**GH-C3**@LCI_F16C), consisting of a Grubbs-Hoveyda cofactor and a material-binding peptide variant of LCI, proved highly effective for capturing and removing various hydrophobic NPs, including PP, PE, PS, PET, PMMA, and SBR. The hydrophobic polynorbornene-coated $Fe_3O_4$ beads enabled rapid adsorption of PS NPs within just 10 minutes of shaking and demonstrated a high adsorption

capacity of 5.53 ± 0.29 g/g for PS-$COOH_{500\ nm}$ NPs, outperforming previously reported $Fe_3O_4$-based materials. Notably, up to 99% recovery of NPs was achieved in the presence of 100 mM NaCl, where hydrophobic interactions became the dominant mechanism for binding, thus supporting the system's broad applicability across diverse aqueous environments. The Grubbs-Hoveyda cofactor exhibited dual functionality, contributing both to the formation of the polymer coating and the ethenolysis-driven degradation of SBR NPs, with a degradation efficiency of up to 6.5%. These findings illustrate the potential of this platform not only for the effective removal but also the chemical breakdown of synthetic rubber-based MP/NPs. Overall, the film-coated $Fe_3O_4$ beads present an innovative approach for eliminating hydrophobic NP pollutants from water. We propose that the vast diversity of available monomers and material-binding peptides offers a versatile and powerful technological foundation to address pressing environmental and human health challenges related to plastic pollution.

### 3.3 MP/NPs detection and quantification in human kidneys

MP/NPs are used in a wide variety of products, such as food packaging, cosmetic containers, and water supply systems. These particles have been detected in numerous environmental and consumer sources, including drinking water, a broad spectrum of food items, cosmetic products, and even the air.[18, 24, 219, 220] Inhalation exposure is particularly concerning, as MP/NPs can bind to fine particulate matter (PM2.5) and be carried over long distances through atmosphere.[15] Given their pervasive presence, MP/NPs can easily enter the human body through ingestion, inhalation, or even dermal contact. This widespread exposure raises increasing concern about their potential health impacts.[221]

MPs, with an average concentration of approximately 1.6 μg/mL, have been detected in human blood using Py-GC/MS. In theory, once present in the bloodstream, MPs can circulate throughout the body via the cardiovascular system, potentially reaching and accumulating in various tissues and organs. Recent studies have confirmed the presence of MPs in the carotid arteries,[32, 33] brains,[30] kidneys,[30] bones,[34] and eyes.[35] Although the detection and quantification of MPs in kidney tissue have been achieved, there remains a lack of research exploring the relationship between MP/NP levels and kidney function. In this study, we addressed this gap by analyzing kidney samples from three groups with different eGFR values using Py-GC/MS to assess MP/NP content. In addition, we employed plastibody-based staining to visualize the MP/NPs within the kidney tissues.

#### 3.3.1 MP/NPs detection and quantification by Py-GC/MS

As described earlier, prior to conducting Py-GC/MS analysis on the kidney samples, specific indicator ions for each target plastic type were selected based on previous identifications and established literature.[18, 19, 69, 73, 193] Since the peptide had no influence in this case, the chosen markers differ slightly from those used in the earlier section.

A summary of the pyrolysis markers selected for each polymer is provided in Table 10. For PMMA, PS, nylon 6, and nylon 66, the indicator compounds and their corresponding ions remained the same as previously reported: methyl methacrylate (m/z 100) for PMMA, styrene trimer (m/z 91) for PS, N-(5-cyanopentyl)hex-5-enamide (m/z 154) for nylon 6, and cyclopentanone (m/z 84) for nylon 66. In the case of PE, 1,20-heneicosadiene (C21, m/z 83) was selected due to its high specificity and sensitivity. For PP, the most suitable marker was identified as 2,4-dimethyl-1-heptene (m/z 83). PET was quantified using vinyl benzoate (m/z 105) as the indicator ion. PVC was also included for analysis, with naphthalene (m/z 128) chosen as its representative marker.

All selected indicator ions exhibited strong linearity in calibration curves within the range of 0.5–2.5 mg $SiO_2$ complex per cup, with correlation coefficients close to 0.99, demonstrating the robustness of the quantification method. The calculated LODs, based on laboratory and procedural blanks, were as follows: 0.134 µg/L for PE, 0.116 µg/L for PP, 0.002 µg/L for PS, 0.036 µg/L for PET, 0.025 µg/L for PMMA, 0.017 µg/L for PVC, 0.003 µg/L for nylon 6, and 0.027 µg/L for nylon 66. These low detection limits confirm the method's capability to reliably quantify nanoplastic mass concentrations in kidney samples. Importantly, the LOD values are in good agreement with those reported in previous studies on MP/NPs detection in human tissues.[32, 33]

**Table 10. Characteristic components and calibration functions of the eight analyzed nanoplastic polymer types.**

| Polymer | Indicator compound | Indicator ions (m/z) | Calibration functions | Linearity ($R^2$) | LOD (ng) | LOQ (ng) |
|---|---|---|---|---|---|---|
| PE | 1,20-Heneicosadiene (C21) | 83 | y=12344.728x-4159.106 | 0.997 | 134.26 | 447.53 |
| PP | 2,4,6-Dimethyl-1-heptene | 83 | y=37492.853x-7141.98 | 0.984 | 115.65 | 385.50 |
| PS | Styrene trimer | 91 | y=878400.878x-5957.764 | 0.988 | 2.48 | 8.27 |
| PET | Vinyl benzoate | 105 | y=33381.936x+6562.767 | 0.995 | 36.15 | 120.50 |
| PMMA | Methyl methacrylate | 100 | y=74196.662x-6447.105 | 0.999 | 25.01 | 83.38 |
| PVC | Naphthalene | 128 | y=60136.721x+9332.386 | 0.993 | 16.78 | 55.93 |
| Nylon 6 | *N*-(5-cyanopentyl)hex-5-enamide | 154 | y=145422.536x+4788.591 | 0.994 | 2.75 | 9.17 |
| Nylon 66 | Cyclopentanone | 84 | y=21086.104x+17.163 | 0.995 | 26.85 | 89.50 |

A total of 139 patients were categorized into three groups according to their eGFRs: <59 mL/min, 60–89 mL/min, and >90 mL/min. These ranges represent varying degrees of kidney function, with higher eGFR values indicating better renal performance. This classification was used to investigate the relationship between MP/NP concentrations and kidney function.

The concentration of MP/NPs in each kidney sample was determined by normalizing the detected MP/NP mass to the sample weight. As illustrated in Figure 75, MP/NPs were present in all analyzed kidney samples. Patients with an eGFR below 59 mL/min exhibited the highest MP/NP burden, averaging $49.3 \pm 39.3$ µg/mg. In the 60–89 mL/min group, the average concentration was $31.2 \pm 23.7$ µg/mg, while those with eGFR above 90 mL/min showed the

lowest levels, at 12.1 ± 6.2 µg/mg. Statistically significant differences were observed between adjacent eGFR groups ($P < 0.01$) and between the lowest and highest eGFR groups ($P < 0.001$).

These findings indicate a strong inverse correlation between MP/NP accumulation and kidney function, suggesting that higher MP/NP exposure may be associated with impaired renal performance. Notably, the concentrations detected in kidney tissue were substantially higher than those previously reported in other human samples, including three types of human arteries (such as coronary artery, carotid artery, and aorta; 118.66 ± 53.87 µg/g),[32] carotid artery plaques (e.g., 21.7 ± 53.87 µg/mg for PE),[33] and blood (1.6 ± 2.3 µg/mL),[39] all quantified via Py-GC/MS. This elevated accumulation in the kidney was likely due to its role as a biological filtration organ, resulting in the retention and buildup of plastic particles over time.

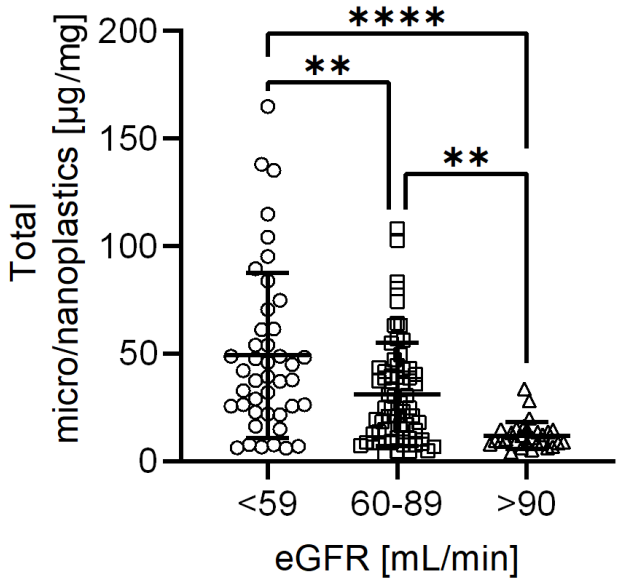


**Figure 75. MP/NPs concentration in human kidneys.** The kidney samples were divided into three groups, categorized by GFR values. The group of lower eGFR shows higher MP/NPs amounts.

Linear regression analysis was conducted to assess the relationship between MP/NP burden and eGFR values across the 139 patient samples (Figure 76). The results revealed a statistically significant inverse correlation: as eGFR increased, the amounts of detected MP/NPs decreased. This relationship was supported by a p-value of 0.003326, indicating a meaningful association between reduced MP/NP accumulation and better kidney function.

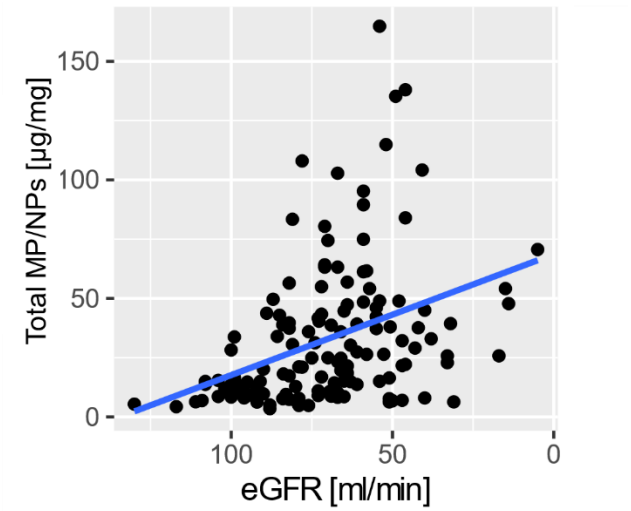


**Figure 76. Linear regression model between total MP/NPs amounts and eGFR.** MP/NPs amounts correlate well to the eGFR values, indicating MP/NPs might cause kidney dysfunction.

As illustrated in Figure 77, eight different types of MP/NPs were identified in the kidney samples. Among these, PE was the most prevalent, accounting for 38–68% of the total MP/NP content, followed by PP at 10–27%, nylon 66 at 11–18%, and nylon 6 at 5–7%. Prior study investigating MPs in kidneys and carotid artery plaques also reported PE as the most abundant polymer, aligning with the findings from our study and suggesting that PE may be the most dominant MP type in human organs.[30, 33] However, current studies detected only nylon 66, PE, PET, and PVC in arterial samples, while PP, nylon 6, PMMA, and PS, found in kidney tissue, were absent.[32, 33] This discrepancy could be attributed to individual variations in MP/NP exposure sources and patterns, as well as the kidney's role as a filtration organ, which may promote greater accumulation of diverse MP/NP types compared to other tissues.

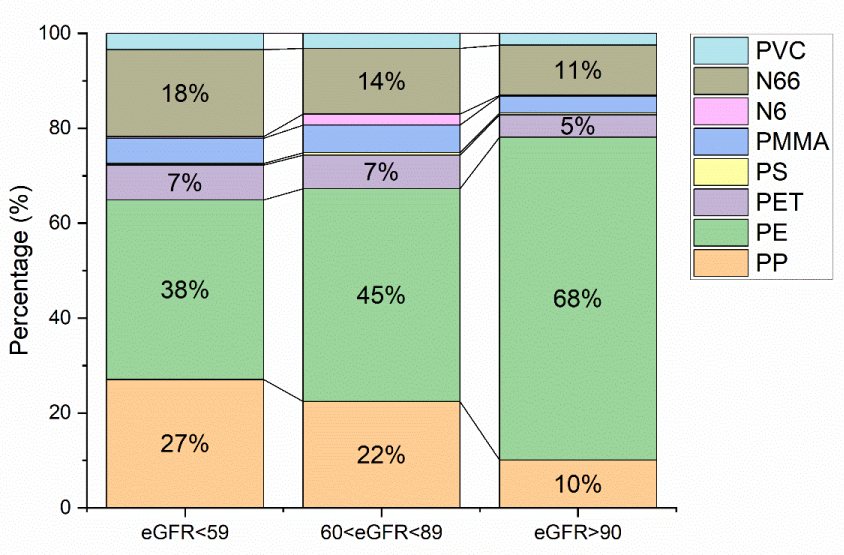


**Figure 77. Polymer types in three groups of kidney samples.** Eight types of MP/NPs are identified in the kidney samples, with PE, PP, and Nylon 66 as the most dominant plastic types.

Previous studies have already reported an association between the presence of MP/NPs in carotid artery plaques and the incidence of cardiovascular disease.[33] In addition to those findings, our study revealed a correlation between the quantity of MP/NPs and kidney function. However, it is important to note that these observed relationships are correlational and do not establish a direct causal link.

### 3.3.2 MPs detection by Plastibody

As demonstrated in the previous section through Py-GC/MS analysis, eight types of MP/NPs were identified and quantified in human kidney tissues. To visualize these plastic particles within the tissue, specific fluorescent staining is required. While Nile red is commonly used for staining plastics, it also binds to cellular lipids, resulting in high background fluorescence and reduced specificity.[222]

To overcome this limitation, we employed the "plastibody",[58] a material-binding peptide-based probe specifically developed for plastic staining, to label MP/NPs in kidney samples. In parallel, DAPI staining was used to label cell nuclei, providing structural context and aiding in the identification of kidney features such as glomeruli and tubules. As shown in Figure 78, MP/NPs labeled by the plastibody appear red under fluorescence microscopy and are notably concentrated in the glomerular region. While this suggests accumulation of MP/NPs in specific kidney structures, further validation of the plastibody's specificity for MP/NPs is necessary. Based on current knowledge, the red fluorescence observed is unlikely to originate from kidney stones, as it is commonly seen within the tubules where kidney stones typically form.

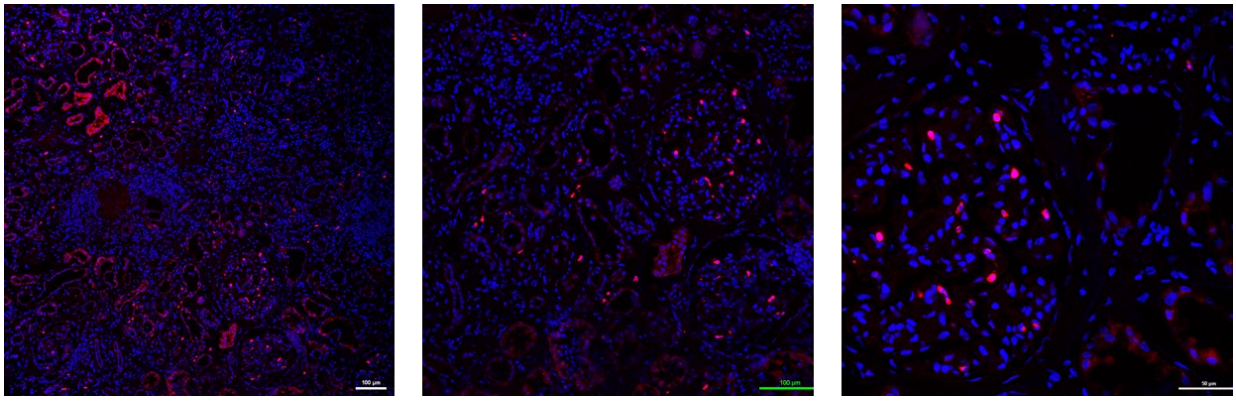

**Figure 78. Fluorescence images showing the Plastibody and DAPI-stained human kidney.** MP/NPs in kidney tissue are dyed by the Plastibody and show red fluorescence, but the results require further confirmation by other techniques.

In this study, we successfully detected and quantified MP/NPs in human kidney tissue using Py-GC/MS. Additionally, these particles were visualized within the kidney using plastibody-based fluorescent staining. A correlation was observed between the levels of MP/NPs in kidney

samples and kidney function, suggesting a potential link. However, further research is necessary to determine whether MP/NPs play a causal role in the development or progression of kidney disease.

# 4 Lessons learned from MBP-assisted enrichment, detection, and quantification of MP/NPs

In a circular polymer economy, all polymeric materials are expected to be either biodegradable or recyclable.[3] As a result, a strong increase in the release of MP/NPs into the environment can be expected. Detecting and quantifying these small particles in high throughput, particularly those under 5 mm, remains a significant analytical challenge, as recognized by the EU Commission, and hampers the development of effective regulatory policies.[52, 53] MP/NPs are widespread in aquatic ecosystems and often present at low concentrations, making their detection and analysis particularly difficult. The latter is urgent due to the rapid circular polymer economy development, which underscores the need for efficient enrichment methods and sensitive analytical tools to assess both environmental contamination and potential health risks.

Accordingly, this thesis addresses these challenges by developing and applying MP/NP-enrichment platforms based on MBP-capture, termed MagNanoTrap and Hooked for Decay. When combined with Py-GC/MS, MagNanoTrap, in particular, enables reliable detection and quantification of MP/NPs, even in complex environmental water matrices at environmental concentrations. Furthermore, this analytic methodology was successfully extended to biological samples, providing first insights into possible correlations between MP/NP accumulation and human health effects.

In the **MagNanoTrap system**, the peptide LCI was selected due to its strong affinity for iron oxide ($Fe_3O_4$) surfaces. LCI decoration of iron oxide nanoparticles introduces desired chemicals or physical functionalities.[54] In the MagNanoTrap application, LCI was fused with the plastic-binding peptide MBP1 through a rigid linker, known as Domain Z, to generate a custom-designed bifunctional peptide. Domain Z is composed of three parallel alpha helices, providing a symmetrical and spatially separated display of both peptides, which ensures that each retains its independent functionality.[223] MBP1 is a 33-amino acid peptide enriched with arginine, which accounts for roughly one-third of its sequence.[147] Previous studies in MBP engineering have demonstrated that positively charged residues, particularly arginine and lysine, play a key role in enhancing binding strength to plastic surfaces like PP,[148] PET,[142] and polyamides.[142] Therefore, the high abundance of these residues in MBP1 is expected to underlie its strong and broad-spectrum binding capability, making it a valuable component for the development of versatile platforms for capturing plastic particles.

MBP-based binding occurs rapidly, typically within minutes, under ambient aqueous conditions and remains effective even after exposure to high temperatures (e.g., 60 °C), making the system user-friendly and efficient.[132, 142] The detergent-resistant nature of the binding allows it to function even in the presence of residual $H_2O_2$, which is commonly used to oxidize and eliminate organic contaminants in environmental water.[19, 69] This makes the system well-suited for direct enrichment after such pretreatment steps that remove biofilms without requiring additional cleanup.

Kinetic and isothermal adsorption studies showed that the enrichment process follows the Hofmeister series, indicating that the primary mechanism is a salting-out-induced hydrophobic interaction effect. Salt ions interfere with water's interactions with charged groups on both the MagNanoTrap and the plastic particles, reducing the hydration shell and exposing hydrophobic regions.[190] As a result, increasing salt concentrations accelerate and enhance MP/NP capture. This salting-out makes the system highly applicable to most environmental water bodies, including rivers, lakes, seawater, and wastewater, since salt can be easily supplemented to any sample.

Py-GC/MS results confirmed that the MBP peptides bound to the plastic particles after enrichment do not interfere with the identification of plastic-specific indicator ions. This ensures the reliable and versatile quantification of a wide range of plastics. Although one liter of environmental water is typically used for enrichment, the system is sensitive enough to detect key plastics like PE and PS from volumes as small as 50 mL, with detection limits of 58 ng and 60 ng, respectively. In treated wastewater, even after ultrafiltration, residual NPs smaller than the membrane pore size were still detected at concentrations of 1.35 µg/L. These smaller particles pose greater risks due to their higher surface-to-volume ratios, which make them more prone to adsorbing toxic substances.[27] Furthermore, such NPs may be small enough to cross biological barriers, including the blood-brain barrier, highlighting their potential health risks.[37, 38] This thesis also showed that lakes with higher levels of human activity, for example, water retrieved from a park lake, contained significantly more MP/NPs than those with minimal human interference, as shown in the plastics quantification of the lake from a natural reservoir, underlining the impact of anthropogenic activities on plastic pollution. Additionally, because iron oxide is acid-digestible, captured particles can be recovered and imaged using SEM. This compensates for the loss of size and shape information that typically occurs during pyrolysis in plastics analysis.

The MagNanoTrap enrichment system was successfully developed for the detection and quantification of NPs in environmental water samples. However, degradation of these particles could be an effective process to ensure environmental and human health. To address this, the **Hooked and Decay platform** was established, leveraging the dual functionality of the GH catalyst to both capture and disintegrate NPs. This system relies on ROMP reaction to generate a hydrophobic polymer film that attracts MP/NPs, while also enabling the degradation of SBR NPs through the ethenolysis process.

Built on the same principle of iron oxide functionalization, the system employs a variant of the MBP LCI, termed LCI_F16C, which introduces a free thiol group for site-specific conjugation via click chemistry to maleimide-functionalized GH-cofactors. This design allows precise anchoring of catalytically active GH groups onto the SPION surface. These cofactors initiate ROMP using a water-insoluble norbornene derivative (Nor-C18) to form a robust hydrophobic polynorbornene shell. This outer layer enhances MP/NP capture via hydrophobic interactions. In contrast, a water-soluble monomer would yield a less stable polymer, compromising the particle-capturing ability of the coating. The enrichment performance is also influenced by the ROMP reaction time. Insufficient reaction time leads to incomplete polymer coating on $Fe_3O_4$ nanoparticles, resulting in poor adsorption. Conversely, prolonged reaction times can cause nanoparticle aggregation, which also diminishes adsorption capacity. Additionally, the linker connecting the GH-cofactor to LCI_F16C is crucial for catalytic efficiency. A shorter linker positions the metal catalyst closer to the surrounding amino acid residues, optimizing the microenvironment for the ROMP reaction and thereby enhancing polymer formation.[224] The capture behavior of the hydrophobic shell parallels that of the MagNanoTrap system, showing similarly high adsorption capacity for PS NPs. The addition of salt ions further accelerates binding, and the observed enrichment trends align with the Hofmeister series, underscoring hydrophobic interactions as the primary driving force behind the adsorption mechanism.

Importantly, the GH-cofactor retains its catalytic activity even after encapsulation, protected within the polymer shell. After capturing SBR NPs, exposure to organic solvents dissolves the film, enabling the cofactor to access internal carbon–carbon double bonds in the SBR polymer. In the presence of ethylene, this triggers selective ethenolysis, initiating polymer degradation. This demonstrates a promising strategy for not only capturing but also controllably breaking down persistent plastic pollutants.

The potential **impact of MP/NPs on kidney health** (cooperation with Uniklinik RWTH Aachen) was investigated by examining their association with kidney dysfunction. To detect

and quantify MP/NPs in human kidney tissues, samples are first pretreated with 68% nitric acid to remove organic matter that could interfere with Py-GC/MS analysis.[32, 182-184] A significant inverse correlation was observed between the kidney health, measured by eGFR, and the detected plastic amount. Patients with impaired kidney function (eGFR < 59) exhibited markedly higher MP/NP loads, with plastics comprising up to 10% of kidney tissue weight in some cases. These findings raise two possible scenarios: MP/NPs may contribute directly to kidney damage, or reduced filtration capacity in dysfunctional kidneys may lead to the accumulation of MP/NPs. To further investigate causality, additional analyses of inflammation-related gene expression are underway to determine whether MP/NP exposure is linked to molecular markers of kidney impairment. For visualization, a plastibody, comprising the plastic-binding peptide LCI conjugated with an Alexa Fluor dye, was used to stain MP/NPs in kidney sections.[58] This targeted approach offers greater specificity than conventional dyes like Nile Red, which bind broadly to hydrophobic substances. While the plastibody method shows promise for selective imaging of plastic particles, further validation is needed to confirm that the observed fluorescence is exclusive to MP/NPs but not other hydrophobic residues.

In conclusion, "Material-binding peptides empowering MP/NPs enrichment, detection, and quantification" presents a comprehensive and innovative approach to addressing the growing concerns surrounding MP/NPs pollution in both environmental and biological systems. By developing two distinct platforms, MagNanoTrap for effective NPs enrichment, detection, and quantification, and Hooked and Decay for NPs capture and degradation, this work not only advances analytical capabilities but also introduces practical tools for mitigating plastic contamination. The ability to capture and analyze trace amounts of MP/NPs in complex matrices such as environmental water and human tissue provides critical insights into pollution levels and potential health impacts, particularly concerning kidney function. Moreover, the modular design of the peptide-based enrichment and catalytic systems allows for adaptation across various types of plastic pollutants and sample conditions. As such, these platforms hold significant potential for broader environmental monitoring, public health research, and the development of next-generation remediation strategies. Ultimately, the findings of this thesis contribute valuable knowledge and methodologies to support regulatory efforts, guide policy decisions, and promote sustainable practices in a circular polymer economy.

# 5 Summary and conclusions

Managing MP/NP contamination in aquatic environments is important, as the degradation of synthetic polymers within a circular polymer economy inevitably leads to the formation and widespread release of MP/NPs.[3] The European Commission has identified the analytical gap as a major obstacle to regulating MP/NP contamination, highlighting the urgent need for robust and universal enrichment and monitoring platforms.[52, 53]

The **MagNanoTrap**, a biofunctionalized magnetic nanoparticle system based on SPIONs functionalized with a bifunctional peptide (LCI-DZ-MBP1), contributes to these aspects by enabling efficient enrichment of diverse NPs. When coupled with Py-GC/MS, it allows reliable detection and quantification of NPs in environmental samples with volumes of only 1 liter. In detail, peptide LCI binds SPIONs, while peptide MBP1 targets major plastic types, including PP, PE, PS, and PET. In spiked microliter-scale assays, MagNanoTrap achieved >96% recovery of PS NPs within 10 minutes of shaking, with an adsorption capacity of 3.95 ± 0.14 g/g at 200 mM NaCl. The adsorption mechanism is driven by salt-enhanced hydrophobic interactions. Salt ions interfere with the hydration shell by competing with water molecules bound to the charged surfaces of both the peptide and the NPs. This weakens the hydration layer and enhances exposure of hydrophobic regions, accelerating the binding process.[190] Higher salt concentrations not only increase reaction speed but also improve binding affinity, making the system suitable even in saline environments such as seawater. Notably, the presence of heavy metals did not compromise the system's enrichment performance for PS NPs, supporting its applicability in heavy metal-contaminated waters, such as wastewater. The above-mentioned results demonstrate the broad applicability of the MagNanoTrap platform, which can be employed across various natural aquatic environments, including lakes, rivers, wastewater, and seawater, since NaCl can be readily supplemented when needed.

MagNanoTrap is also compatible with Py-GC/MS analysis, as the peptides do not interfere with key plastic-specific indicator compounds across eight polymers (PP, PE, PET, PS, PMMA, PC, Nylon 6, Nylon 66). In 1 L spiked environmental samples (river, lake, seawater, wastewater), recovery rates ranged from 51.9% to 60.6%, compared to 65.1 ± 2.9% in deionized water, demonstrating robustness across complex water matrices. Detected environmental NP levels were high in human-impacted sites, e.g., park lake (8.60 µg/L) compared to a natural reservoir (2.61 µg/L), and declined significantly with advanced wastewater treatment (ultrafiltration removed ~90% of NPs). Predominant NP types were PP,

PE, and Nylon 6,6, accounting for over 75% of the total plastic load. SEM imaging confirmed the presence of nanosized fibers, flakes, and spheres, particularly in post-treatment wastewater.

Current remediation technologies for removing MP/NPs include flotation systems utilizing bubble–particle interactions,[80, 81] membrane-based methods exploiting membrane cutoffs,[18, 19, 69, 73, 78] and surface-functionalized materials relying on adsorption.[189, 225-227] Most reported approaches achieve removal efficiencies above 80%, mainly for spiked PS and PMMA NPs, with adsorption capacities such as 444.6 ± 22.3 mg/g for biomass fibrous foam[189] and 0.69 ± 0.26 g/g for SPIONs-PAC.[105] In comparison, the MagNanoTrap platform, featuring SPIONs functionalized with bifunctional peptides, exhibited superior performance, achieving over 96% PS NP recovery within 13 minutes of shaking and an adsorption capacity of 3.95 ± 0.14 g/g at 200 mM NaCl. Despite this, only membrane-based techniques have been reported as generally applicable for MP/NP monitoring in environmental waters. These systems, cross-flow (50 L samples)[18, 73] and dead-end (1 L samples),[19, 69] typically use polyethersulfone (PES) membranes with a 0.01 µm cutoff, coupled with Py-GC/MS for quantifying mixed plastics such as PP, PE, PS, PET, PMMA, PC, Nylon 6, and Nylon 66, achieving recoveries above 50%. In comparison, the MagNanoTrap combined with Py-GC/MS achieved similar recoveries exceeding 60%, while capturing NPs of all sizes and types from various environmental water samples, making it a promising, universally applicable analytical tool for monitoring NP contamination, supporting circular polymer economy initiatives, and advancing SDG 6 goals for clean water and sanitation.[228]

In a separate approach, a bifunctional "**Hooked for Decay**" system was developed, incorporating a hydrophobic coating on $Fe_3O_4$ beads using a biohybrid catalyst. A variant peptide, LCI_F16C, facilitated the immobilization of a Grubbs-Hoveyda catalyst onto SPIONs via click chemistry. This construct catalyzed the ROMP of a norbornene derivative (Nor-C18), forming a hydrophobic polynorbornene coating. This hydrophobic layer enabled efficient capture of a broad spectrum of plastic NPs, including PP, PE, PS, PET, PMMA, and SBR. The film-coated SPIONs achieved a high adsorption capacity of 5.53 ± 0.29 g/g for PS-COOH NPs (500 nm) within 10 minutes and reached 99% recovery in 100 mM NaCl, driven by hydrophobic interactions.

Moreover, the retained catalytic activity of the embedded GH-cofactor enabled the chemical degradation of captured SBR NPs via internal cleavage of C=C bonds within 1,4-addition butadiene units, in the presence of ethylene, without any additional catalyst. This process

achieved a 6.5% degradation in organic solvent, demonstrating the potential not only for capturing but also initiating the breakdown of persistent synthetic rubber contaminants.

Compared to existing MP/NP removal technologies described above, the “Hooked for Decay” system, based on SPIONs coated with a hydrophobic nanofilm, achieved exceptional performance, recovering over 99% of PS NPs within 10 minutes of shaking and exhibiting an adsorption capacity of 5.53 ± 0.29 g/g at 200 mM NaCl. In addition to NP capture, the film-coated SPIONs also enable the degradation of plastics with internal C=C bonds, such as SBR, introducing a new concept for the removal and disintegration of NP contaminants from aqueous solutions.

Moving from aqueous systems to biological tissues requires specialized pretreatment to remove interference from organic matter; accordingly, a robust protocol was established for the quantification of **MP/NPs in human kidney** samples. To assess human exposure, 139 human kidney tissue samples stratified by eGFR using Py-GC/MS were analyzed. Plastics, including PP, PE, PS, PET, PMMA, PVC, Nylon 6, and Nylon 66, were detected in all groups. The average plastic loads were 49.3 ± 39.3 μg/mg for individuals with eGFR <59 mL/min, 31.2 ± 23.7 μg/mg for those with eGFR 60–89 mL/min, and 12.1 ± 6.2 μg/mg for eGFR >90 mL/min. Dominant plastic types, including PE, PP, and Nylon 66, mirrored the profiles seen in environmental samples. A significant inverse correlation was observed between plastic content and kidney function, suggesting a potential relationship between plastic accumulation and kidney health. Plastibody-based immunostaining further confirmed the localization and accumulation of MP/NPs in kidney glomeruli.

Overall, the combination of bifunctional peptides, either fused with other peptides (MagNanoTrap) or conjugated to catalysts (Hooked for Decay), and SPIONs represents a versatile and modular platform for MP/NPs enrichment. Especially, the MagNanoTrap system holds promise for monitoring plastic contamination in various contexts, including factory effluents, food products, and clinical samples. Furthermore, the correlation between MP/NP accumulation and kidney function was also explored, offering insight into possible health implications. In summary, this work presents a comprehensive, interdisciplinary approach that integrates materials engineering, environmental science, and biomedical assessment to advance the capture, quantification, degradation, and biological evaluation of MP/NPs, providing critical tools for environmental monitoring and human health risk assessment in the context of escalating plastic pollution.

## References


1. D. Crespy, M. Bozonnet and M. Meier, *Angew. Chem., Int. Ed.*, 2008, **47**, 3322-3328.
2. L. Lebreton and A. L. Andrady, *Palgrave Communications*, 2019, **5**, 1-11.
3. L. T. J. Korley, T. H. Epps, B. A. Helms and A. J. Ryan, *Science*, 2021, **373**, 66-69.
4. S. B. Borrelle, J. Ringma, K. L. Law, C. C. Monnahan, L. Lebreton, A. McGivern, E. Murphy, J. Jambeck, G. H. Leonard, M. A. Hilleary, M. Eriksen, H. P. Possingham, H. De Frond, L. R. Gerber, B. Polidoro, A. Tahir, M. Bernard, N. Mallos, M. Barnes and C. M. Rochman, *Science*, 2020, **369**, 1515-1518.
5. A. S. Pottinger, R. Geyer, N. Biyani, C. C. Martinez, N. Nathan, M. R. Morse, C. Liu, S. Hu, M. de Bruyn, C. Boettiger, E. Baker and D. J. McCauley, *Science*, 2024, **386**, 1168-1173.
6. R. C. Thompson, W. Courtene-Jones, J. Boucher, S. Pahl, K. Raubenheimer and A. A. Koelmans, *Science*, 2024, **386**, eadl2746.
7. T. Yang, J. Luo and B. Nowack, *Environ. Sci. Technol.*, 2021, **55**, 15873-15881.
8. T. Yang, Y. Xu, G. Liu and B. Nowack, *Nat. Water*, 2024, **2**, 151-160.
9. D. M. Mitrano, P. Wick and B. Nowack, *Nat. Nanotechnol.*, 2021, **16**, 491-500.
10. H. P. H. Arp, D. Kühnel, C. Rummel, M. MacLeod, A. Potthoff, S. Reichelt, E. Rojo-Nieto, M. Schmitt-Jansen, J. Sonnenberg, E. Toorman and A. Jahnke, *Environ. Sci. Technol.*, 2021, **55**, 7246-7255.
11. M. MacLeod, H. P. H. Arp, M. B. Tekman and A. Jahnke, *Science*, 2021, **373**, 61-65.
12. D. Mennekes and B. Nowack, *Nat. Water*, 2023, **1**, 523-533.
13. M. Strokal, P. Vriend, M. P. Bak, C. Kroeze, J. van Wijnen and T. van Emmerik, *Nat. Commun.*, 2023, **14**, 4842.
14. V. Nava, S. Chandra, J. Aherne, M. B. Alfonso, A. M. Antão-Geraldes, K. Attermeyer, R. Bao, M. Bartrons, S. A. Berger, M. Biernaczyk, R. Bissen, J. D. Brookes, D. Brown, M. Cañedo-Argüelles, M. Canle, C. Capelli, R. Carballeira, J. L. Cereijo, S. Chawchai, S. T. Christensen, K. S. Christoffersen, E. de Eyto, J. Delgado, T. N. Dornan, J. P. Doubek, J. Dusaucy, O. Erina, Z. Ersoy, H. Feuchtmayr, M. L. Frezzotti, S. Galafassi, D. Gateuille, V. Gonçalves, H.-P. Grossart, D. P. Hamilton, T. D. Harris, K. Kangur, G. B. Kankılıç, R. Kessler, C. Kiel, E. M. Krynak, À. Leiva-Presa, F. Lepori, M. G. Matias, S.-i. S. Matsuzaki, Y. McElarney, B. Messyasz, M. Mitchell, M. C. Mlambo, S. N. Motitsoe, S. Nandini, V. Orlandi, C. Owens, D. Özkundakci, S. Pinnow, A. Pociecha, P. M. Raposeiro, E.-I. Rõõm, F. Rotta, N. Salmaso, S. S. S. Sarma, D. Sartirana, F. Scordo, C. Sibomana, D. Siewert, K. Stepanowska, Ü. N. Tavşanoğlu, M. Tereshina, J. Thompson, M. Tolotti, A. Valois, P. Verburg, B. Welsh, B. Wesolek, G. A. Weyhenmeyer, N. Wu, E. Zawisza, L. Zink and B. Leoni, *Nature*, 2023, **619**, 317-322.
15. R. Akhbarizadeh, S. Dobaradaran, M. Amouei Torkmahalleh, R. Saeedi, R. Aibaghi and F. Faraji Ghasemi, *Environ. Res.*, 2021, **192**, 110339.
16. R. Bartnick, A. Rodionov, S. D. J. Oster, M. G. J. Löder and E. Lehndorff, *Environ. Sci. Technol.*, 2024, **58**, 13047-13055.

17. X. Xu, T. Li, J. Zhen, Y. Jiang, X. Nie, Y. Wang, X.-Z. Yuan, H. Mao, X. Wang, L. Xue and J. Chen, *Environ. Sci. Technol. Lett.*, 2024, **11**, 16-22.

18. Y. Xu, Q. Ou, M. Jiao, G. Liu and J. P. van der Hoek, *Environ. Sci. Technol.*, 2022, **56**, 4988-4997.

19. E. D. Okoffo and K. V. Thomas, *J. Hazard. Mater.*, 2024, **464**, 133013.

20. C. Leistenschneider, P. Burkhardt-Holm, T. Mani, S. Primpke, H. Taubner and G. Gerdts, *Environ. Sci. Technol.*, 2021, **55**, 15900-15911.

21. P. Chen, I. A. Kane, M. A. Clare, E. L. Soutter, F. Mienis, R. A. Wogelius and E. Keavney, *Environ. Sci. Technol.*, 2025, **59**, 7278-7287.

22. M. E. Schiano, L. J. D'Auria, R. D'Auria, S. Seccia, G. Rofrano, D. Signorelli, D. Sansone, E. Caprio, S. Albrizio and M. Cocca, *Sci. Total Environ.*, 2024, **948**, 174698.

23. N. Qian, X. Gao, X. Lang, H. Deng, T. M. Bratu, Q. Chen, P. Stapleton, B. Yan and W. Min, *P. Natl. Acad. Sci. USA*, 2024, **121**, e2300582121.

24. D. Li, Y. Shi, L. Yang, L. Xiao, D. K. Kehoe, Y. K. Gun'ko, J. J. Boland and J. J. Wang, *Nat. Food*, 2020, **1**, 746-754.

25. L. M. Hernandez, E. G. Xu, H. C. E. Larsson, R. Tahara, V. B. Maisuria and N. Tufenkji, *Environ. Sci. Technol.*, 2019, **53**, 12300-12310.

26. J. Gigault, H. El Hadri, B. Nguyen, B. Grassl, L. Rowenczyk, N. Tufenkji, S. Feng and M. Wiesner, *Nat. Nanotechnol.*, 2021, **16**, 501-507.

27. N. Sun, H. Shi, X. Li, C. Gao and R. Liu, *Environ. Int.*, 2023, **171**, 107711.

28. L. Shang, K. Nienhaus and G. U. Nienhaus, *J. Nanobiotechnology*, 2014, **12**, 5.

29. F. Abdolahpur Monikh, Š. Lehtonen, J. Kekäläinen, I. Karkossa, S. Auriola, K. Schubert, A. Zanut, S. Peltonen, J. Niskanen, M. Bandekar, M. von Bergen, J. T. T. Leskinen, A. Koistinen, S. Bogialli, Z. Guo, J. V. K. Kukkonen, C. Chen and I. Lynch, *Nano Today*, 2024, **59**, 102466.

30. A. J. Nihart, M. A. Garcia, E. El Hayek, R. Liu, M. Olewine, J. D. Kingston, E. F. Castillo, R. R. Gullapalli, T. Howard, B. Bleske, J. Scott, J. Gonzalez-Estrella, J. M. Gross, M. Spilde, N. L. Adolphi, D. F. Gallego, H. S. Jarrell, G. Dvorscak, M. E. Zuluaga-Ruiz, A. B. West and M. J. Campen, *Nat. Med.*, 2025, DOI: 10.1038/s41591-024-03453-1.

31. S. Huang, X. Huang, R. Bi, Q. Guo, X. Yu, Q. Zeng, Z. Huang, T. Liu, H. Wu, Y. Chen, J. Xu, Y. Wu and P. Guo, *Environ. Sci. Technol.*, 2022, **56**, 2476-2486.

32. S. Liu, C. Wang, Y. Yang, Z. Du, L. Li, M. Zhang, S. Ni, Z. Yue, K. Yang, Y. Wang, X. Li, Y. Yang, Y. Qin, J. Li, Y. Yang and M. Zhang, *J. Hazard. Mater.*, 2024, **469**, 133855.

33. R. Marfella, F. Prattichizzo, C. Sardu, G. Fulgenzi, L. Graciotti, T. Spadoni, N. D'Onofrio, L. Scisciola, R. L. Grotta, C. Frigé, V. Pellegrini, M. Municinò, M. Siniscalchi, F. Spinetti, G. Vigliotti, C. Vecchione, A. Carrizzo, G. Accarino, A. Squillante, G. Spaziano, D. Mirra, R. Esposito, S. Altieri, G. Falco, A. Fenti, S. Galoppo, S. Canzano, F. C. Sasso, G. Matacchione, F. Olivieri, F. Ferraraccio, I. Panarese, P. Paolisso, E. Barbato, C. Lubritto, M. L. Balestrieri, C. Mauro, A. E. Caballero, S. Rajagopalan, A. Ceriello, B. D'Agostino, P. Iovino and G. Paolisso, *N. Engl. J. Med.*, 2024, **390**, 900-910.

34. Q. Yang, Y. Peng, X. Wu, X. Cao, P. Zhang, Z. Liang, J. Zhang, Y. Zhang, P. Gao, Y. Fu, P. Liu, Z. Cao and T. Ding, *Environ. Int.*, 2025, **196**, 109316.

35. Y. Zhong, Y. Yang, L. Zhang, D. Ma, K. Wen, J. Cai, Z. Cai, C. Wang, X. Chai, J. Zhong, B. Liang, Y. Huang, H. Xian, Z. Li, X. Yang, D. Chen, G. Zhang and Z. Huang, *Sci. Total Environ.*, 2024, **921**, 171109.

36. S. Liu, X. Liu, J. Guo, R. Yang, H. Wang, Y. Sun, B. Chen and R. Dong, *Environ. Sci. Technol.*, 2023, **57**, 17774-17785.

37. Z. Liu, A. Sokratian, A. M. Duda, E. Xu, C. Stanhope, A. Fu, S. Strader, H. Li, Y. Yuan, B. G. Bobay, J. Sipe, K. Bai, I. Lundgaard, N. Liu, B. Hernandez, C. Bowes Rickman, S. E. Miller and A. B. West, *Sci. Adv.*, 2023, **9**, eadi8716.

38. H. Sun, B. Yang, Q. Li, X. Zhu, E. Song, C. Liu, Y. Song and G. Jiang, *Nat. Nanotechnol.*, 2024, **19**, 1354-1365.

39. H. A. Leslie, M. J. M. van Velzen, S. H. Brandsma, A. D. Vethaak, J. J. Garcia-Vallejo and M. H. Lamoree, *Environ. Int.*, 2022, **163**, 107199.

40. Y. Luo, L. Li, Y. Feng, R. Li, J. Yang, W. J. G. M. Peijnenburg and C. Tu, *Nat. Nanotechnol.*, 2022, **17**, 424-431.

41. X.-D. Sun, X.-Z. Yuan, Y. Jia, L.-J. Feng, F.-P. Zhu, S.-S. Dong, J. Liu, X. Kong, H. Tian, J.-L. Duan, Z. Ding, S.-G. Wang and B. Xing, *Nat. Nanotechnol.*, 2020, **15**, 755-760.

42. L. Li, Y. Luo, R. Li, Q. Zhou, W. J. G. M. Peijnenburg, N. Yin, J. Yang, C. Tu and Y. Zhang, *Nat. Sustain.*, 2020, **3**, 929-937.

43. H. Liao, J. Liu, D. Gao, G. Chen, C. Kong, X. Huang and J. Wang, *TrAC-Trend. Anal. Chem*, 2025, **182**, 118061.

44. X.-X. Zhou, S. He, Y. Gao, H.-Y. Chi, D.-J. Wang, Z.-C. Li and B. Yan, *Environ. Sci. Technol.*, 2021, **55**, 3032-3040.

45. N. González-Soto, L. Campos, E. Navarro, E. Bilbao, L. Guilhermino and M. P. Cajaraville, *Sci. Total Environ.*, 2022, **851**, 157999.

46. A. Binelli, C. Della Torre, L. Nigro, N. Riccardi and S. Magni, *Sci. Total Environ.*, 2022, **806**, 150574.

47. I. Martínez-Álvarez, K. Le Menach, M. P. Cajaraville, H. Budzinski and A. Orbea, *Sci. Total Environ.*, 2024, **927**, 172380.

48. C. Halsband, L. Sørensen, F. R. Khan, D. Herzke and S. Wagner, *Front. Environ. Sci.*, 2024, **Volume 11 - 2023**.

49. F. Sommer, V. Dietze, A. Baum, J. Sauer, S. Gilge, C. Maschowski and R. Gieré, *Aerosol Air Qual. Res.*, 2018, **18**, 2014-2028.

50. B. Baensch-Baltruschat, B. Kocher, F. Stock and G. Reifferscheid, *Sci. Total Environ.*, 2020, **733**, 137823.

51. A. Brachner, D. Fragouli, I. F. Duarte, P. M. A. Farias, S. Dembski, M. Ghosh, I. Barisic, D. Zdzieblo, J. Vanoirbeek, P. Schwabl and W. Neuhaus, *International Journal of Environmental Research and Public Health*, 2020, **17**, 8832.

52. P. Alexy, E. Anklam, T. Emans, A. Furfari, F. Galgani, G. Hanke, A. Koelmans, R. Pant, H. Saveyn and B. Sokull Kluettgen, *Food Addit. Contam. Part A*, 2020, **37**, 1-10.

53. J. Allan, S. Belz, A. Hoeveler, M. Hugas, H. Okuda, A. Patri, H. Rauscher, P. Silva, W. Slikker, B. Sokull-Kluettgen, W. Tong and E. Anklam, *Regul. Toxicol. Pharmacol.*, 2021, **122**, 104885.

54. M. Mao, L. Ahrens, J. Luka, F. Contreras, T. Kurkina, M. Bienstein, M. Sária Pereira de Passos, G. Schirinzi, D. Mehn, A. Valsesia, C. Desmet, M.-Á. Serra, D. Gilliland and U. Schwaneberg, *Chem. Soc. Rev.*, 2024, **53**, 6445-6510.

55. K. Kadac-Czapska, P. J. Trzebiatowska, E. Knez, A. Zaleska-Medynska and M. Grembecka, *Food Chem.*, 2023, **418**, 135985.

56. Q. Abbas, M. Zia-ur-Rehman, H. Ullah, M. A. Mujtaba Munir, M. U. Ali, A. Ali, K. Pikon and B. Yousaf, *J. Clean. Prod.*, 2024, **471**, 143454.

57. A. Bianco, L. Carena, N. Peitsaro, F. Sordello, D. Vione and M. Passananti, *Environ. Chem. Lett.*, 2023, **21**, 647-653.

58. W. Bauten, M. Nöth, T. Kurkina, F. Contreras, Y. Ji, C. Desmet, M.-Á. Serra, D. Gilliland and U. Schwaneberg, *Sci. Total Environ.*, 2023, **860**, 160450.

59. Y. Lu, K.-W. Hintzen, T. Kurkina, Y. Ji and U. Schwaneberg, *Adv. Sci.*, 2023, **10**, 2303195.

60. Y. Lu, K.-W. Hintzen, T. Kurkina, Y. Ji and U. Schwaneberg, *ACS Catal.*, 2023, **13**, 12746-12754.

61. N. P. Ivleva, *Chem. Rev.*, 2021, **121**, 11886-11936.

62. W. Pei, R. Hu, H. Liu, L. Wang and Y. Lai, *TrAC-Trend. Anal. Chem*, 2023, **166**, 117188.

63. Y. Chen, D. Wen, J. Pei, Y. Fei, D. Ouyang, H. Zhang and Y. Luo, *Curr. Opin. Environ. Sci. Health*, 2020, **18**, 14-19.

64. K. Hashimoto, V. R. Badarla, A. Kawai and T. Ideguchi, *Nat. Commun.*, 2019, **10**, 4411.

65. B. E. Oßmann, G. Sarau, H. Holtmannspötter, M. Pischetsrieder, S. H. Christiansen and W. Dicke, *Water Res.*, 2018, **141**, 307-316.

66. S. Moon, L. M. A. Martin, S. Kim, Q. Zhang, R. Zhang, W. Xu and T. Luo, *Sci. Adv.*, 2024, **10**, eadh1675.

67. X. Shi, T. Mao, X. Huang, H. Shi, K. Jiang, R. Lan, H. Zhao, J. Ma, J. Zhao and B. Xing, *Nat. Water*, 2025, **3**, 449-460.

68. B. Singh and A. Kumar, *TrAC-Trend. Anal. Chem*, 2024, **170**, 117440.

69. E. D. Okoffo and K. V. Thomas, *Water Res.*, 2024, **254**, 121397.

70. P. Li, Y. Lai, R.-g. Zheng, Q.-c. Li, X. Sheng, S. Yu, Z. Hao, Y.-q. Cai and J. Liu, *Environ. Sci. Technol.*, 2023, **57**, 12010-12018.

71. X.-y. Sheng, Y.-j. Lai, S.-j. Yu, Q.-c. Li, Q.-x. Zhou and J.-f. Liu, *Environ. Sci. Technol.*, 2023, **57**, 10754-10762.

72. Q. Li, Y. Lai, P. Li, X. Liu, Z. Yao, J. Liu and S. Yu, *Environ. Sci. Technol.*, 2022, **56**, 8255-8265.

73. Y. Xu, Q. Ou, X. Wang, F. Hou, P. Li, J. P. van der Hoek and G. Liu, *Environ. Sci. Technol.*, 2023, **57**, 3114-3123.

74. F. Ribeiro, E. D. Okoffo, J. W. O'Brien, S. Fraissinet-Tachet, S. O'Brien, M. Gallen, S. Samanipour, S. Kaserzon, J. F. Mueller, T. Galloway and K. V. Thomas, *Environ. Sci. Technol.*, 2020, **54**, 9408-9417.

75. C. Jeffries, C. Rauert and K. V. Thomas, *ACS Food Sci. Technol.*, 2025, **5**, 1536-1545.

76. S. Mutemi, Z. Hoko and H. Makurira, *Phys. Chem. Earth, Parts A/B/C*, 2020, **117**, 102864.

77. Q. Yang, S. Zhang, J. Su, S. Li, X. Lv, J. Chen, Y. Lai and J. Zhan, *Environ. Sci. Technol.*, 2022, **56**, 10818-10828.

78. M. Jiang, C. Jing, C. Lei, X. Han, Y. Wu, S. Ling, Y. Zhang, Q. Li, H. Yu, S. Liu, J. Li, W. Chen and G. Yu, *Nat. Sustain.*, 2024, **7**, 168-178.

79. S.-H. Na, M.-J. Kim, J.-T. Kim, S. Jeong, S. Lee, J. Chung and E.-J. Kim, *Water Res.*, 2021, **202**, 117417.

80. A. Abdeljaoued, B. L. Ruiz, Y.-E. Tecle, M. Langner, N. Bonakdar, G. Bleyer, P. Stenner and N. Vogel, *Nat. Commun.*, 2024, **15**, 5437.

81. M. Jia, M. U. Farid, Y.-W. Ho, X. Ma, P. W. Wong, T. Nah, Y. He, M. W. Boey, G. Lu, J. K.-H. Fang, J. Fan and A. K. An, *Nat. Commun.*, 2024, **15**, 9079.

82. B. Yang, L. Tian, P. Zhou, P. Babakhani, J. Gregory, N. Graham, M. Elimelech and W. Yu, *Nat. Commun.*, 2025, **16**, 5998.

83. S. Lu, L. Liu, Q. Yang, H. Demissie, R. Jiao, G. An and D. Wang, *Sci. Total Environ.*, 2021, **786**, 147508.

84. Y. Zhang, X. Wang, Y. Li, H. Wang, Y. Shi, Y. Li and Y. Zhang, *J. Hazard. Mater.*, 2022, **425**, 127962.

85. H. Li, M. Tang, J. Wang, L. Dong, L. Wang, Q. Liu, Q. Huang and S. Lu, *Sci. Total Environ.*, 2023, **897**, 165404.

86. Z. Wang, C. Sun, F. Li and L. Chen, *Chem. Eng. J.*, 2021, **415**, 129006.

87. B. Zheng, B. Li, H. Wan, X. Lin and Y. Cai, *J. Hazard. Mater.*, 2022, **431**, 128611.

88. A. Batool and S. Valiyaveettil, *J. Hazard. Mater.*, 2021, **413**, 125301.

89. E. Tiwari, N. Singh, N. Khandelwal, F. A. Monikh and G. K. Darbha, *J. Hazard. Mater.*, 2020, **397**, 122769.

90. H. Zhao, J. Wu, F. Su and X. He, *Hum. Ecol. Risk Assess.*, 2023, **29**, 327-346.

91. S. Shang, Y. Liu, M. Liu, Y. Bai, X. Wang, B. Wu, J. Chen, J. Dong and Y. Liu, *J. Hazard. Mater.*, 2022, **421**, 126796.

92. F. Pasanen, R. O. Fuller and F. Maya, *Chem. Eng. J.*, 2023, **455**, 140405.

93. M. Haris, M. W. Khan, A. Zavabeti, N. Mahmood and N. Eshtiaghi, *Chem. Eng. J.*, 2023, **455**, 140390.

94. Z. Chen, J. Fang, W. Wei, H. H. Ngo, W. Guo and B.-J. Ni, *J. Clean. Prod.*, 2022, **371**, 133676.

95. H. Park, A. May, L. Portilla, H. Dietrich, F. Münch, T. Rejek, M. Sarcletti, L. Banspach, D. Zahn and M. Halik, *Nat. Sustain.*, 2020, **3**, 129-135.

96. M. Sarcletti, D. Vivod, T. Luchs, T. Rejek, L. Portilla, L. Müller, H. Dietrich, A. Hirsch, D. Zahn and M. Halik, *Adv. Funct. Mater.*, 2019, **29**, 1805742.

97. T. Luchs, M. Sarcletti, L. Zeininger, L. Portilla, C. Fischer, S. Harder, M. Halik and A. Hirsch, *Chem. Eur. J.*, 2018, **24**, 13589-13595.

98. H. Gaß, M. Sarcletti, L. Müller, S. Hübner, T. Yokosawa, H. Park, T. Przybilla, E. Spiecker and M. Halik, *Adv. Sci.*, 2023, **10**, 2302495.

99. P. Elumalai, R. Rajamohan, A. Thashbin Vayal Purayil, V. Menon, R. Pranav Srivatsan, A. Santhosh Kumar, S. Lakshminarayanan, S. Mainupriya, S. Nandi, X. Gao, J. Cui and P. Parthipan, *Chem. Eng. J.*, 2024, **497**, 154677.

100. H. Singh, N. Bhardwaj, S. K. Arya and M. Khatri, *Environ. Nanotechnol. Monit. Manag.*, 2020, **14**, 100305.

101. B. I. Kharisov, H. V. R. Dias and O. V. Kharissova, *J. Pet. Sci. Eng.*, 2014, **122**, 705-718.

102. D. Garcia-Osorio, H. P. Nogueira, J. M. Gonçalves, S. H. Toma, S. Garcia-Segura and K. Araki, *Mater. Adv.*, 2021, **2**, 963-973.

103. B. Singh, S. Kumar, B. Kishore and T. N. Narayanan, *Environ. Sci.: Water Res. Technol.*, 2020, **6**, 436-463.

104. M. Zandieh and J. Liu, *Angew. Chem., Int. Ed.*, 2022, **61**, e202212013.

105. M. Sarcletti, H. Park, J. Wirth, S. Englisch, A. Eigen, D. Drobek, D. Vivod, B. Friedrich, R. Tietze, C. Alexiou, D. Zahn, B. Apeleo Zubiri, E. Spiecker and M. Halik, *Mater. Today*, 2021, **48**, 38-46.

106. H. Gaß, T. M. Kloos, A. Höfling, L. Müller, L. Rockmann, D. W. Schubert and M. Halik, *Small*, 2024, **20**, 2305467.

107. A. Misra, C. Zambrzycki, G. Kloker, A. Kotyrba, M. H. Anjass, I. Franco Castillo, S. G. Mitchell, R. Güttel and C. Streb, *Angew. Chem., Int. Ed.*, 2020, **59**, 1601-1605.

108. Y. Tang, S. Zhang, Y. Su, D. Wu, Y. Zhao and B. Xie, *Chem. Eng. J.*, 2021, **406**, 126804.

109. M. Urso, M. Ussia, F. Novotný and M. Pumera, *Nat. Commun.*, 2022, **13**, 3573.

110. M. Urso, M. Ussia, X. Peng, C. M. Oral and M. Pumera, *Nat. Commun.*, 2023, **14**, 6969.

111. W. Li, C. Wu, Z. Xiong, C. Liang, Z. Li, B. Liu, Q. Cao, J. Wang, J. Tang and D. Li, *Sci. Adv.*, 2022, **8**, eade1731.

112. J. Jiménez-Lamana, L. Marigliano, J. Allouche, B. Grassl, J. Szpunar and S. Reynaud, *Anal. Chem.*, 2020, **92**, 11664-11672.

113. X.-x. Zhou, L.-t. Hao, H.-y.-z. Wang, Y.-j. Li and J.-f. Liu, *Anal. Chem.*, 2019, **91**, 1785-1790.

114. Y. Lai, L. Dong, Q. Li, P. Li, Z. Hao, S. Yu and J. Liu, *Environ. Sci. Technol.*, 2021, **55**, 4783-4791.

115. M. Xiao, Y. Yang, H. Alahmadi, A. Harbolic, G. M. Moreno, T. Yu, J. Liu, A. Guo, G. R. Warner, P. A. Stapleton and H. Chen, *J. Hazard. Mater.*, 2025, **493**, 138322.

116. X.-X. Zhou, S. He, Y. Gao, Z.-C. Li, H.-Y. Chi, C.-J. Li, D.-J. Wang and B. Yan, *Anal. Chem.*, 2021, **93**, 6698-6705.

117. M.-L. Mattinen, M. Linder, A. Teleman and A. Annila, *FEBS Letters*, 1997, **407**, 291-296.

118. P. Tomme, A. L. Creagh, D. G. Kilburn and C. A. Haynes, *Biochemistry*, 1996, **35**, 13885-13894.

119. M. A. Goldstein, M. Takagi, S. Hashida, O. Shoseyov, R. H. Doi and I. H. Segel, *Journal of Bacteriology*, 1993, **175**, 5762-5768.

120. K. Morimoto, S. Karita, T. Kimura, K. Sakka and K. Ohmiya, *Journal of bacteriology*, 1997, **179**, 7306-7314.

121. D. W. Cockburn, C. Suh, K. P. Medina, R. M. Duvall, Z. Wawrzak, B. Henrissat and N. M. Koropatkin, *Molecular Microbiology*, 2018, **107**, 249-264.

122. T. Asakura, *Molecules*, 2021, **26**, 3706.

123. K. Kar, S. Ibrar, V. Nanda, T. M. Getz, S. P. Kunapuli and B. Brodsky, *Biochemistry*, 2009, **48**, 7959-7968.

124. C. F. Cruz, N. G. Azoia, T. Matamá and A. Cavaco-Paulo, *International Journal of Biological Macromolecules*, 2017, **101**, 805-814.

125. L. F. Di Costanzo, *Chemistry*, 2022, **4**, 827-847.

126. J. Gautron, L. Stapane, N. Le Roy, Y. Nys, A. B. Rodriguez-Navarro and M. T. Hincke, *BMC Molecular and Cell Biology*, 2021, **22**, 11.

127. N. C. Collins, H. Thordal-Christensen, V. Lipka, S. Bau, E. Kombrink, J.-L. Qiu, R. Hückelhoven, M. Stein, A. Freialdenhoven, S. C. Somerville and P. Schulze-Lefert, *Nature*, 2003, **425**, 973-977.

128. N. Kröger, R. Deutzmann and M. Sumper, *Science*, 1999, **286**, 1129-1132.

129. H. Hashimoto, *Cellular and Molecular Life Sciences CMLS*, 2006, **63**, 2954-2967.

130. H. J. Gilbert, J. P. Knox and A. B. Boraston, *Current Opinion in Structural Biology*, 2013, **23**, 669-677.

131. R. A. Latour, *Colloids and Surfaces B: Biointerfaces*, 2020, **191**, 110992.

132. K. Rübsam, B. Stomps, A. Böker, F. Jakob and U. Schwaneberg, *Polymer*, 2017, **116**, 124-132.

133. A. Yayci, T. Sassmann, A. Boes, F. Jakob, A. Töpel, A. Loreth, C. Rauch, A. Pich and U. Schwaneberg, *Angew. Chem., Int. Ed.*, 2024, **63**, e202319832.

134. S. Braun, G. Dilarri, L. C. de Lencastre Novaes, P. Huth, A. Töpel, L. Hussmann, A. Boes, M. D. da Rocha, F. Jakob, L. O. Regasini, U. Schwaneberg, H. Ferreira and A. Pich, *Adv. Funct. Mater.*, 2024, **34**, 2305646.

135. R. A. Meurer, S. Kemper, S. Knopp, T. Eichert, F. Jakob, H. E. Goldbach, U. Schwaneberg and A. Pich, *Angew. Chem., Int. Ed.*, 2017, **56**, 7380-7386.

136. H. Cui, L. Zhang, D. Söder, X. Tang, M. D. Davari and U. Schwaneberg, *ACS Catal.*, 2021, **11**, 2445-2453.

137. J. P. Palafox-Hernandez, Z. Tang, Z. E. Hughes, Y. Li, M. T. Swihart, P. N. Prasad, T. R. Walsh and M. R. Knecht, *Chem. Mater.*, 2014, **26**, 4960-4969.

138. Z. E. Hughes, M. A. Nguyen, J. Wang, Y. Liu, M. T. Swihart, M. Poloczek, P. I. Frazier, M. R. Knecht and T. R. Walsh, *ACS Nano*, 2021, **15**, 18260-18269.

139. C. Juds, J. Schmidt, M. G. Weller, T. Lange, U. Beck, T. Conrad and H. G. Börner, *J. Am. Chem. Soc.*, 2020, **142**, 10624-10628.

140. D. Wang, A. A. Ingram, J. Luka, M. Mao, L. Ahrens, M. Bienstein, T. P. Spaniol, U. Schwaneberg and J. Okuda, *Angew. Chem., Int. Ed.*, 2024, **63**, e202317419.

141. M. Schadt, N. Herrmann, C. Formen, C. Simons, E. Heine, F. Jakob, U. Schwaneberg and A. Herrmann, *ACS Appl. Eng. Mater.*, 2024, **2**, 2559-2568.

142. N. Herrmann, A. Boes, F. Jakob and U. Schwaneberg, *Prog. Org. Coat.*, 2024, **195**, 108655.

143. Y. Lu, F. Bourdeaux, B. Nian, P. Manimaran, B. Verma, M. Rommerskirchen, S. Bold, L. Zhu, Y. Ji, J. H. Schleifenbaum and U. Schwaneberg, *Chem*, 2025, 102395.

144. S. Dedisch, A. Wiens, M. D. Davari, D. Söder, C. Rodriguez-Emmenegger, F. Jakob and U. Schwaneberg, *Biotechnol. Bioeng.*, 2020, **117**, 49-61.

145. P. Schwinges, S. Pariyar, F. Jakob, M. Rahimi, L. Apitius, M. Hunsche, L. Schmitt, G. Noga, C. Langenbach, U. Schwaneberg and U. Conrath, *Green Chem.*, 2019, **21**, 2316-2325.

146. W. Gong, J. Wang, Z. Chen, B. Xia and G. Lu, *Biochemistry*, 2011, **50**, 3621-3627.

147. J. P. Duvick, T. Rood, A. G. Rao and D. R. Marshak, *J. Biol. Chem.*, 1992, **267**, 18814-18820.

148. K. Rübsam, M. D. Davari, F. Jakob and U. Schwaneberg, *Polymers*, 2018, **10**, 423.

149. Z. Zhang, L. Gao, A. Boes, B. Bajer, J. Stotz, L. Apitius, F. Jakob, E. S. Schneider, E. Sperling, M. Held, T. Emmler, U. Schwaneberg and V. Abetz, *Nat. Commun.*, 2024, **15**, 3308.

150. S. Islam, L. Apitius, F. Jakob and U. Schwaneberg, *Environ. Int.*, 2019, **123**, 428-435.

151. A. R. Grimm, D. F. Sauer, T. Mirzaei Garakani, K. Rübsam, T. Polen, M. D. Davari, F. Jakob, J. Schiffels, J. Okuda and U. Schwaneberg, *Bioconjugate Chem.*, 2019, **30**, 714-720.

152. D. Wang, A. A. Ingram, J. Luka, M. Mao, L. Ahrens, M. Bienstein, T. P. Spaniol, U. Schwaneberg and J. Okuda, *Angew. Chem. Int. Ed.*, 2024, e202317419.

153. L. Witzdam, M. Garay-Sarmiento, M. Gagliardi, Y. L. Meurer, Y. Rutsch, J. Englert, S. Philipsen, A. Janem, R. Alsheghri, F. Jakob, D. G. M. Molin, U. Schwaneberg, N. M. S. van den Akker and C. Rodriguez-Emmenegger, *Macromol. Biosci.*, 2024, **24**, 2300434.

154. M. Garay-Sarmiento, A. Yayci, Y. Rutsch, H. El Kadaoui, S. Apelt, J. Englert, A. Boes, M. Kohse, F. Jakob, T. Bergs, U. Schwaneberg and C. Rodriguez-Emmenegger, *ACS Appl. Mater. Interfaces*, 2025, **17**, 7498-7509.

155. K.-W. Hintzen, C. Simons, K. Schaffrath, G. Roessler, S. Johnen, F. Jakob, P. Walter, U. Schwaneberg and T. Lohmann, *Biomater. Sci.*, 2022, **10**, 3282-3295.

156. M. Garay-Sarmiento, L. Witzdam, M. Vorobii, C. Simons, N. Herrmann, A. de los Santos Pereira, E. Heine, I. El-Awaad, R. Lütticken, F. Jakob, U. Schwaneberg and C. Rodriguez-Emmenegger, *Adv. Funct. Mater.*, 2022, **32**, 2106656.

157. D. Söder, M. Garay-Sarmiento, K. Rahimi, F. Obstals, S. Dedisch, T. Haraszti, M. D. Davari, F. Jakob, C. Heß, U. Schwaneberg and C. Rodriguez-Emmenegger, *Macromol. Biosci.*, 2021, **21**, 2100158.

158. U. T. Bornscheuer, B. Hauer, K. E. Jaeger and U. Schwaneberg, *Angew. Chem., Int. Ed.*, 2019, **58**, 36-40.

159. G. Å. Løset and I. Sandlie, *Methods*, 2012, **58**, 40-46.

160. G. Winter, A. D. Griffiths, R. E. Hawkins and H. R. Hoogenboom, *Annu. Rev. Immunol.*, 1994, **12**, 433-455.

161. J. C. Almagro, M. Pedraza-Escalona, H. I. Arrieta and S. M. Pérez-Tapia, *Antibodies*, 2019, **8**, 44.

162. W. Jaroszewicz, J. Morcinek-Orłowska, K. Pierzynowska, L. Gaffke and G. Węgrzyn, *FEMS Microbiol. Rev.*, 2021, **46**.

163. V. Frappier and A. E. Keating, *Curr. Opin. Struct. Biol.*, 2021, **69**, 63-69.

164. C. M. Clemente, L. Capece and M. A. Martí, *J. Chem. Inf. Model.*, 2023, **63**, 2609-2627.

165. F. H. Arnold, *Angew. Chem., Int. Ed.*, 2018, **57**, 4143-4148.

166. F. Cheng, L. Zhu and U. Schwaneberg, *Chem. Commun.*, 2015, **51**, 9760-9772.

167. J. Yang, A. J. Ruff, M. Arlt and U. Schwaneberg, *Biotechnol. Bioeng.*, 2017, **114**, 1921-1927.

168. K. Rübsam, L. Weber, F. Jakob and U. Schwaneberg, *Biotechnol. Bioeng.*, 2018, **115**, 321-330.

169. K. K. Yang, Z. Wu and F. H. Arnold, *Nat. Methods*, 2019, **16**, 687-694.

170. J. Jumper, R. Evans, A. Pritzel, T. Green, M. Figurnov, O. Ronneberger, K. Tunyasuvunakool, R. Bates, A. Žídek, A. Potapenko, A. Bridgland, C. Meyer, S. A. A. Kohl, A. J. Ballard, A. Cowie, B. Romera-Paredes, S. Nikolov, R. Jain, J. Adler, T. Back, S. Petersen, D. Reiman, E. Clancy, M. Zielinski, M. Steinegger, M. Pacholska, T. Berghammer, S. Bodenstein, D. Silver, O. Vinyals, A. W. Senior, K. Kavukcuoglu, P. Kohli and D. Hassabis, *Nature*, 2021, **596**, 583-589.

171. E. C. Meng, T. D. Goddard, E. F. Pettersen, G. S. Couch, Z. J. Pearson, J. H. Morris and T. E. Ferrin, *Protein Sci.*, 2023, **32**, e4792.

172. Y. Duan, C. Wu, S. Chowdhury, M. C. Lee, G. Xiong, W. Zhang, R. Yang, P. Cieplak, R. Luo, T. Lee, J. Caldwell, J. Wang and P. Kollman, *J. Comput. Chem.*, 2003, **24**, 1999-2012.

173. A. Onoda, K. Fukumoto, M. Arlt, M. Bocola, U. Schwaneberg and T. Hayashi, *Chem. Commun.*, 2012, **48**, 9756-9758.

174. K. Fukumoto, A. Onoda, E. Mizohata, M. Bocola, T. Inoue, U. Schwaneberg and T. Hayashi, *ChemCatChem*, 2014, **6**, 1229-1235.

175. J. Wang, R. M. Wolf, J. W. Caldwell, P. A. Kollman and D. A. Case, *J. Comput. Chem.*, 2004, **25**, 1157-1174.

176. A. Jakalian, D. B. Jack and C. I. Bayly, *J. Comput. Chem.*, 2002, **23**, 1623-1641.

177. S. B. Garber, J. S. Kingsbury, B. L. Gray and A. H. Hoveyda, *J. Am. Chem. Soc.*, 2000, **122**, 8168-8179.

178. F. H. Zokaei, S. Gharavi, E. Asgarani, M. Zarrabi, M. Soudi and Z. Moosavi-nejad, *Biologia*, 2023, **78**, 179-186.

179. K. Vogel, R. Wei, L. Pfaff, D. Breite, H. Al-Fathi, C. Ortmann, I. Estrela-Lopis, T. Venus, A. Schulze, H. Harms, U. T. Bornscheuer and T. Maskow, *Sci. Total Environ.*, 2021, **773**, 145111.

180. J. Wang and X. Guo, *J. Hazard. Mater.*, 2020, **390**, 122156.

181. M. A. Al-Ghouti and D. A. Da'ana, *J. Hazard. Mater.*, 2020, **393**, 122383.

182. Q. Zhao, L. Zhu, J. Weng, Z. Jin, Y. Cao, H. Jiang and Z. Zhang, *Sci. Total Environ.*, 2023, **877**, 162713.

183. S. Liu, J. Guo, X. Liu, R. Yang, H. Wang, Y. Sun, B. Chen and R. Dong, *Sci. Total Environ.*, 2023, **854**, 158699.

184. L. Zhu, J. Zhu, R. Zuo, Q. Xu, Y. Qian and L. An, *Sci. Total Environ.*, 2023, **856**, 159060.

185. E. Hermsen, S. M. Mintenig, E. Besseling and A. A. Koelmans, *Environ. Sci. Technol.*, 2018, **52**, 10230-10240.

186. J. C. Prata, V. Reis, J. P. da Costa, C. Mouneyrac, A. C. Duarte and T. Rocha-Santos, *J. Hazard. Mater.*, 2021, **403**, 123660.

187. B. K. Nfor, N. N. Hylkema, K. R. Wiedhaup, P. D. E. M. Verhaert, L. A. M. van der Wielen and M. Ottens, *J. Chromatogr. A*, 2011, **1218**, 8958-8973.

188. N. A. Moringo, L. D. C. Bishop, H. Shen, A. Misiura, N. C. Carrejo, R. Baiyasi, W. Wang, F. Ye, J. T. Robinson and C. F. Landes, *P. Natl. Acad. Sci. USA*, 2019, **116**, 22938-22945.

189. Y. Wu, S. Chen, J. Wu, F. Liu, C. Chen, B. Ding, X. Zhou and H. Deng, *Sci. Adv.*, 2024, **10**, eadn8662.

190. V. Mazzini and V. S. J. Craig, *Curr. Opin. Colloid Interface Sci.*, 2016, **23**, 82-93.

191. X. Xi, D. Ding, H. Zhou, B. Baihetiyaer, H. Sun, Y. Cai, N. Wang and X. Yin, *J. Hazard. Mater.*, 2022, **437**, 129311.

192. D. Li, Y. Ouyang, H. Lu, Y. Xie, S. Guo, Q. Zeng, Y. Xiao, Q. Zhang and S. Huang, *Mater. Today Chem.*, 2023, **32**, 101629.

193. E. J. Dziwiński, J. Iłowska and J. Gniady, *Polym. Test.*, 2018, **65**, 111-115.

194. S. Tsuge, H. Ohtani and C. Watanabe, *Pyrolysis-GC/MS data book of synthetic polymers: pyrograms, thermograms and MS of pyrolyzates*, Elsevier, 2011.

195. M. Fischer and B. M. Scholz-Böttcher, *Environ. Sci. Technol.*, 2017, **51**, 5052-5060.

196. G. Dierkes, T. Lauschke, S. Becher, H. Schumacher, C. Földi and T. Ternes, *Anal. Bioanal. Chem.*, 2019, **411**, 6959-6968.

197. E. D. Okoffo, F. Ribeiro, J. W. O'Brien, S. O'Brien, B. J. Tscharke, M. Gallen, S. Samanipour, J. F. Mueller and K. V. Thomas, *Sci. Total Environ.*, 2020, **715**, 136924.

198. C. Rauert, Y. Pan, E. D. Okoffo, J. W. O'Brien and K. V. Thomas, *J. Environ. Expo. Assess.*, 2022, **1**, 13.

199. C. S. Witzig, C. Földi, K. Wörle, P. Habermehl, M. Pittroff, Y. K. Müller, T. Lauschke, P. Fiener, G. Dierkes, K. P. Freier and N. Zumbülte, *Environ. Sci. Technol.*, 2020, **54**, 12164-12172.

200. Q.-c. Li, Y.-j. Lai, S.-j. Yu, P. Li, X.-x. Zhou, L.-j. Dong, X. Liu, Z.-w. Yao and J.-f. Liu, *Anal. Chem.*, 2021, **93**, 4559-4566.

201. A. Ter Halle, L. Jeanneau, M. Martignac, E. Jardé, B. Pedrono, L. Brach and J. Gigault, *Environ. Sci. Technol.*, 2017, **51**, 13689-13697.

202. T. Toapanta, E. D. Okoffo, S. Ede, S. O'Brien, S. D. Burrows, F. Ribeiro, M. Gallen, J. Colwell, A. K. Whittaker, S. Kaserzon and K. V. Thomas, *Sci. Total Environ.*, 2021, **796**, 148835.

203. N. M. Ainali, D. N. Bikiaris and D. A. Lambropoulou, *J. Anal. Appl. Pyrolysis*, 2021, **158**, 105207.

204. S. M. Mintenig, P. S. Bäuerlein, A. A. Koelmans, S. C. Dekker and A. P. van Wezel, *Environ. Sci. Nano*, 2018, **5**, 1640-1649.

205. Y. Zhu, R. Che, X. Zong, J. Wang, J. Li, C. Zhang and F. Wang, *J. Environ. Manage.*, 2024, **352**, 120039.

206. Y. Kida, T. Sawada, T. Iwasaki, T. Kadonosono and T. Serizawa, *Polym. J.*, 2023, **55**, 289-294.

207. S. Wang, E. S. Humphreys, S.-Y. Chung, D. F. Delduco, S. R. Lustig, H. Wang, K. N. Parker, N. W. Rizzo, S. Subramoney, Y.-M. Chiang and A. Jagota, *Nat. Mater.*, 2003, **2**, 196-200.

208. V. Puddu and C. C. Perry, *ACS Nano*, 2012, **6**, 6356-6363.

209. J. D. Sachs, G. Schmidt-Traub, M. Mazzucato, D. Messner, N. Nakicenovic and J. Rockström, *Nat. Sustain.*, 2019, **2**, 805-814.

210. B. Belete, B. Desye, A. Ambelu and C. Yenew, *Environ. Health Insights*, 2023, **17**, 11786302231195158.

211. J. Ianes, S. Piraldi, B. Cantoni and M. Antonelli, *Water Res. X*, 2025, **29**, 100334.

212. S.-W. Nam, Y. Yoon, S. Chae, J.-H. Kang and K.-D. Zoh, *Environ. Eng. Sci.*, 2017, **34**, 752-761.

213. S. Ghatge, Y. Yang, J.-H. Ahn and H.-G. Hur, *Appl. Biol. Chem.*, 2020, **63**, 27.

214. B. T. Ho, R. T. K. and S. and Lucas, *Crit. Rev. Biotechnol.*, 2018, **38**, 308-320.

215. M. Yikmis and A. Steinbüchel, *Appl. Environ. Microbiol.*, 2012, **78**, 4543-4551.

216. D. Wang, A. A. Ingram, A. Okumura, T. P. Spaniol, U. Schwaneberg and J. Okuda, *Chem. Eur. J.*, 2023, e202303066.

217. T. Mirzaei Garakani, D. F. Sauer, M. A. S. Mertens, J. Lazar, J. Gehrmann, M. Arlt, J. Schiffels, U. Schnakenberg, J. Okuda and U. Schwaneberg, *ACS Catal.*, 2020, **10**, 10946-10953.

218. A. Gallo-Cordova, B. Corrales-Pérez, P. Cabrero, C. Force, S. Veintemillas-Verdaguer, J. G. Ovejero and M. d. P. Morales, *Chem. Eng. J.*, 2024, **490**, 151725.

219. A. C. Morales, J. M. Tomlin, C. P. West, F. A. Rivera-Adorno, B. N. Peterson, S. A. L. Sharpe, Y. Noh, S. M. T. Sendesi, B. E. Boor, J. A. Howarter, R. C. Moffet, S. China,

B. T. O'Callahan, P. Z. El-Khoury, A. J. Whelton and A. Laskin, *Nat. Nanotechnol.*, 2022, **17**, 1171-1177.

220. M. Giustra, G. Sinesi, F. Spena, B. De Santes, L. Morelli, L. Barbieri, S. Garbujo, P. Galli, D. Prosperi and M. Colombo, *ChemSusChem*, 2024, **17**, e202401065.

221. A. D. Vethaak and J. Legler, *Science*, 2021, **371**, 672-674.

222. V. C. Shruti, F. Pérez-Guevara, P. D. Roy and G. Kutralam-Muniasamy, *J. Hazard. Mater.*, 2022, **423**, 127171.

223. M. Tashiro, R. Tejero, D. E. Zimmerman, B. Celda, B. Nilsson and G. T. Montelione, *J. Mol. Biol.*, 1997, **272**, 573-590.

224. J. Serrano-Plana, C. Rumo, J. G. Rebelein, R. L. Peterson, M. Barnet and T. R. Ward, *J. Am. Chem. Soc.*, 2020, **142**, 10617-10623.

225. I. Leppänen, T. Lappalainen, T. Lohtander, C. Jonkergouw, S. Arola and T. Tammelin, *Nat. Commun.*, 2022, **13**, 1814.

226. X. Fu, S. Zhang, X. Zhang, Y. Zhang, B. Li, K. Jin, X. Feng, J. Hong, X. Huang, H. Cao, Q. Yuan, P. Ai, H. Yu and Q. Li, *Adv. Funct. Mater.*, 2023, **33**, 2212570.

227. Y. Wang, M. Wang, Q. Wang, T. Wang, Z. Zhou, M. Mehling, T. Guo, H. Zou, X. Xiao, Y. He, X. Wang, O. J. Rojas and J. Guo, *Advanced Materials*, 2023, **35**, 2301531.

228. C. W. Sadoff, E. Borgomeo and S. Uhlenbrook, *Nat. Sustain.*, 2020, **3**, 346-347.

## Appendix

Amino acid sequence involved in this thesis:

LCI-strep-DZ

MAIKLVQSPNGNFAASFVLDGTKWIFKSKYYDSSKGYWVGIYEVWDRKSAWSHPQ
FEKADNKFNKEQQNAFYEILHLPNLNEEQRNGFIQSLKDDPSQSANLLAEAKKLNDA
QAPK

strep-DZ-MBP1

MSAWSHPQFEKADNKFNKEQQNAFYEILHLPNLNEEQRNGFIQSLKDDPSQSANLLA
EAKKLNDAQAPKRSGRGECRRQCLRRHEGQPWETQECMRRCRRRG

LCI-strep-DZ-MBP1

MAIKLVQSPNGNFAASFVLDGTKWIFKSKYYDSSKGYWVGIYEVWDRKSAWSHPQ
FEKADNKFNKEQQNAFYEILHLPNLNEEQRNGFIQSLKDDPSQSANLLAEAKKLNDA
QAPKRSGRGECRRQCLRRHEGQPWETQECMRRCRRRG

LCI_F16C

MGLGKKLSVAVAASFMSLSISLPGVQAAEFSAWSHPQFEKAEAAAKEAAAKEAAA
KAENLYFQGAIKLVQSPNGNFAASCVLDGTKWIFKSKYYDSSKGYWVGIYEVWDR
K (signal peptide was marked in red)

## Acknowledgment

I would like to express my sincere gratitude to Prof. Dr. Schwaneberg for offering me the opportunity to conduct my doctoral research at the Institute of Biotechnology, RWTH Aachen University. His guidance and continuous support throughout my Ph.D. were instrumental in shaping both my scientific and personal development. I also wish to thank Prof. Dr. Maria Fyta for serving as the second referee and for her role on my evaluation committee.

Special thanks go to Dr. Francisca Contreras Leiva and Dr. Marian Bienstein, coordinators of the PlastiQuant project, whose support, encouragement, and belief in my potential greatly motivated me throughout this journey. I am equally grateful to Dr. Lilin Feng, Dr. Dong Wang, Ling Zhang, Dr. Konrad Hoeft, Leon Ahrens, and Julian Luka for their cooperation, scientific input, and valuable assistance during the course of the project.

I gratefully acknowledge the German Federal Ministry of Education and Research (BMBF) for funding this work within the framework of BioRevierPLUS: Bioökonomie-REVIER Innovationscluster Biotechnologie & Kunststofftechnik (PlastiQuant and ProtLab, FKZ 031B1134C). My heartfelt thanks extend to our external collaborators: Dr. Tetiana Kurkina, Dr. Marisa Sárria Pereira de Passos, Dr. Gabriella Schirinzi, Dr. Dora Mehn, Dr. Andrea Valsesia, Dr. Cloé Desmet, Dr. Miguel-Ángel Serra, Dr. Douglas Gilliland, Maximilian Lorberg, and Prof. Jun Okuda, for their insightful discussions and productive collaborations.

I am also thankful to all members of the Schwaneberg group, especially the colleagues involved in the Plastic Detection and Management Competence Cluster, for their constructive feedback and camaraderie. I would like to acknowledge the dedicated technical staff, Jens Bührmann, Ursula Holter, Wolfgang Gloy, Sarah Zeschnigk, and Jens Gruber, for their invaluable help in laboratory operations and organization.

To my friends from China, both near and far, thank you for your emotional support, friendship, and for standing by me throughout this journey. Lastly, I am deeply thankful to my family, especially my parents, for their unwavering support, encouragement, and for providing me with the foundation that made this achievement possible.

## Author contribution

**Mao, M.**,[+] Ahrens, L.,[+] Luka, J.,[+] Contreras, F., Kurkina, T., Bienstein, M., de Passos, M., Schirinzi, G., Mehn, D., Valsesia, A., Desmet, C., Serra, M., Gilliland, D., & Schwaneberg, U. (2024). Material-specific Binding Peptides Empower Sustainable Innovations in Plant Health, Biocatalysis, Medicine and Microplastic Quantification. *Chem. Soc. Rev.*, 53(12), 6445-6510. [+]Shared first authorship

The manuscript has been published in cooperation with the Joint Research Center (Italy). The first authorship was shared with Leon Ahrens and Julian Luka. M., de Passos, M., Schirinzi, G., Mehn, D., Valsesia, A., Desmet, C., Serra, and M., Gilliland, D. did the original writing for the microplastic analysis part. Mao, M., Ahrens, L., Luka, J., Contreras, F., Kurkina, T., Bienstein, M., and Schwaneberg, U. did the original writing for the rest. Mao, M. focused on the binding peptides for natural carbohydrates, Ahrens, L. focused on the binding peptides for minerals, and Luka, J. focused on the computational part. All authors helped revise the paper. Prof. Ulrich Schwaneberg supervised the project, advised on the literature study, manuscript structure design, and reviewed the manuscript.

**Mao, M.**, Bienstein, M., Contreras, F., Wang, D., Feng, L., & Schwaneberg, U. (2025). MagNanoTrap Enrichment Empowers Ultra-sensitive Quantification of Mixed Nanoplastic Particles from Environmental Water Samples. *Angew. Chem. Int. Ed.* 2026, e22823.

M, M. designed and performed most of the experiments and wrote the original manuscript. M.B. participated in the experiment design and result discussion. F.C. participated in the experiment design, result discussion, and manuscript revision. D.W. participated in the result discussion. L.F. participated in the materials characterization. U.S. conceived the idea, directed the project, and wrote and revised the original manuscript.

Wang, D.,[+] **Mao, M.**,[+] Lorberg, M., Luka, J., Bienstein, M., Okuda, J., & Schwaneberg, U. (2025). Hooked for Decay with Hydrophobic-coated Magnetic Beads to Grapple and Disintegrate Nanoplastics. *Angew. Chem. Int. Ed.* 2025, 64, e202510356. [+]Shared first authorship

The manuscript has been published by Dong Wang and Maochao Mao with shared first authorship. Dong and Maochao designed the whole experiment. Dong did all the chemical synthesis, biohybrid catalyst design and characterization, and SBR degradation. Maochao did the materials characterization and nanoplastics enrichment experiments. Lorberg, M. helped

SBR ethenolysis set-up establishment. Bienstein, M. participated in the experiment discussion. Prof. Okuda helped with the experiment design. Prof. Schwaneberg revised the manuscript.

## Declaration of authorship

I hereby declare that all information in this document has been obtained and presented in accordance with academic rules and ethical conduct. I also declare that, as required by these rules and conduct, I have fully cited and referenced all material and results that are not original to this work.

Maochao Mao Aachen, 27.10.2025

## Curriculum vitae

### Personal Information

| | |
|---|---|
| Name | Maochao Mao |
| Date of birth | 6th March 1996 |
| Place of birth | Sichuan, China |
| Nationality | Chinese |

### Education

**2022-2025** Dr. rer. nat. (Ph.D.) Fellow, Institute of Biotechnology (Bio VI), Faculty of Mathematics, Computer science, and Natural sciences, RWTH Aachen University, Aachen, Germany

**2019-2021** Master of Biotechnology. Division of Biotechnology and Applied Microbiology, Lund University, Sweden.

**2014-2018** Bachelor of Biological Engineering. Faculty of Chemical Engineering, Tianjin University, China.